University of Washington
Department of Civil and Environmental Engineering

USE OF A ONE-DIMENSIONAL SNOW COVER MODEL TO ANALYZE MEASURED SNOW DEPTH AND SNOW TEMPERATURE DATA FROM SOUTHERN FINLAND

Harri J. Koivusalo
Stephen J. Burges

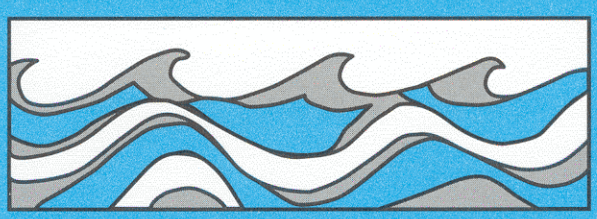

Water Resources Series
Technical Report No.150
March 1996

Seattle, Washington
98195

Department of Civil Engineering
University of Washington
Seattle, Washington 98195

USE OF A ONE-DIMENSIONAL SNOW COVER MODEL TO ANALYZE MEASURED SNOW DEPTH AND SNOW TEMPERATURE DATA FROM SOUTHERN FINLAND

Harri J. Koivusalo
Stephen J. Burges

Water Resources Series
Technical Report No. 150

March 1996

ABSTRACT

Snow properties vary vertically in a seasonal snowpack due to periodical accumulation of new snow and continuous metamorphism as a result of temperature changes, snowpack weight, and liquid water percolation. If the soil underneath the snow cover is frozen and impermeable, alternating freezing and thawing temperatures in early winter may result in formation of a distinct ice layer on the soil surface. A multilayered one-dimensional snow model (SNTHERM, Jordan 1991), which accounted for the relevant mass and energy transfer processes, was used to model the properties of a winter snowpack. Measurements of snow cover mass, vertical temperature, and meteorological variables were available at an experimental site in Southern Finland for the 1993-94 winter season. The quality of data was checked by comparing the measured meteorological variables with those at the nearest weather stations. The experimental site measurements were used to determine the relevant soil and snow initial conditions for the model. The model results indicated that the calculated snow mass and temperature were in good agreement with the measurements and the model was able to simulate the formation of an ice layer immediately above the soil surface. The sensitivity of the model to prescribed systematic and random perturbations in the input data series was examined. The calculated snow depth was most sensitive to systematic errors in the air temperature measurements and the estimated long-wave radiation. Systematic errors in the other meteorological variables, which include short-wave radiation, were of minor importance to the snowmelt, which was influenced principally by sensible heat fluxes. Random errors in the meteorological variables had practically no influence on the modeled snow mass.

ACKNOWLEDGMENTS

This report was prepared initially as the Master of Science in Civil Engineering Thesis of the first author. We thank our colleagues, Professors Susan Bolton and Dennis Lettenmaier, for their valuable and fruitful comments on the original thesis. This study was made possible by support provided to the first author by the Valle Scholarship for Scandinavian Exchange Students, and the Finnish Foundations: Suomen Kulttuurirahasto, Sven Hallinin Tutkimussäätiö, and Vilho, Yrjö ja Kalle Väisälän Rahasto. We appreciate the support and continuing interest in this work by Professor Dale Carlson, director of the Valle Program. Special thanks are due to Dr. Rachel Jordan for making her snow model available. The field investigations for this study were made in Finland with the help of Professor Tuomo Karvonen, Pertti Hyvönen, Noor Sepahi, and Maija Paasonen-Kivekäs.

The first author records his deepest gratitude to his wife Pirjo and daughter Anna for their support and patience throughout his studies at the University of Washington.

Table of Contents

List of Figures

List of Tables

Chapter 1 Introduction

Seasonal snowpack and spring melt comprise a significant portion of the annual runoff in a humid continental climate such as in Finland. Rapid melting of snow masses may contribute to extreme spring floods causing major threat to the inhabitants and the structures occupying the floodplain. Frozen soil lowers meltwater infiltration and leads to surface runoff and fast streamflow response to snowmelt. For that reason, the soil moisture content in the early winter has a significant affect on the subsequent snowmelt runoff characteristics. Frozen soil with low moisture content may remain permeable, whereas near saturated frozen soil becomes impermeable.

The main energy sources for melting snowpack are net radiation, sensible heat, and latent heat. The combined effects of these inputs are often represented by using air temperature as an index of snowmelt (U.S. Army Corps of Engineers 1956, Male and Gray 1981, Rango and Martinec 1995). Such an energy index approach can be used to estimate the average snow mass balance. The behavior and characteristics of a vertically heterogeneous snowpack requires use of a multilayered snow mass and energy balance model to describe the vertical distribution of snow mass and its thermal properties (Anderson 1976, Jordan 1991). This type of energy balance model is necessary to describe quantitatively the liquid water movement and snow metamorphism.

The objective of this study was to apply a one-dimensional energy balance snow model (SNTHERM, Jordan 1991) to simulate snow properties throughout a winter. The main purposes were to model the vertical distribution and temporal change in snow mass and its thermal properties, and to study the influence of meteorological fluxes on changes in snow cover. The model was applied to a data set collected at Sjökulla, Southern Finland, during the winter of 1994. An ice layer was observed troughout the winter at the measurement site immediately above the soil surface, which caused water to pond at the ice-snow boundary. This impermeable layer played a major importance in the

formation of surface runoff, and therefore, the simulation of the time history of the ice layer became a primary objective in the model application.

The data included meteorological variables (air temperature, solar radiation, precipitation, relative humidity, and wind speed), snow cover measurements (depth and density), and temperature profiles in the snow and soil. Extensive data quality checking was done to determine the suitability of meteorological time series for use with the model. The data were compared to the measurements from nearby stations operated by the Finnish Meteorological Institute. The data quality was further checked using the snow model to identify inconsistencies in the measured meteorological time series, snow mass, and snow temperature, and to check the estimated long-wave radiation. The model was then used to simulate the measured snow depth and thermal properties for the winter season. The relative influence of the meteorological variables on snow depth was analyzed by examining systematic and random errors, which were added to the input series.

A brief survey of the relevant literature discussing the energy balance approach to snow modeling is presented in Chapter 2. Chapter 3 presents the data and the quality assurance/control procedures used. Chapter 4 presents the model application and discusses the results. A general discussion, conclusions, and suggestions for future research completes this report. A summary of pertinent features of Jordan's (1991) model is presented in Appendix A.

Chapter 2 Modeling Snowpack and Snow Thermal State

2.1 Introduction

Operational snowmelt models are commonly based on an empirical temperature index approach, since air temperature is well related to the melting of snow especially in densely forested areas, and temperature data are more readily available than data needed for a complete energy balance (U.S. Army Corps of Engineers 1956, Male and Gray 1981, Rango and Martinec 1995). Zuzel and Cox (1975) concluded that air temperature was the best single predictor of snowmelt if only one meteorological variable was available; the best combination of meteorological variables was vapor pressure, net radiation, and wind speed. Kustas et al. (1994) compared two energy index based models and an energy balance model to predict lysimeter outflows from snowpacks in alpine catchments. The "restricted degree-day" model (Kustas et al. 1994), which included a radiation term and a degree-day factor, performed comparably to the energy balance model. The use of energy index models is appropriate for making operational snowmelt predictions in relatively homogeneous areas, where catchment outflow or average snow water equivalent is the main interest. Index models give best results if the melt factor relating to an energy component is not changing in space and time, or the change can be estimated effectively (Rango and Martinec 1995). Temperature index models become less satisfactory if energy components other than long-wave radiation dominate the melt process. For example, short-wave radiation, and sensible and latent heat become the dominant energy sources during clear skies in open areas (Male and Gray 1981, Vehviläinen 1986). Sensible and latent heat are often of opposite sign and can cancel each other in particular locations (e.g., Marks 1988).

Physically-based models require more complete meteorological data to effect the energy balance of snow. In addition to air temperature, measurements of net radiation, vapor pressure, wind speed, and initial and boundary conditions such as soil temperature are

needed. Energy balance models, which treat snowpack as a single layer, are not necessarily superior to empirical approaches in predicting average snow water equivalent or catchment outflow (e.g., WMO 1986). An energy balance approach is necessary when investigating sensitivity of snow accumulation and ablation to climate or land use changes, and in the context of coupled land-atmosphere models where surface energy fluxes become important. Energy balance models are also useful in simulating small-scale processes of snow metamorphosis, melt and thermal state, or for predicting spatially-distributed snow water equivalent or short-term extreme conditions (Blöschl et al. 1991, Gray and Prowse 1992). Snow settling and compaction are complicated processes which depend on the continuously changing structure of the snow. Therefore, bulk averaging of snow properties at some spatial scale is required for energy balance models to be effective (Anderson 1976, Jordan 1991). The small-scale spatial distribution of snow is highly variable due to changes in topography, vegetation, and snow drifting. Simplifications in the representation of snow physics are needed to enable computationally efficient solution to the set of mass and energy balance equations used in physically-based snow models.

The energy balance components of snow and the modeling approaches for describing the atmosphere-soil-snow energy exchange are discussed below. The structure of such models is investigated with emphasis on point energy balance approaches. Snow properties affecting metamorphism and energy exchange are also described.

2.2 Snow Energy Budget

The energy balance of a snow mass is defined by the internal energy, and the thermodynamic states, and the energy fluxes at the snowpack boundaries. The fluxes include net radiation, sensible and latent heat, ground heat, and advective heat. The energy exchange across the air-snow interface is in most cases more important than across the soil-snow interface (e.g., Price and Dunne 1976, Anderson 1976, Marks

1988). For a control volume enclosing the snow mass, the sum of the incoming and outgoing energy components equals the change in the internal energy, which is used to warm and melt the pack. The relative importance of the energy components may vary considerably in time and space depending on the site characteristics and diurnal and seasonal variation of the meteorological variables; none of the energy components dominates constantly (Gray and Prowse 1992).

2.2.1 Net Radiation

The radiant energy is considered separately as short (solar) and long (terrestrial) wavelengths, because the electromagnetic absorption (and reflection) properties of snow vary considerably with the wavelength of radiant energy. Furthermore, solar radiation may be subdivided into visible and near-infrared ranges (e.g., Marks 1988). The net short-wave radiation is the difference between the incoming and reflected global radiation, which combines direct and diffuse radiation. In the short-wave range (approximately 0.3-3 μm), snow is a relatively efficient reflector with high albedo. The snow surface albedo changes with time depending on snow age, density, liquid water content, and surface roughness, the solar angle, the spectral composition of radiation, and objects which fall onto the snow. Snow metamorphism changes the grain size of the snow crystals, and snow albedo decreases with increasing grain size (Male and Gray 1981). Liquid water present in snow decreases the albedo, because the albedo of water is considerably lower than that of snow. Snow albedo is higher at low solar zenith angles. For small snow depths, the low albedo of the underlying soil surface tends to decrease the areal average snow albedo. Deposition of new snow increases the snow albedo temporarily.

The part of the short-wave radiation that is not reflected, is absorbed and transmitted to the lower layers of the snowpack. The amount of absorbed short-wave radiation

decreases approximately exponentially with depth (e.g., Anderson 1976) and is represented using an empirical extinction coefficient. The value of the extinction coefficient depends on wavelength, grain size, and density. If soil under a shallow snow cover absorbs and emits the transmitted solar radiation (as long-wave radiation), snowmelt may be accelerated.

In the long-wave radiation range (3-100 μm), snow acts almost like a pure black body cavity radiator and absorbs nearly all incident long-wave radiation from clouds or vegetation canopy (U.S. Army Corps of Engineers 1956). The Stefan-Boltzmann law can be used to calculate long-wave radiation emitted to the atmosphere from the snow surface (e.g., Wallace and Hobbs 1977, p. 289). Long-wave radiation is an important energy input to snow in forests, where incident short-wave radiation is absorbed by the canopy, and during the presence of low clouds, which prevent the escape of the long-wave radiation emitted from snow to the atmosphere. The snowpack cools considerably during night time clear skies in open areas (Gray and Prowse 1992). Measurements of long-wave radiation are seldom available, and the Stefan-Boltzmann law is used to estimate downward long-wave radiation using air or cloud base temperature. The atmospheric emissivity is related to water vapor pressure, and the radiation is further corrected for cloud cover and site conditions (Bras 1990, Gray and Prowse 1992).

2.2.2 Sensible and Latent Heat Fluxes

The heat exchange at the snow surface occurs as sensible and latent heat. Sensible heat is due to convection of air to the snowpack, whereas latent heat is related to heat taken or released in evaporation from or condensation (of water vapor) onto the snow surface. Wind generated turbulence increases greatly the sensible and latent heat exchange: rough or uneven surfaces (high aerodynamic resistance) enhance turbulent eddies, whereas vegetation may reduce turbulent fluctuations near the snow surface. The magnitude of

the turbulent energy exchange is often relatively small during the cold winter, but may be significant during the melting period (U.S. Army Corps of Engineers 1956). Sensible heat is calculated using a (potential) temperature gradient between the snow surface and the overlying air. Latent heat is estimated using the vapor pressure gradient between the snow surface and the overlying air. The vapor pressure at the snow surface is commonly assumed to be that of saturated vapor over ice. The sensible and latent heat fluxes need to be corrected for atmospheric stability, which depends on the vertical temperature lapse rate relative to an adiabatic lapse rate (Wallace and Hobbs 1977, p. 81-86). During snowmelt, stable conditions with the actual lapse rate less than an adiabatic lapse rate commonly prevail over the surface (Male and Gray 1981). Under neutral stability, the vertical profile of the (horizontal) wind speed in the turbulent layer varies approximately logarithmically. Stability related functions are used to correct the wind profile under stable or unstable conditions. Correction functions using a Richardson number as a stability index are presented, for example, in Anderson (1976, p. 12-18).

2.2.3 Advective and Ground Heat Fluxes

Advective and ground heat fluxes are usually minor components in the snow energy balance. Advective heat flux is due to the heat content of rain, which cools to the snowpack temperature. If rain water freezes when it enters the snowpack, the release of the latent heat of fusion increases the snow temperature. The heat content of snowfall is usually ignored. Ground heat flux is conducted from the ground below, which may be the only energy flux in the bottom layers of a deep snowpack. Ground heat flux may cause melting immediately above the soil surface during winter when melting at the snow surface does not exist (U.S. Army Corps of Engineers 1956). The contribution of ground heat flux to the bottom layer energy balance depends on the thermal properties of soil and snow depth.

2.2.4 Thermal State of Snow

The amount of heat needed to raise the temperature of the snowpack to 0 °C is called the cold content of snow (U.S. Army Corps of Engineers 1956). Snowmelt occurs once the cold content is satisfied. The thermal quality of snow is defined as the ratio of the heat required to produce a given amount of melt water from snow to the heat required to yield the same amount of melt water from ice at 0 °C.

Anderson (1976) lists the major energy transfer mechanisms in a snow mass. These include heat conduction, penetration of solar radiation, and phase changes of water. A second order partial differential heat equation (Anderson 1976, Eq. 3.3) defines the temperature changes due to heat conduction. Water vapor sublimation, which is included in the equation, depends on water vapor concentration changes. The effective coefficients for thermal conductivity and vapor diffusivity are defined for the mixture of ice, air, and water, which comprise the snow mass. Dry snow has low effective thermal conductivity and is a good insulator, because the pores in snow are filled with air only.

2.3 Snow Mass Budget

Snow mass changes are due to snowfall and rain, movement of liquid water and water vapor, and densification of snow, which is caused by compaction and metamorphosis. Liquid water movement takes place in an isothermal snowpack at 0 °C and may be calculated empirically using a storage model, which attenuates water before draining it to the layers below or out of the snowpack (e.g., Anderson 1976, p. 61-63). One common approach is to simplify the equation for fluid momentum to Darcy's law, in which capillary forces are ignored (Colbeck 1972, Jordan 1991). Water flow in heterogeneous snow with irregular ice layers cannot be described using any of the previous approaches. Reasonable predictions of average melt water flow have been achieved using both empirical and physical approaches with effective parameters

(Anderson 1976, Jordan 1991). Mass transfer through snow surface (evaporation and condensation) is of minor importance compared to the mass changes during liquid water movement in melting snow. Dry, cold snow has a small amount of retained liquid water. However, except in the evaluation of snow porosity, the retained water in snow is usually ignored in the calculations of water movement. More complete details are given in Arons and Colbeck (1995) who reviewed the state-of-the-art of theories on small-scale snow texture and its relation to water and vapor transport through snow.

2.3.1 Snow Metamorphism

Temperature changes in snow lead to what is referred to as *temperature gradient metamorphism*, since the vapor pressure becomes lower in cold snow and vapor diffuses to the lower pressure. Therefore, colder snow crystals grow at the expense of warmer crystals by deposition of vapor. The growth of the colder crystals depends on the steepness of the temperature gradient. *Depth hoar* is caused by a steep temperature gradient at the bottom of the snowpack, where the vapor diffuses to overlying snow crystals from the warmer soil below. Similarly, *hoar frost* is developed on the snow surface due to radiative night time cooling (Langham 1981). In the absence of steep temperature gradients, vapor pressure differences due to changes in radii of grain surface curvature exist, but the speed of metamorphism lowers. Some temperature gradient and heat flow is required to metamorphose snow (Colbeck 1982).

New snow experiences *destructive metamorphism*, in which large snow grains grow at the expense of small grains. Local stresses such as weight of the overlying snow masses or shear stress on a steep hillslope increase vapor pressure differences and contribute to snow metamorphism. Increasing liquid water content enhances snow metamorphism by bonding the snow grains together and enhancing conductive heat transfer between the grains. Small grains tend to dissipate, while big grains grow. Refrozen wet snow

becomes hard since the individual grains become connected due to liquid water bonding. This is called *melt-freeze metamorphism* (Langham 1981).

Colbeck (1991) describe the layered nature of snow cover and the high variation of the layer properties in time and space. The layered structure of snow is a result of variable processes affecting snow surface and snowpack below. A hard layer on the snow surface such as *wind slab* or *wind crust* leaves a distinct layer when covered by new snow. On the other hand, spatially variable snow metamorphism or unevenly percolating and re-freezing liquid water result in layers with spatially variable physical properties at a given elevation inside the snowpack.

2.3.2 Hydraulic Properties of Snow

In mass balance calculations, the snowpack, or layers of snow are commonly assumed to be homogeneous with uniform hydraulic properties. The *liquid water holding capacity* or *irreducible water saturation* of snow is due to capillary retention of water. When the water content is less than the irreducible water saturation, the water film is discontinuous. Water can flow only in snow when the saturation is higher than the irreducible saturation (Colbeck 1972). Both water and air are present in snow and the permeability of water or air depends on the snow pore geometry and the volume of water relative to volume of air. Capillary pressure is defined as the difference between pressures in the air and water phases, which is always positive in snow because snow is hygroscopic. Capillary forces, which are usually ignored, become important at the front of an advancing meltwater pulse, where the water content changes rapidly from the irreducible saturation level to saturated (Colbeck 1972). The variable properties of snow in time and space makes the evaluation of the hydraulic properties in snow difficult: properties typically are averaged over assumed homogeneous snow layers (Anderson 1976, Morris 1983, Jordan 1991).

2.3.3 Water Percolation in Snow

In empirical models of water movement through snow, the liquid water in excess of the water holding capacity of the snow determines the amount of water that can percolate (U.S. Army Corps of Engineers 1956, Anderson 1976). This quantity is further lagged and attenuated in water storages before draining out of the snowpack (e.g., Anderson 1976, p. 61-63). In models based on physical principles, the percolation of periodical inputs of water proceeds in unsaturated snow as a shock wave front, whose gradient increases with depth in the upper layers of snow, and decreases and turns into approximately steady state flow at sufficient depth (Colbeck 1972). A numerical solution to the propagation of the infiltrating shock wave can be effected, for example, using the method of characteristics. Colbeck (1974) represented the vertical movement of water in unsaturated snow as a shock front, and the horizontal movement of water in bottom saturated layers as Darcian flow. The characteristics of vertical and horizontal water movement in snow were different, especially the water flux wave in saturated snow was considerably faster than in unsaturated snow.

The layered character of snow causes the hydraulic properties to be highly variable in time and space (Colbeck 1991). For example, an ice layer in snow restrains the downward percolation of water where it is diverted laterally or stays and accumulates on the ice layer. The ice layer experiences spatial variation in melting once melt water penetrates the layer at low or thin points. The resulting percolation through the ice layer is spatially highly irregular. Therefore, the use of physical methods assuming apparently homogeneous snow and ice layer properties is not necessarily superior to empirical methods.

2.4 Energy Balance Approach in Snow Modeling

2.4.1 Model Components and Data Requirements

The energy balance approach permits calculating the heat available to change snow temperature or to melt snow. Mass balance calculations track the movement of liquid water in snow, the addition of (precipitated) mass, and the phase changes of water. Changes in snow structure also need to be considered. Using mixture theory, the mass balance is calculated separately for the solid, liquid and vapor phases of water (e.g., Kelly et al. 1986). At the snow surface, the incoming fluxes of radiation need to be measured (or estimated using an index of sunshine hours or cloudiness, air humidity, and temperature). Sensible and latent heat are estimated using the measured air temperature, vapor pressure, and wind speed. The vapor pressure of the overlying air is estimated using the measured dew point temperature or air temperature and relative humidity. Inside the snowpack, a heat flow equation determines the temperature profile based on the thermal properties of the snow. At the soil-snow boundary, the ground heat flux is estimated using the measured soil temperature.

In most energy balance models, the properties of water at 0 °C are utilized (e.g., Anderson 1976, Marks 1988). Below 0 °C no liquid water is assumed present and the snow temperature is the only unknown. At 0 °C snow is isothermal, the temperature is known and only liquid water contend needs to be estimated. However, some water can persist in the liquid phase at temperatures below 0 °C, in which case a freezing curve determines the relation between liquid water content and snow temperature (e.g., Jordan 1991, p. 19-21).

In addition to energy balance equations, some approximations to snow physics and fluxes have to be introduced. Snow density changes are caused by the weight of snow and temperature gradients in the snow. A wind function, which depends on the stability

of the air column, is used to estimate the rate of turbulent heat exchange at the snow surface. The effective thermal conductivity, effective diffusivity of water vapor, extinction coefficient of snow, and snow albedo are calculated using relevant snow properties. Such models require initial conditions for each snow layer. Representative energy balance models and some of their features are reviewed below.

2.4.2 Examples of Energy Balance Models

Price and Dunne (1976) used an energy balance model to calculate daily snowmelt in subarctic plots in Quebec, Canada. The snowpack was considered as one homogeneous layer and the energy fluxes across the snow surface were calculated. Advective heat was ignored since no precipitation occurred during the measurement period. Ground heat flux was assumed negligible because the ground remained frozen throughout the melting period. The net radiation in open or forested areas was calculated as a function of measured global radiation in an open area. The turbulent exchange coefficients for sensible and latent heat were corrected for atmospheric stability conditions. The results of modeled daily snowmelt were in reasonable agreement with measurements. The energy balance was particularly sensitive to the assumed surface roughness length.

The energy balance model and the data were further used to calculate the daily melt input to the snowpack (Dunne et al. 1976). The water percolated through unsaturated snow as a shock front, and the vertical movement of water in the bottom saturated zone was estimated using Darcian flow theory (Colbeck 1974). The calculated daily hydrographs as well as the depth of the bottom saturated layer were in good agreement with the observations. The modeled meltwater outflow rate was most sensitive to the snowpack depth, the accuracy of melt input from the snow surface, and the (saturated and unsaturated) permeability of snow.

A rigorous approach for modeling energy and mass balance of snow was presented by Anderson (1976). A one-dimensional multilayered model was developed and tested using detailed meteorological and snow cover data measured in Vermont, USA. The model divided a snowpack into assumed homogeneous layers of variable thickness and the number of layers was allowed to change with time. The model was able to simulate continuously the seasonal formation, ablation, and melting of the snow pack. During one time step, the model solved the snow temperature profile and if the layer temperature was 0 °C, the energy balance was solved for the liquid water content. In addition, mass fluxes due to phase changes of water, liquid water transmission, and the density changes in each snow layer were calculated. The liquid water transfer was calculated using empirical equations, which lagged and attenuated excess water in conceptual storages. Empirical equations for a number of snow properties were developed. Snow density changes were divided into compaction, which was calculated based on the weigh of snow layers above, and settling, which was approximated using the temperature gradient in the snow. Density of precipitated snow was represented as a function of wet bulb temperature of the overlying air. Snow grain diameter and albedo depended on snow density. Effective thermal conductivity was related to the square of the snow density, and effective diffusivity of water vapor was represented as a function of temperature and air pressure. The extinction coefficient for solar radiation was related to snow grain diameter and density. Anderson (1976) compared empirical and physical wind functions and noticed that since unstable atmospheric conditions over melting snow were rare, the empirical wind functions performed justifiably well. The energy balance equation for each snow layer was written using an implicit finite difference scheme, and an iterative numerical solution for the profile of temperature/liquid water content for each time step was solved using the Newton-Rhapson method. Using the required input data, the model was able to simulate snow water equivalent, snow cover and surface densities, and snowpack temperature profile satisfactorily.

Marks (1988) tested a two-layer point energy balance model using measurements of meteorological and seasonal snow cover conditions in an alpine catchment in the Sierra Nevada Mountains in California, USA. The point model divided the snowpack into an upper active layer, in which the surface energy exchange occurred, and a lower layer, which interacted with ground and the layer above through conduction and diffusion. The layers were assumed homogeneous with uniform temperature, density and liquid water content. The thickness of the surface layer was taken constant and the layer was assumed to absorb most of the penetrating solar radiation. The energy budget determined the required change in layer temperature, cold content, and possible melt. Whenever the temperature of a layer was at 0 °C, the liquid water content was updated for melt, re-freezing, and evaporation or condensation, and the excess liquid water in the snowpack defined the meltwater runoff.

When calculating the net short-wave radiation, the albedo of the snow was parametrized separately in the visible and near infrared ranges as a function of grain size and solar zenith angle (Marks 1988, p. 53). The albedo of the near infrared radiation range is lower than that of the visible range. The results indicated that sensible and latent heat, and especially net radiation were critical during the melting period. Ground and advective heat fluxes were always negligible. The snowmelt model indicated satisfactory performance during cold weather in early spring when the snow liquid water content was low. However, the model was not tested against spring melt conditions.

A physically-based snowmelt algorithm was developed by Morris (1983) for the SHE model (Système Hydrologique Européen, Abbott et al. 1986). The SHE model incorporates physics-based equations of hydrological processes to distributed submodels, which describe snowmelt, canopy interception, evapotranspiration, overland and channel flow, and unsaturated and saturated subsurface flow. In the snow model, the flow of mass and energy in the snow was based on the conservation of mass, momentum, and energy, and the equations of state. Snow was considered a mixture of

three water phases and dry air; the ice matrix was assumed to be at rest (snow compaction was ignored) and mass changes due to vapor phase changes were ignored. Therefore, the mass and momentum equations were formulated considering the water phase only. The momentum equation was replaced with the Darcy's empirical law, and the energy equation was based on the first law of thermodynamics with the change in enthalpy set equal to changes in internal energy (heat flow) and work (pressure change under constant volume).

The thermal effects of vapor transfer in the energy equation were taken into account using an effective thermal conductivity, which was related empirically to snow density. A characteristic equation for snow (Morris 1983, Eq. 15) defined the variation of water content with capillary tension, which was further related to snow temperature with a low water content (pendular regime) or in near saturated snow (funicular regime). This determined the relation between snow water saturation and temperature (freezing curve). Hydraulic conductivity of snow was related to snow density, grain diameter, and capillary tension. The extinction of radiation was treated separately for short- and long-wave ranges, and the turbulent exchange coefficients were corrected for atmospheric stability at the surface boundary condition. The changes in phase were related to the distribution of ice-water-vapor assuming that the phase changes have an equal effect on all grains.

Morris (1983) tested the energy balance model against snow melting and re-freezing data, which were measured in Scotland, U.K. The results using a fixed (Eulerian) one-dimensional finite difference grid indicated good performance compared to temperature index models. The model performed especially well using *a priori* selected model parameters, which indicated that the physical model did not require extensive parameter optimization.

Kelly et al. (1986) presented a theory for a three phase mixture model of snow cover, in which dry air and water vapor were combined to form a moist air constituent. The mass and energy equations for the three constituents were modified slightly from those used by Morris (1983). In the case of snow saturated with water, the model was reduced to representing the thermodynamics of a mixture of water and ice. Morland et al. (1990) further gave a detailed theoretical framework for a four-constituent model of snowpack.

Mixture theory (e.g., Morris 1983) and the point model of Anderson (1976) were combined into a snow temperature model by Jordan (1991) which she called SNTHERM. The model has since been continuously refined and modified to take into account detailed processes affecting snowpack energy and mass balance. The model partitions a snowpack into horizontal layers in similar fashion to the approach used by Anderson (1976), and simulates snow temperature, density, effective thermal conductivity and specific heat profiles under a variety of winter conditions. In addition to snow properties, the model simulates soil temperatures. The mass balance equations are formulated for the three water phases and their mixture in snow. Snow metamorphism is based on snow mass overburden and destructive metamorphism following Anderson (1976).

The fluid flow equation describes water movement due to gravitational flux (Darcian flow) and phase change fluxes. Water movement in soil is disregarded, and snowmelt outflow is drained artificially at the snow-soil interface. The fluid flow and heat flux equations are coupled to determine the temperature and liquid water content of the snow layers. The freezing curve determines the relation between the depression temperature below 0 °C and the liquid water content in snow.

Jordan's (1991) model does not account for the effects of capillary pressure, fingering of flow, water ponding above ice lenses, and evaporation mass changes in the fluid flow equation. Mass changes due to vapor diffusion in soil are ignored except for the top soil

layer when it is exposed to the air. The extinction of the near infrared radiation is restricted to the top node, below which only the short-wave radiation penetrates. Heat transport due to conduction and vapor diffusion are combined using an effective thermal conductivity. A stability correction was used to calculate the wind function, except under stable atmospheric conditions where the correction was found to yield poor model results.

The model is solved using an implicit finite difference approximation to the governing equations, and the temperature profiles are calculated each time step using a tridiagonal-matrix equation solution algorithm. In the original version of the model (SNTHERM.89), the albedo of snow was taken to be constant. A revision was introduced late in 1995, when the variable snow albedo scheme presented by Marks (1988) was adopted.

A summary of SNTHERM and the governing equations is presented in Appendix A. As part of the research reported herein, SNTHERM is used to simulate snow and soil temperatures and snow structure using data measured in Finland during the winter of 1994.

Chapter 3 Site Description and Data

3.1 Sjökulla Experimental Field, Finland

Southern Finland has a temperate climate with four distinct seasons. The climate is affected by the Baltic Sea and the Atlantic Gulf Stream. The mean annual temperature in Helsinki is 5.3 °C. On the coastal side of the Gulf of Finland, winters are moderately warm with shallow snow cover depths and temperatures occasionally rising above 0 °C. Further north, the climate becomes continental with more established snow cover throughout the winter. At the experimental field site of the Laboratory of Water Resources Engineering, Helsinki University of Technology (Figure 3.1), snow cover mass and temperature measurements were made during the winter of 1993-1994. The studies were related to a research project on agricultural non-point source pollution, whose objective was to study the amounts of non-point loadings, and the influence of farming practices and nutrient recycling on those loads (Paasonen-Kivekäs 1994). Basic hydrological processes including surface and subsurface runoff and snowmelt dynamics were measured to provide sufficient quantitative data to assess the non-point source pollution.

3.1.1 Experimental Field Location and Measurement System

The agricultural experimental field is located in Sjökulla, Kirkkonummi, 32 km west of Helsinki (Figure 3.1). Temperature profile measurements in the snow (or air) and the soil were made at a downslope point of a fallow field (point A in Figure 3.1), which had relatively steep slope (10-15 %) and was partly shaded by trees located south of the field. The soil in the field area was silt and clay. The (snow or air) temperature profile was measured from 0.05 to 1.0 m above the soil surface. Soil temperatures were measured from -0.05 to -1.0 m below the surface. The specific vertical locations of

temperature sensors are shown in Figure 3.2. The measurement system was connected to a programmable data logger installed at the site. Radio modems were used to transmit the measurements from data logger to a computer located inside a building near the field. The individual temperature measurements were recorded using thermoelements (enclosed electrical resistance temperature sensors), the accuracy of which was not given by the manufacturer. The measurement frequency was 15 minutes.

Meteorological variables were recorded in the middle of a cultivated field section at location B (Figure 3.1) 220 m from the temperature profile site located at A. Solar radiation was measured using a pyranometer sensor sensitive to wavelengths in the range 400-1100 nm. The absolute accuracy of the sensor was given as ± 5 %. Relative humidity and air temperature were measured using sensors with ± 2-3 % accuracy for relative humidity and ± 0.2 °C for temperature. Wind speed at 1.8 m above the ground was recorded using an instantaneous anemometer reading with ± 1-2 % accuracy depending on the wind speed. Precipitation in the form of rain or snowfall was measured at the temperature profile site in the fallow field. The weight of an unshielded container (diameter 0.46 m) gave the accumulated precipitation. The container was supported at the end of a cantilever beam. The beam deflection had a one to one correspondence with the accumulated weight of the gauge plus precipitation. Electrical resistance strain gauges were used to measure the deflection. The accuracy of the weight was given as 0.03 % of the measured value. Meteorological variables were recorded as 15-minute instantaneous quantities.

Snow mass was sampled manually once a week during winter, and 3 to 4 times per week during periods when snow was melting. The measurements were taken at 6 points near the meteorological station labeled S1-S6 in Figure 3.1, and at one point within 10 m of the snow temperature profile site (S7). The snow density was based on the weight of the snow sampled using a 0.1 m diameter snow core cylinder. Before the onset of freezing, the soil appeared to be close to saturation (wet clay adhered to field workers'

boots). An ice or crust layer formed on the apparently impermeable (frozen) soil surface during the winter. This layer was too hard to be penetrated using the snow core cylinder. The depth of the ice layer was measured by cracking, breaking, and removing approximately 20 cm^2 of ice and measuring the distance from the top of the layer to the soil surface.

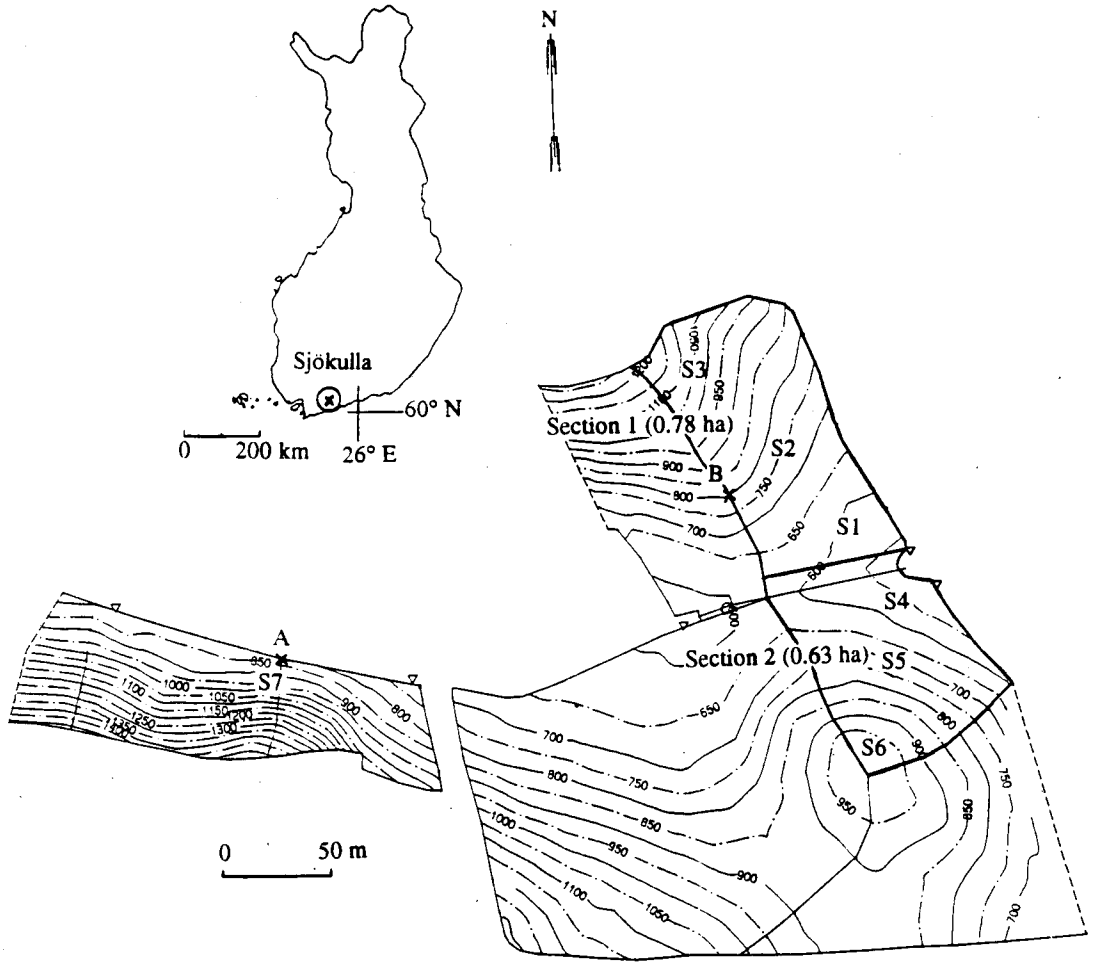

Figure 3.1. Location of experimental field, measurement stations, and snow cover measurement points in Sjökulla, Kirkkonummi. Point A refers to the temperature profile and precipitation gauge site, and B to the meteorological station. S1-S7 refer to the snow cover measurement locations.

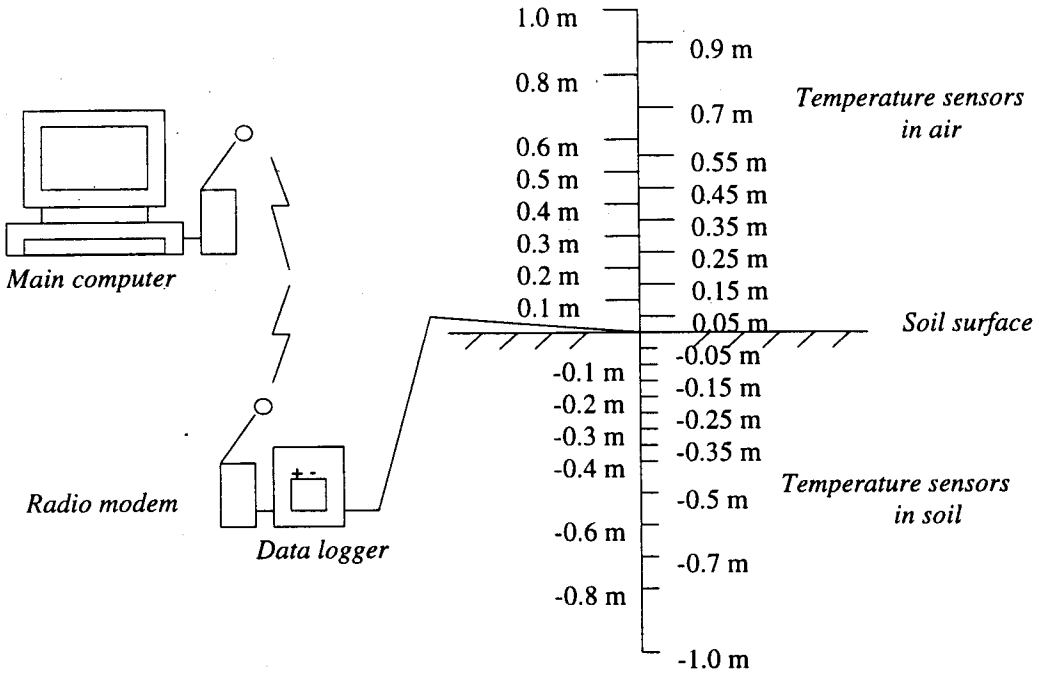

Figure 3.2. Vertical location of temperature sensors and schematic chart of data transfer system.

3.2 Data

The quality of the raw data was uncertain and a major activity was to determine the reliability of the various measurements. The time series were not continuous, some measured temperatures were unrealistic signaling occasional measurement system breakdowns. The solar radiation and relative humidity sensors gave values that were consistently too high indicating calibration errors. Measurement breaks were caused by problems in the (radio) data transfer between the field data loggers and the main recording computer. The small hill located between the temperature profile site and the main computer lowered the data transfer reliability between the radio modems. The main computer had a modem connection to the telephone network enabling remote data query. Unfortunately, the data gathering program ceased to collect data from the loggers whenever the telephone modem connection was used.

3.2.1 Temperature Profiles

The daily average temperatures were calculated using the original 15-minute measurements without editing any seemingly unrealistic values. Figure 3.3 shows the daily temperatures from October 1 1993 to April 30 1994 measured from the soil surface up to 1.00 m. The number of measurements recorded per day is shown together with the temperature graphs. On days when there were 96 15-minute measurements recorded, no data transmission failures or other measurement breaks occurred. The gradients in temperature starting in middle to late January correspond to snow accumulation. The melt period started in early April, 1994. The steepest temperature gradients were measured during a cold period in February. The distinct temperature gradient up to the sensor located 0.35 m above the soil surface corresponded to the highest snow depths in late February. Above the snow surface, the air temperatures remained nearly uniform. A high peak in the temperature profile which occurred in early March indicates that the measurement system was malfunctioning. Closer inspection of the entire record shows that the measurement system had operational difficulties every time after a period of freezing temperatures. The longer and the lower the temperatures remained during a cold period, the higher the peak that followed. Figure 3.3 shows that the system had the most frequent measurement breaks during the coldest part of the winter. Consequently, the daily average values during February were biased because of long periods of missing data.

Figure 3.4 shows the daily average soil temperature profile. The sensor located 1.00 m below the soil surface recorded the highest temperature during most the winter, and the sensors closer to soil surface followed fluctuations in the air temperature. Soil temperatures tended to change smoothly and any erroneous records were more distinctive than in the air temperature profile. The high peaks corresponded to time instants after individual periods of freezing air temperatures. After snow had melted and the air became warmer, the temperature gradient in the soil reversed.

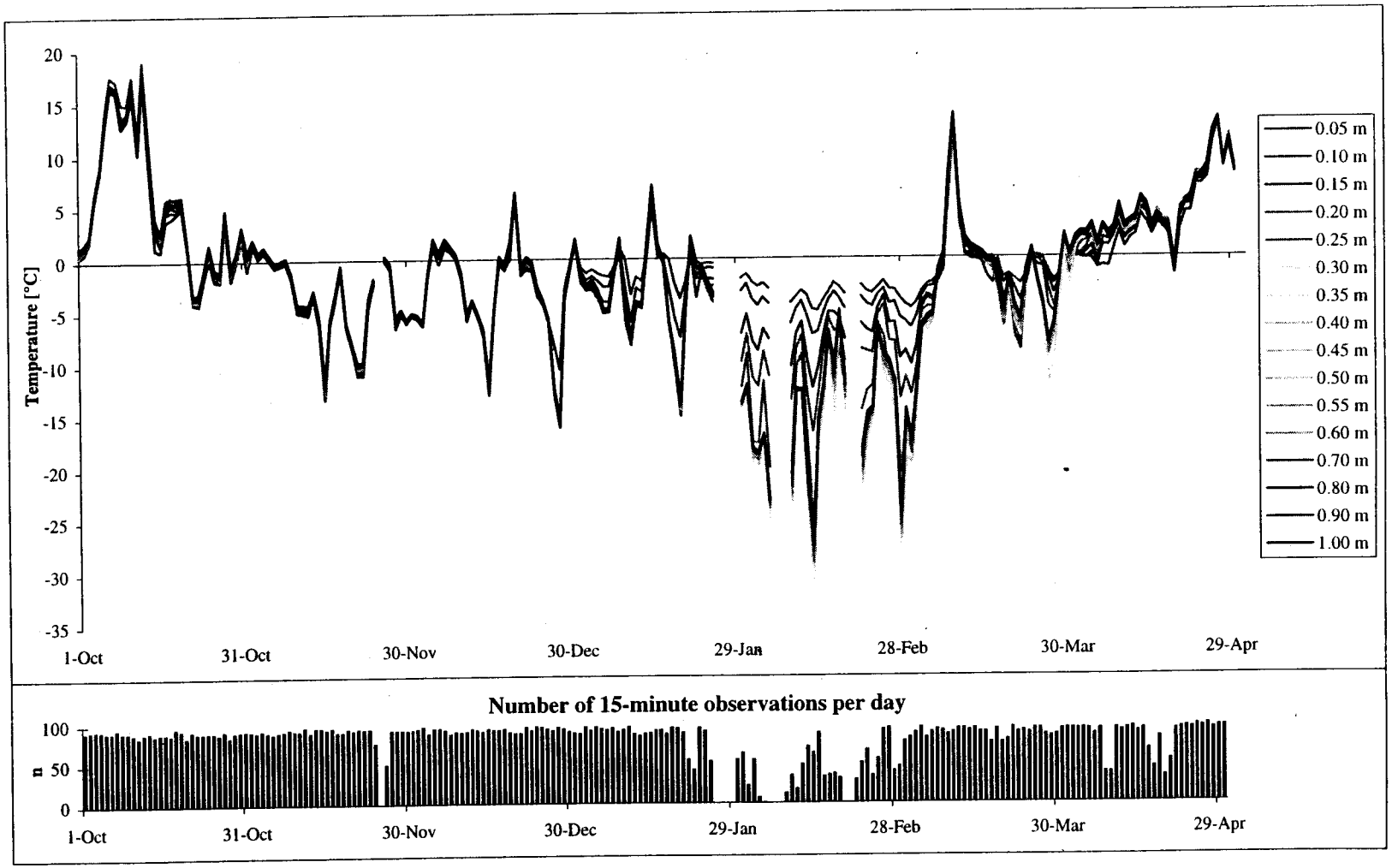

Figure 3.3. Daily average air/snow temperature profile from October 1 1993 to April 30 1994. Legend indicates height of sensor location above soil surface.

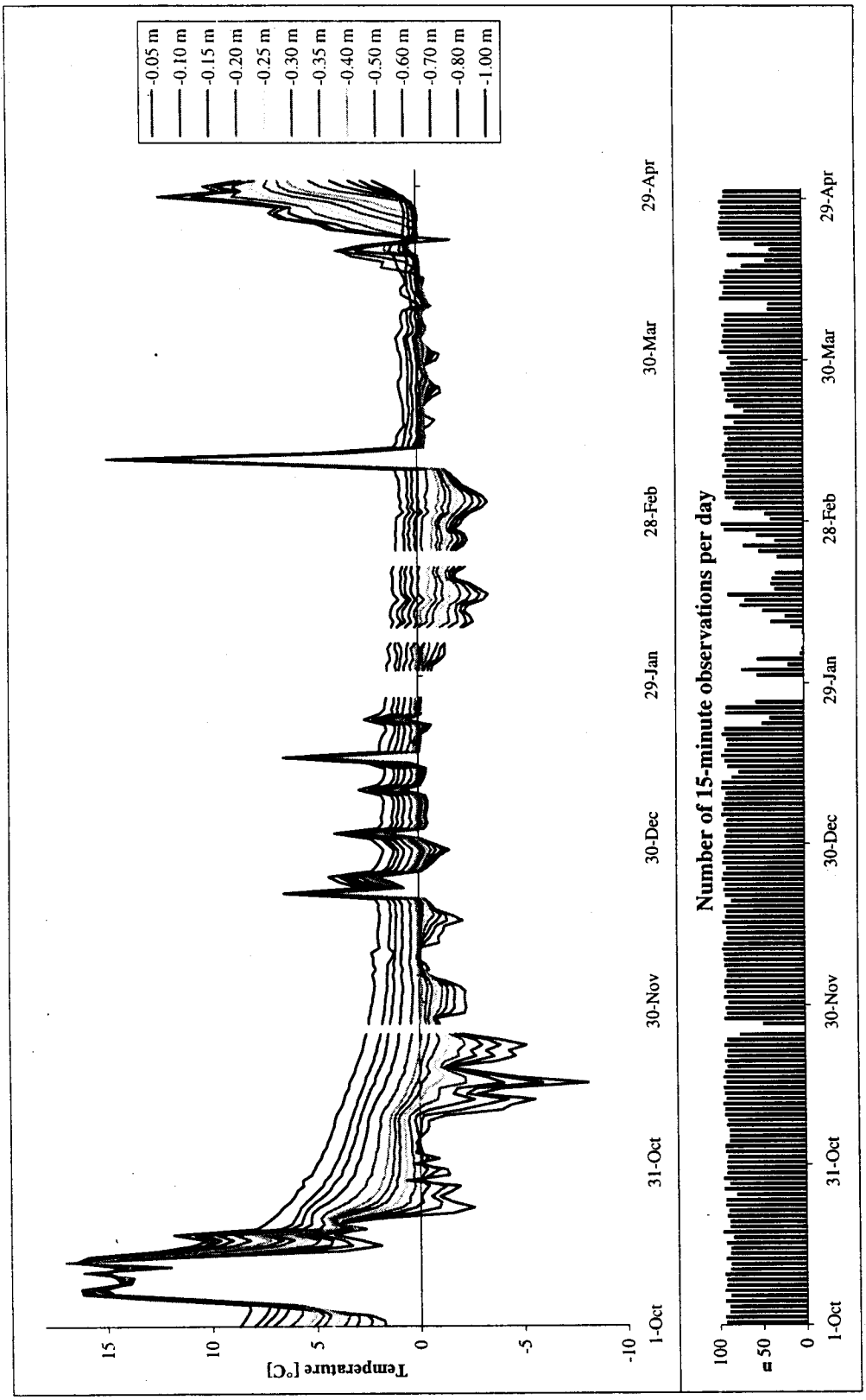

Figure 3.4. Daily average soil temperature profile from October 1 1993 to April 30 1994. Legend indicates height of sensor below soil surface.

3.2.2 Snow Cover Measurements

Figure 3.5 shows the snow cover measurements at the temperature profile site (S7) and Figures 3.6 and 3.7 summarize the areal snow measurements taken near the meteorological station at points S1-S6 (Figure 3.1). The weekly measurements were initiated in late January and continued until early April. The highest snow depths were observed during February and late March. A warm period occurred in the middle of March which resulted in compaction of the snowpack and considerable increase in bulk water density. Fresh snowfall soon after raised the snow depth to near the early winter values. The density measurements indicated slight compaction of the snowpack throughout the winter and extensive compaction during melting. The high measured density values corresponded to high liquid water content in the snow. Figures 3.5 to 3.7 also show the measured thickness of ice or crust layer on the soil surface. The areal measurements in Figures 3.6 and 3.7 indicated extensive variation in snow depth and especially ice layer depth. The variation was due principally to the uneven soil surface partly as a result of autumn plowing. The areal snow cover measurements indicated that the ice layer thickness increased at the lower part of the hillslope during cold periods which preceded snowmelt.

3.2.3 Meteorological Variables

The daily mean values of meteorological data were calculated for the period January to April 1994 of established snow cover. Figure 3.8 shows the daily precipitation which is the sum of the measured hourly precipitation. During late January and February notable breaks occurred in the recorded measurements. Figures 3.9 and 3.10 present the corresponding daily mean values for the variables measured at the meteorological station. The solar radiation indicated a strong seasonal pattern which is consistent with known planetary motion. Air temperature at the meteorological station had the same pattern as the profile temperatures, except there were no erroneous peaks. On the other

hand, the temperature probe at the meteorological station did not measure temperatures below -20 °C. Relative humidity had unrealistically high values during the winter, suggesting that humidity measurements at cold temperatures were biased. Wind speed had consistently low values in early January indicating that the anemometer was malfunctioning.

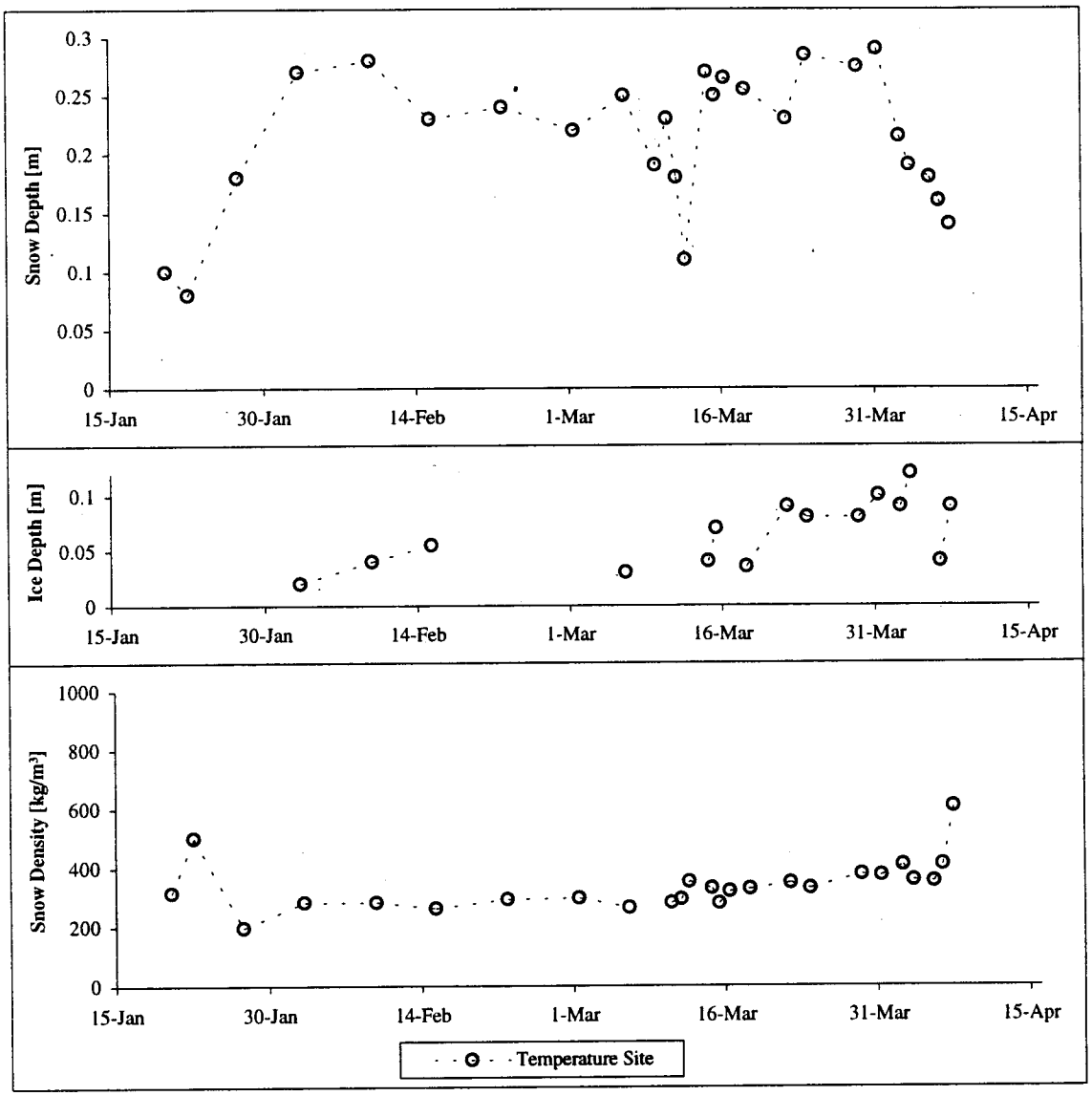

Figure 3.5. Snow depth, density, and ice layer thickness on the soil surface at the temperature profile site during winter 1994. The density of the ice layer was not measured.

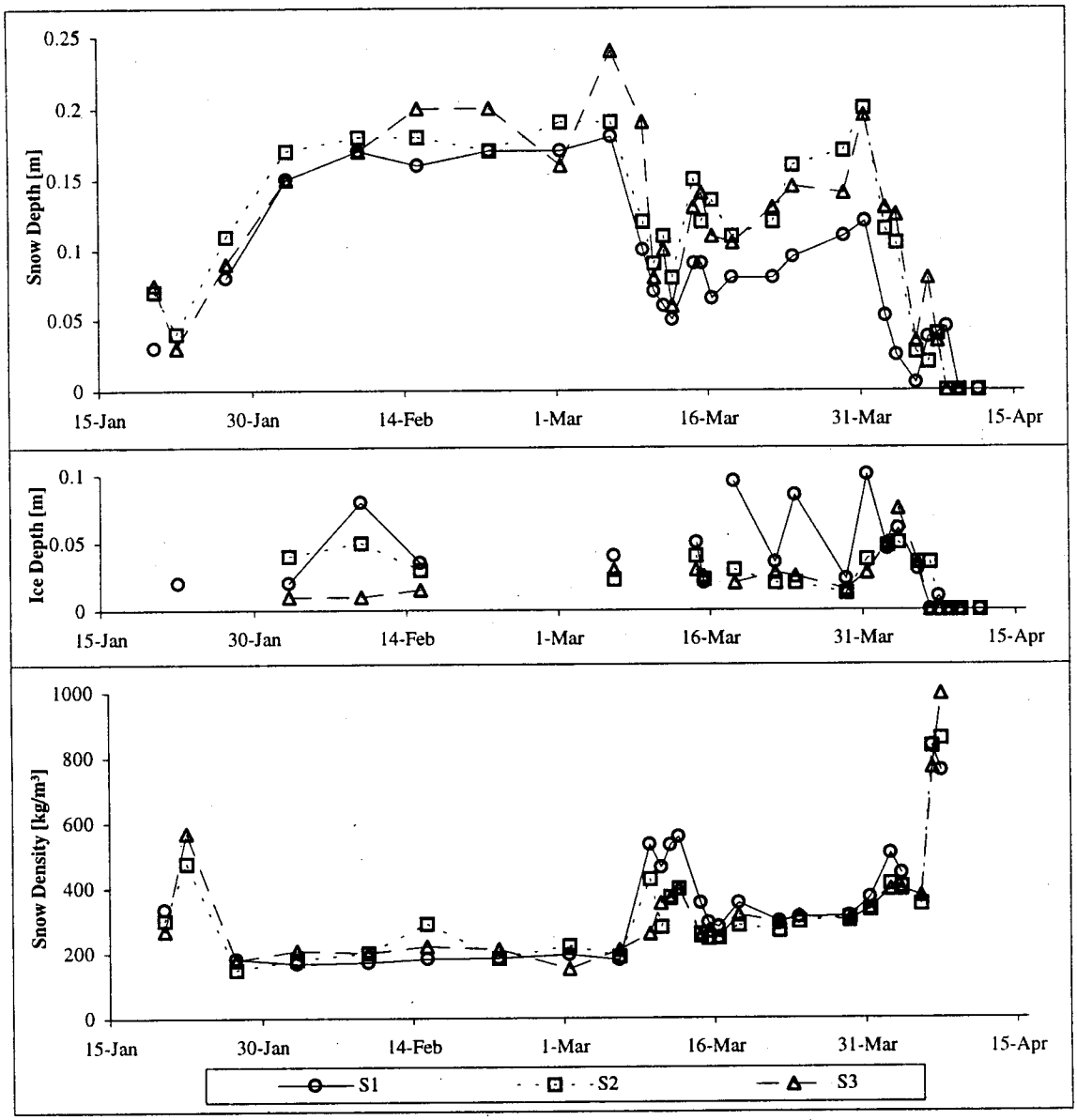

Figure 3.6. Snow depth, density, and ice layer thickness at section 1 near the meteorological station during winter 1994. S1 was located in the lower, S2 in the middle, and S3 in the upper part of the hillslope.

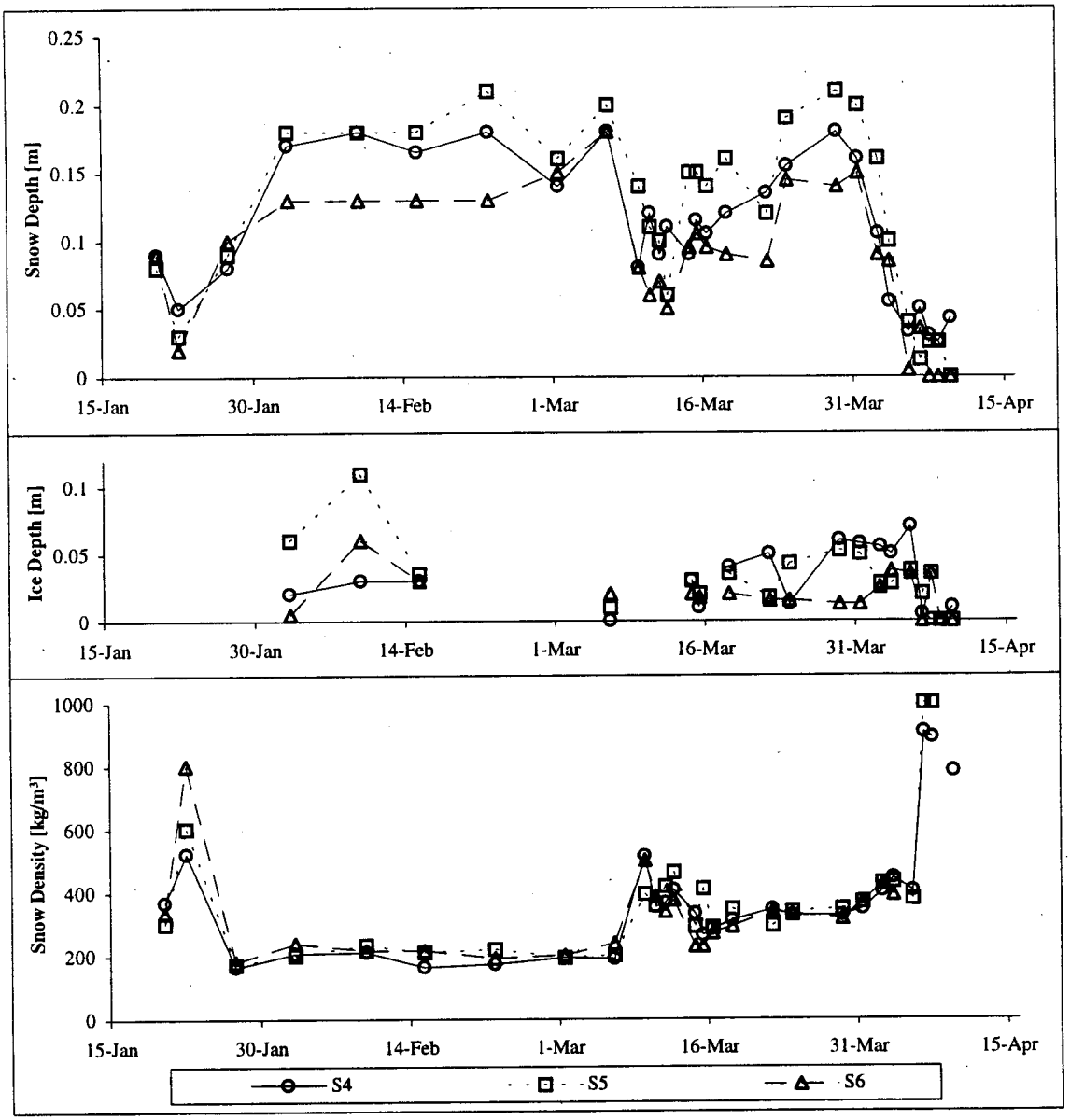

Figure 3.7. Snow depth, density, and ice layer thickness at section 2 near the meteorological station during winter 1994. S4 was located in the lower, S5 in the middle, and S6 in the upper part of the hillslope.

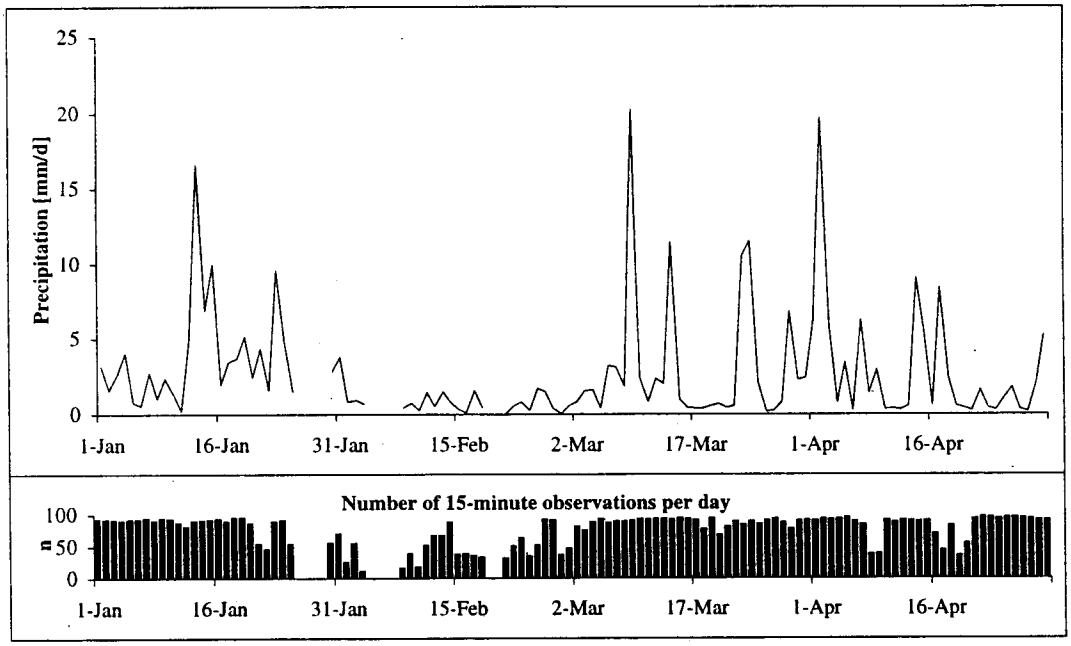

Figure 3.8. Daily precipitation depth at the temperature profile site from January 1 to April 30, 1994.

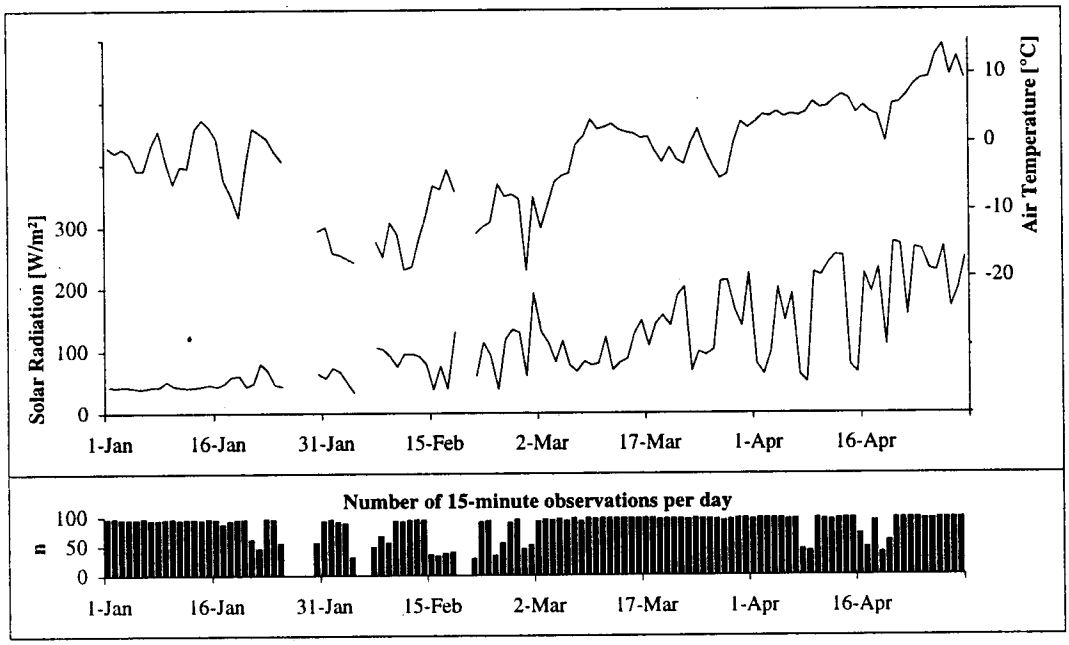

Figure 3.9. Daily average air temperature and solar radiation flux at the meteorological station from January 1 to April 30, 1994.

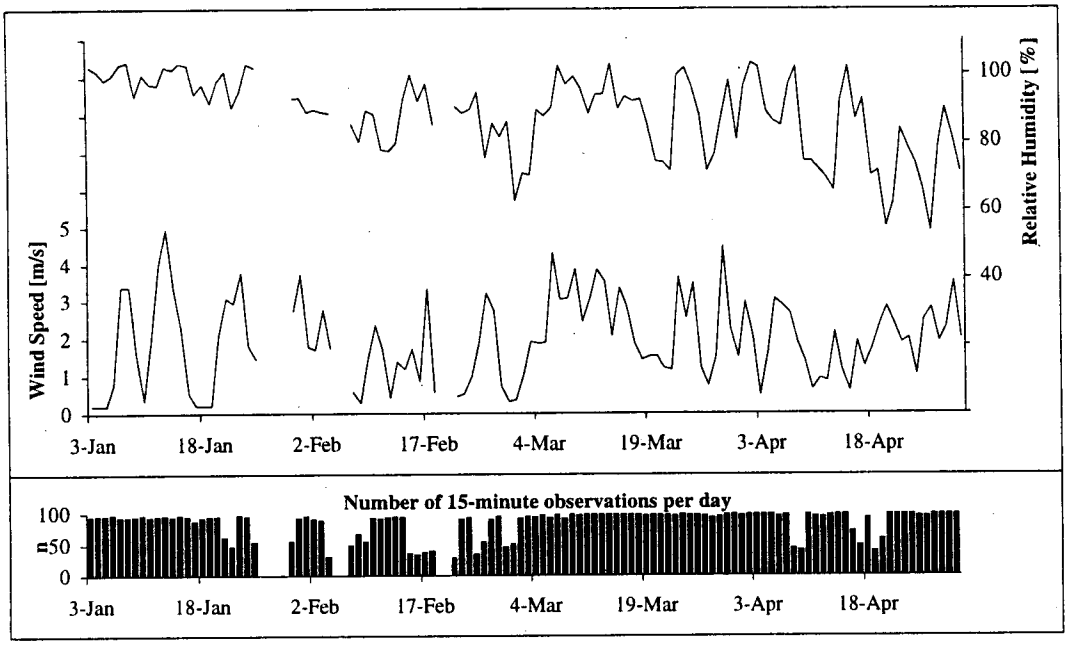

Figure 3.10. Daily average relative humidity and wind speed at the meteorological station from January 1 to April 30, 1994.

3.3 Data Quality Assurance and Quality Control Check

The meteorological data were processed to provide continuous hourly input data for SNTHERM. Missing data were filled in using linear interpolation or estimated using the values for the previous and following days. The data were compared with records from weather stations maintained by the Finnish Meteorological Institute.

3.3.1 Air Temperature

The air temperature measured 1.0 m above the soil surface at the profile site (A in Figure 3.1) was needed as a boundary condition at the air/snow interface. The 15-minute data were used to calculate hourly average temperature. The snow profile temperatures had unrealistically high values after cold periods. Therefore, air

temperature measured at the meteorological station at height 1.8 m was used to correct the high values at site A. Figure 3.11 presents a comparison between the air temperature measured at the meteorological station and at the temperature profile site. The comparison shows close agreement between the two temperatures, except in early March, when the profile temperatures were incorrect. On average, the temperatures at the profile site were slightly colder than the reference air temperature. This was due principally to the difference in the measurement height and the aspect of the two sites: The meteorological site was in the middle of the field, whereas the profile site was located at the bottom of a north facing slope with trees partly shading the hillslope. During cold periods, temperatures below -20 °C were beyond the sensor measurement range at the meteorological station and were not recorded.

If the air temperature at the profile site was greater than that at the meteorological station, the profile site temperature was lowered to the corresponding value at the meteorological station and the past 24 hour average difference between the measured temperatures was subtracted to preserve the mean difference between the sites. Also, if a measurement was available from the meteorological station, but not at the profile site, the station temperature minus the 24-hour average difference was taken as the profile site air temperature.

Missing values were interpolated using the following procedure. For durations less than 4 hours, the missing data were interpolated linearly. Longer periods of missing data were filled in using the average of the nearest previous and next day value corresponding to the same hours. However, if no future value of the corresponding time was found in the next 3 days, only the value of the previous day was used. Figure 3.12 shows the edited air temperatures and the difference from the original values.

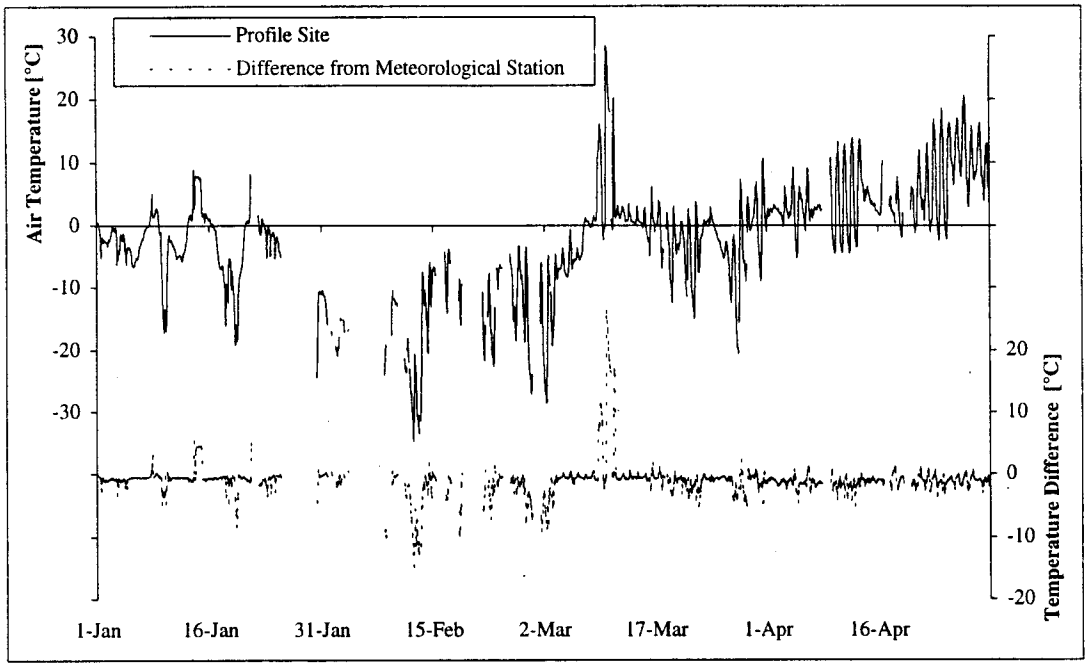

Figure 3.11. Hourly air temperatures measured 1.0 m above the soil surface at the temperature profile site, and the difference from temperature measured 1.8 m from the ground at the meteorological station.

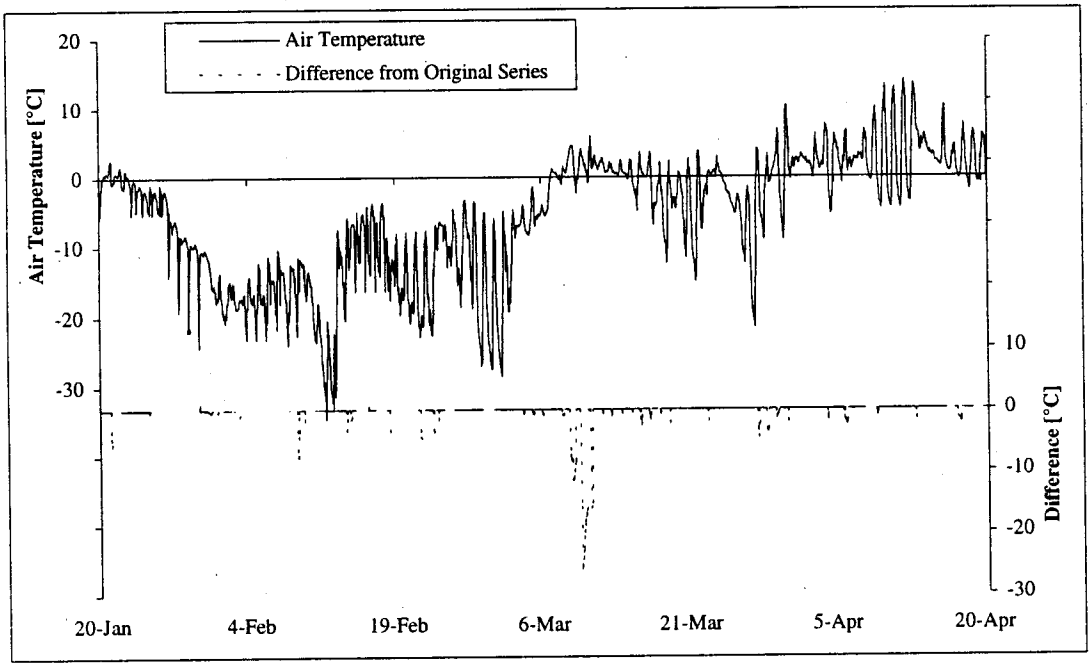

Figure 3.12. Processed hourly air temperature and difference from original values at height 1.0 m above the soil surface at site A, Sjökulla.

The processed air temperature data were compared to daily values measured by the Finnish Meteorological Institute at Kaisaniemi station in Helsinki, and Maasoja station in Vihti. Kaisaniemi station was located about 32 km east of Sjökulla, and Maasoja 20 km to the north, respectively. The daily mean, maximum and minimum air temperatures at the experimental field and at each station are presented in Figures 3.13 and 3.14, and the differences between daily mean temperatures in Figures 3.15 and 3.16. The graphs indicate that the mean temperatures at the stations are in good agreement, except for a few significant deviations during February, when measurement breaks occurred frequently at the snow site. The minimum and maximum temperatures show similar daily variation between Sjökulla and Maasoja. Kaisaniemi station, which was located close to the Gulf of Finland, had lower daily variation in temperature.

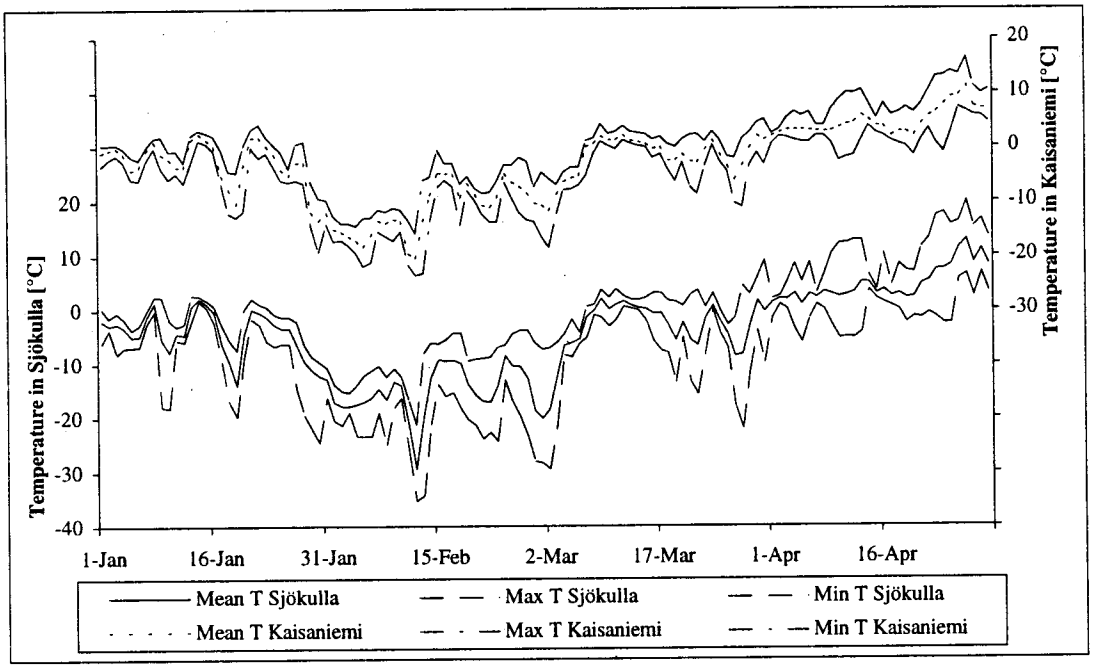

Figure 3.13. Daily mean, maximum, and minimum air temperatures at Sjökulla and Kaisaniemi, winter 1994.

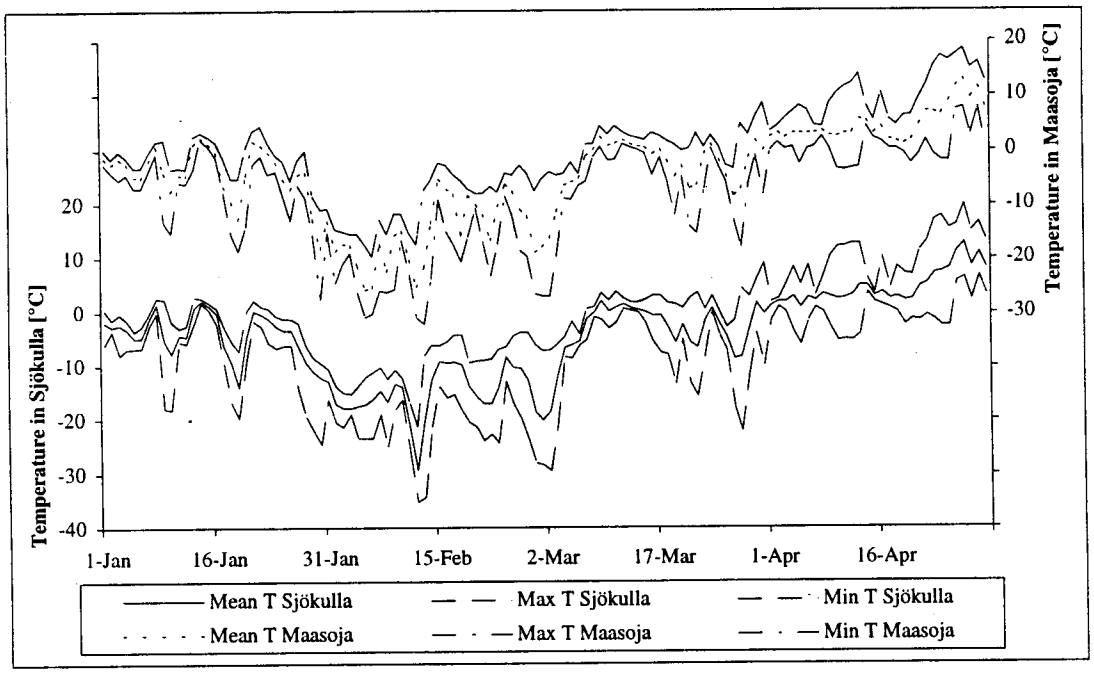

Figure 3.14. Daily mean, maximum, and minimum air temperatures at Sjökulla and Maasoja, winter 1994.

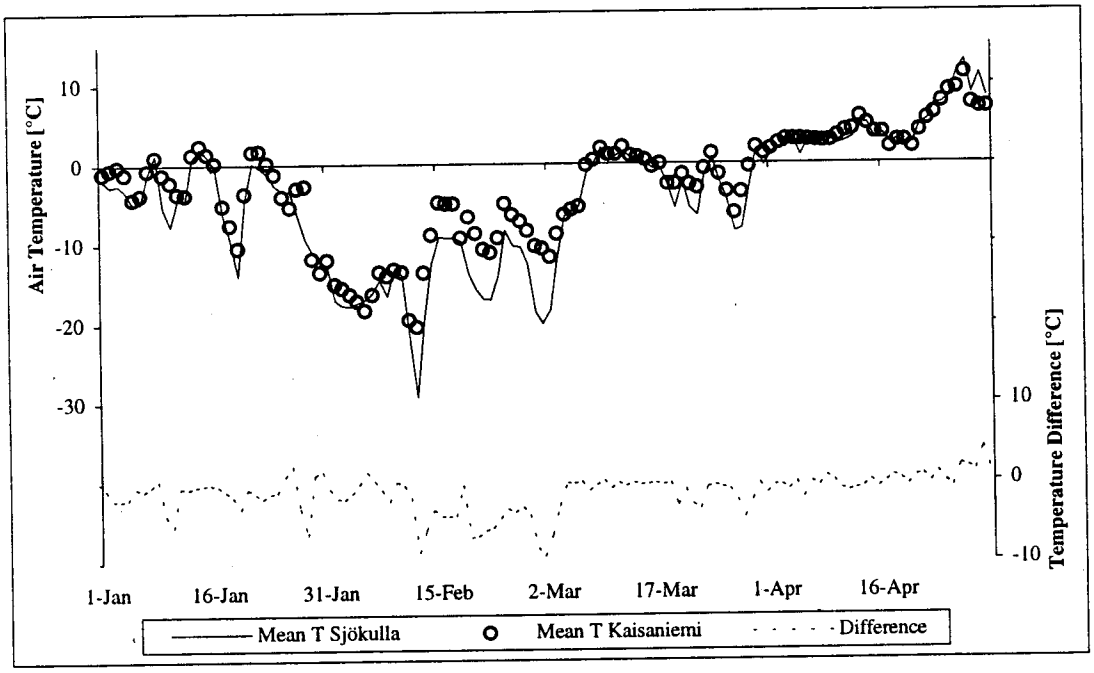

Figure 3.15. Mean daily air temperatures at Sjökulla and Kaisaniemi and their difference, winter 1994.

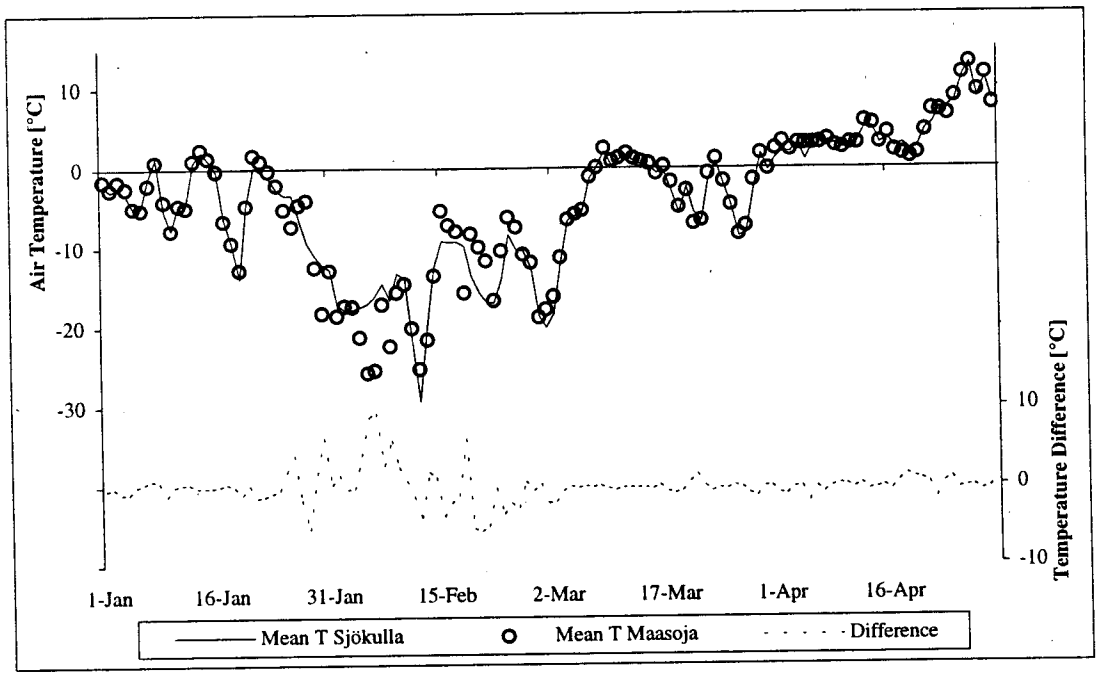

Figure 3.16. Mean daily air temperatures at Sjökulla and Maasoja and their difference, winter 1994.

3.3.2 Radiation

Instrument calibration during summer 1995 indicated that the pyranometer in Sjökulla had a systematic upward bias of about 40 W m^{-2}. The data were corrected by subtracting 40 W m^{-2} from all hourly average radiation values. Missing data were estimated in the same way as the air temperature data by using interpolation or values from the previous and following days. The processed short-wave radiation data and the difference between the edited and the original data are shown in Figure 3.17.

The monthly weather reports by the Finnish Meteorological Institute include daily global radiation measured at the Helsinki-Vantaa Airport located 33 km east of Sjökulla field. The reported global radiation data (direct and diffuse solar radiation) were compared to the global short-wave radiation measurements in Sjökulla. Figure 3.18 indicates good

agreement between daily mean solar radiation values at both sites. The most notable differences occurred in February because of long periods of filled-in data at Sjökulla.

An approach similar to Abdulla (1995) was used for calculating long-wave radiation, which was based on measured air temperature, cloudiness and vapor pressure. However, since cloudiness was not measured at Sjökulla, it was estimated using an index of the ratio of measured and simulated clear sky solar radiation (see e.g., Anderson and Baker 1967). Hourly clear sky radiation was calculated using the approach of Jensen et al. (1990, p. 291-292). Extraterrestrial radiation to the atmosphere was estimated as:

$$R_{ah} = [12(60)/\pi] G_{sc} d_r \{cos(\phi_l) cos(\delta)[sin(\omega_2) - sin(\omega_1)] + (\omega_2 - \omega_1) sin(\phi_l) sin(\delta)\} \quad (3.1)$$

where

R_{ah} = hourly extraterrestrial radiation [MJ m^{-2}]

G_{sc} = solar constant [MJ m^{-2} min^{-1}]

d_r = relative distance of the earth from the sun

ϕ_l = station latitude [rad]

δ = declination angle [rad]

ω = solar time angle (afternoon positive, morning negative) [rad]

ω_1 = solar time angle at the end of the hourly period (= ω - $\pi/24$) [rad]

ω_2 = solar time angle at the beginning of the hourly period (= ω + $\pi/24$) [rad]

Hourly values of the clear sky radiation were estimated as:

$$R_{soh} = (\tau_b + \tau_d) R_{ah} \quad (3.2)$$

where

R_{soh} = hourly clear sky solar radiation [MJ m^{-2}]

and

$$\tau_b = a_0 + a_1 e^{-[K/\cos(\theta_z)]} \quad (3.3)$$

$$\tau_d = 0.2710 - 0.2939\tau_b \quad (3.4)$$

where

τ_b = atmospheric transmittance of direct-beam short-wave radiation

τ_d = atmospheric transmittance of diffuse short-wave radiation

θ_z = zenith angle [rad]

a_0, a_1 = empirical parameters

The simulated clear sky radiation in Sjökulla (latitude N 60°14'31", longitude E 24°23'07") was significantly lower than the measured clear sky radiation. Therefore, the hourly values in (3.2) were increased by 20 % to provide reasonable comparison between simulated and measured clear sky radiation. In this case, the measured solar radiation was believed to be correct, since it was close to the global radiation values reported by the Finnish Meteorological Institute (1994). One reason for the low values given by (3.2) is the seasonal variation in the atmospheric transmissivity, which is lower during winter than during summer due to zenith-angle dependence (Gray and Prowse 1992). Figure 3.19 shows the simulated extraterrestrial and clear sky, and measured daily mean radiation values.

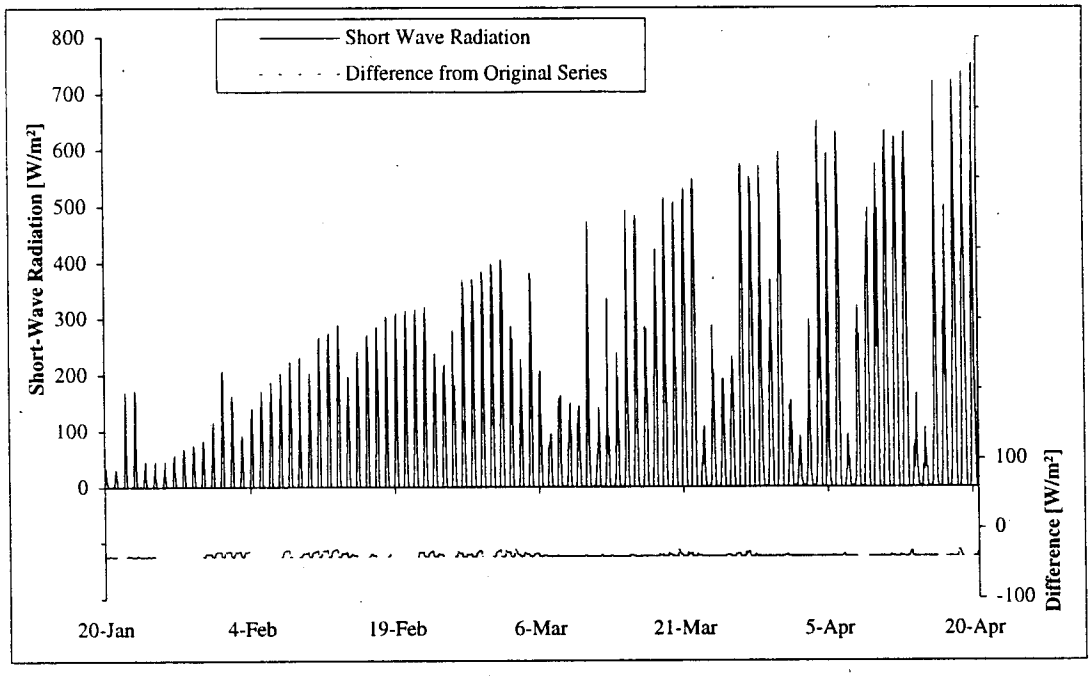

Figure 3.17. Processed hourly solar radiation and difference from original values recorded 1.8 m above ground at site B, Sjökulla.

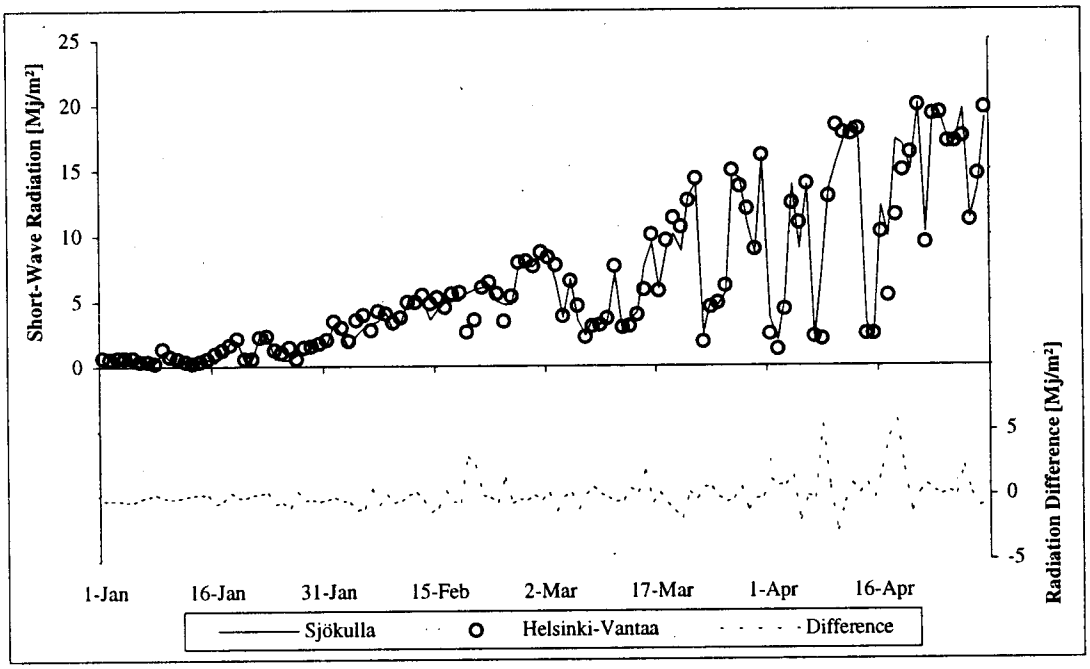

Figure 3.18. Mean daily solar radiation at Sjökulla and Helsinki-Vantaa Airport and their difference, winter 1994.

The cloudiness index was calculated during daytime hours as:

$$C_h = 1 - \left(\frac{R_{meas}}{R_{soh}} \right)^3 \tag{3.5}$$

where

C_h = hourly cloudiness index

R_{meas} = hourly measured solar radiation [MJ m^{-2}]

The night time cloudiness values were estimated by linear interpolation between the average cloudiness in the previous and the following days. Finally, the estimated index was smoothed using a 6-hour moving average. The smoothing was performed to reduce the high variability in the cloudiness index corresponding to low solar zenith angles. Figure 3.20 presents the calculated cloudiness index together with air temperature at the Sjökulla meteorological station. The curve shows that on average, the index has low values when day- and night-time air temperatures fluctuate considerably. The fluctuation in cloudiness index during February results largely from the use of filled-in data.

The monthly weather reports by the Finnish Meteorological Institute listed daily sunshine hours and monthly values for mean cloudiness at the Helsinki-Vantaa Airport. Since the sunshine hours in Sjökulla were not observed, an estimate of sunshine hours was calculated as:

$$S_d = \overline{\left(\frac{R_{meas}}{R_{soh}} \right)^3} S_d^* \tag{3.6}$$

where

S_d = daily sunshine hours

S_d^* = hours per day with solar radiation exceeding 1 W m^{-2}

The overbar in (3.6) indicates an average value over the day. Figure 3.21 shows calculated and reported sunshine hours. Since the sunshine hours were based on the measured solar radiation, the form of the curve is similar to the solar radiation in Figure 3.18. The calculated sunshine hours follow the observed average trend at Helsinki-Vantaa, but the short-term variability is not replicated. Figure 3.22 compares the monthly average cloudiness index in Sjökulla to the reported values at Kaisaniemi and Maasoja stations. The agreement is good except in February, the month with the greatest amount of filled-in data.

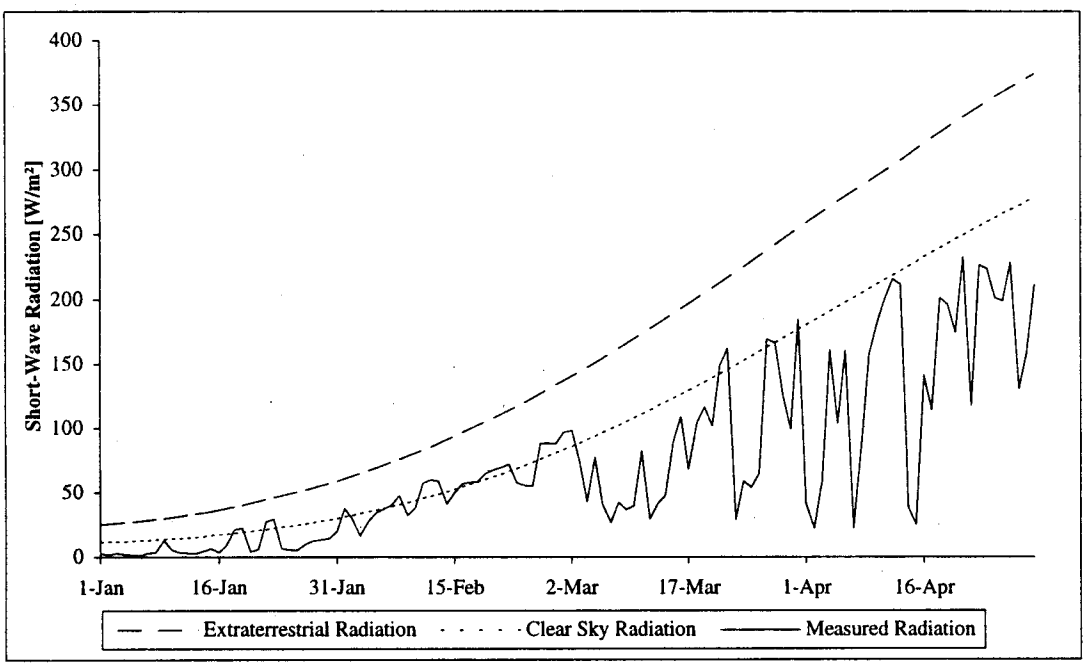

Figure 3.19. Simulated daily average extraterrestrial, clear sky, and measured short-wave radiation at Sjökulla, winter 1994.

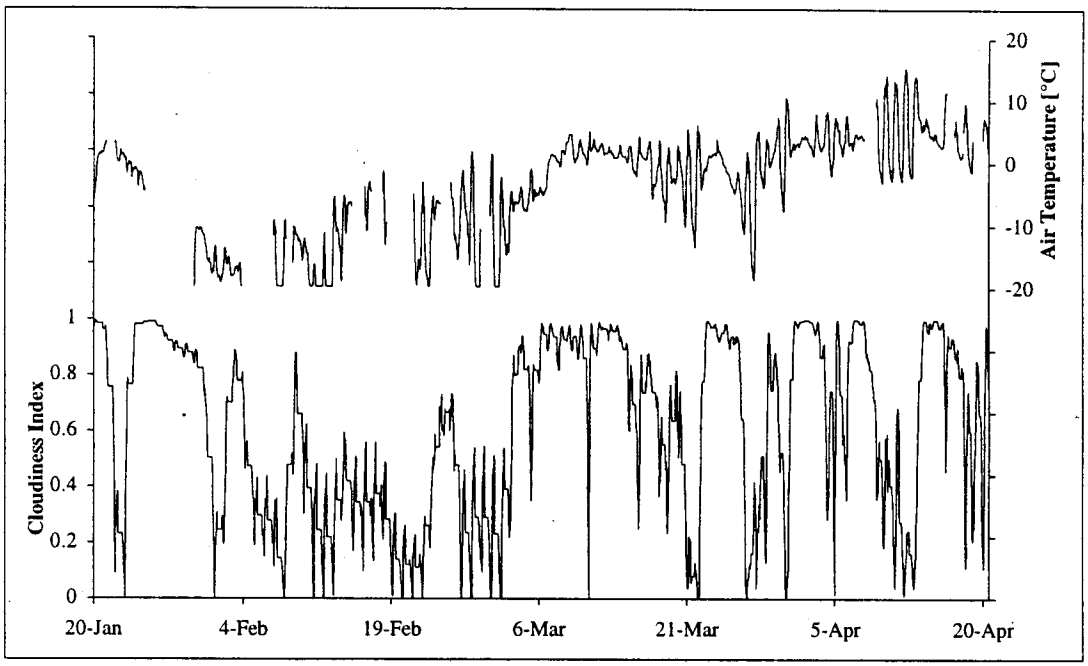

Figure 3.20. Calculated cloudiness index and hourly air temperature at Sjökulla meteorological station, winter 1994.

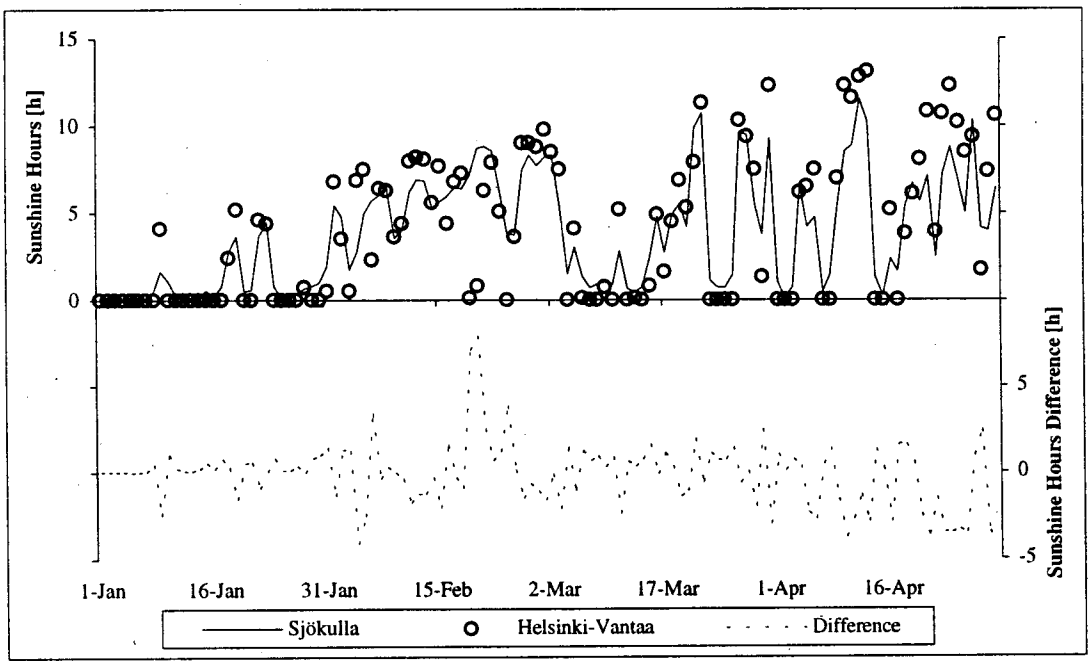

Figure 3.21. Calculated and reported daily sunshine hours at Sjökulla and Helsinki-Vantaa Airport and their difference, winter 1994.

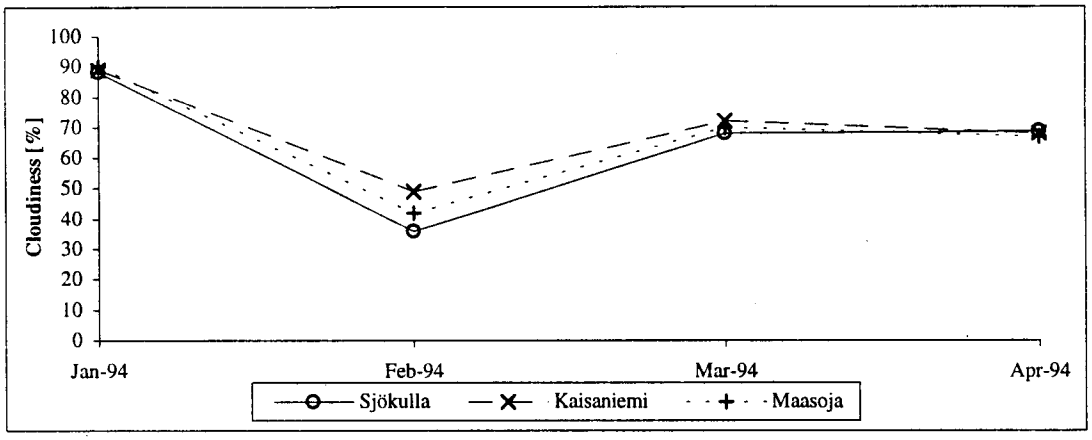

Figure 3.22. Monthly average calculated and reported cloudiness index at Sjökulla and Kaisaniemi and Maasoja stations.

Long-wave radiation is estimated using Equation (2.42) from Bras (1990):

$$I_{ir} = \left(1 + 0.17C_h^2\right)\varepsilon_a \sigma T_a^4 \tag{3.7}$$

I_{ir} = downward long-wave radiation [W m^{-2}]

ε_a = clear sky atmospheric emissivity (= 0.757)

σ = Stefan-Boltzmann constant [W m^{-2} °K^{-4}]

T_a = air temperature at 2 m elevation [°K]

Equation (3.7) was developed by TVA (1972). Figure 3.23 presents the estimated downward long-wave radiation for January-April 1994. The radiation followed the overall pattern of temperature with the lowest values occurring during the coldest weather in February.

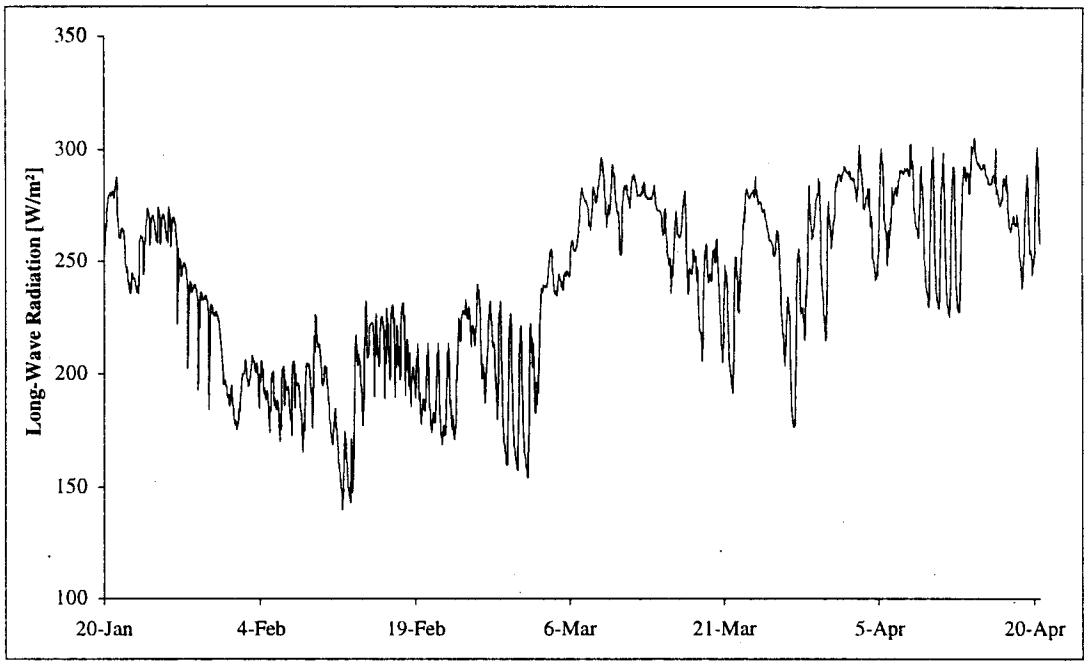

Figure 3.23. Calculated hourly downward long-wave radiation at Sjökulla.

3.3.3 Precipitation

Precipitation is based on the hourly average value of the cumulative weight of the recording container. The resistance signal of the precipitation weigh included small random fluctuation, which most likely resulted from wind induced vibrations. The hourly average of this signal contained both system noise and precipitation signal. Whenever the forward first difference (1-hour increment) was less than 0.5 mm h^{-1}, the accumulated precipitation for that 1-hour period was set to zero. This simple scheme caused some actual recorded precipitation to be omitted. Precipitation that occurred during system failures was accounted for in the first measurement after the break. No correction was used in the measured snowfall or rainfall. Figure 3.24 presents the hourly precipitation and the difference between the original and processed values.

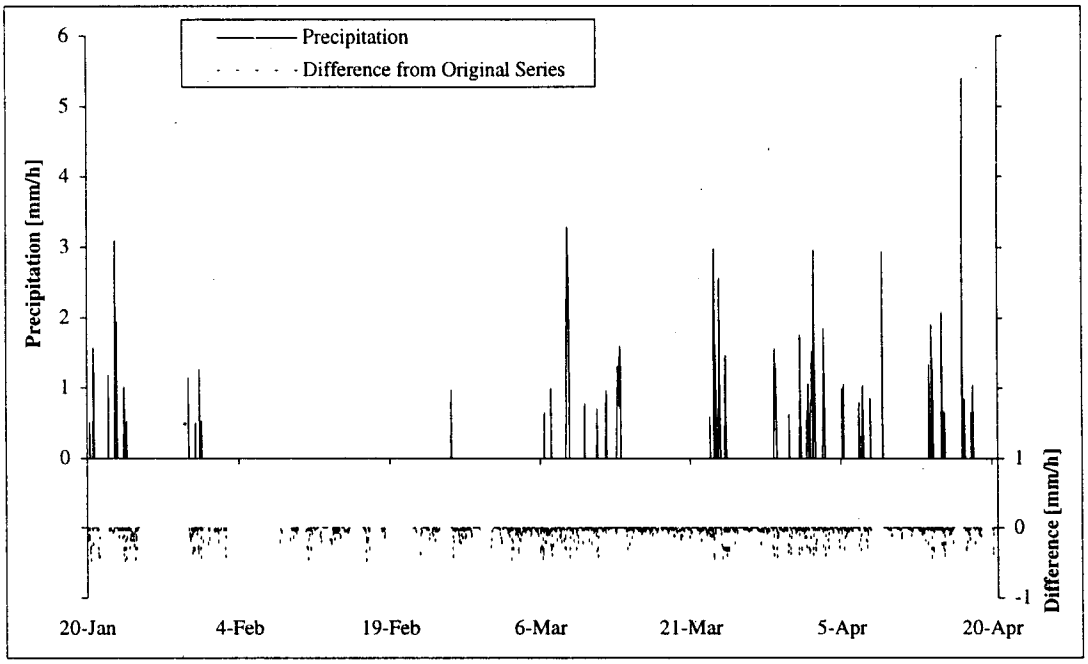

Figure 3.24. Processed hourly precipitation and difference from original values at site A, Sjökulla.

Figure 3.25 shows the cumulative precipitation at Sjökulla and Kaisaniemi and Maasoja stations. The graph shows good agreement between the cumulative series after smaller than 0.5 mm h^{-1} precipitation values at Sjökulla are removed. Close examination shows that the snowfall at Sjökulla is less and rain higher than the values at Maasoja. This suggests that the catch efficiency of the container is different for snow and rain, but the difference cannot be quantified fully from the short-duration record.

The classification of precipitation at Sjökulla (snowfall or rain) is based on the dew point temperature, which was calculated using water vapor pressure. The saturation water vapor pressure over ice is approximated as (Anderson 1976):

$$e_i = 3.5558 \cdot 10^9 e^{(-6141.9/T)} \qquad (3.8)$$

where

e_i = saturation water vapor pressure over ice [kPa]

T = air temperature [°K]

and over water as (Jensen et al. 1990):

$$e_w = e^{\left[(16.78(T-273.15)-116.9)/(T-35.85)\right]} \tag{3.9}$$

where

e_w = saturation water vapor pressure over water [kPa]

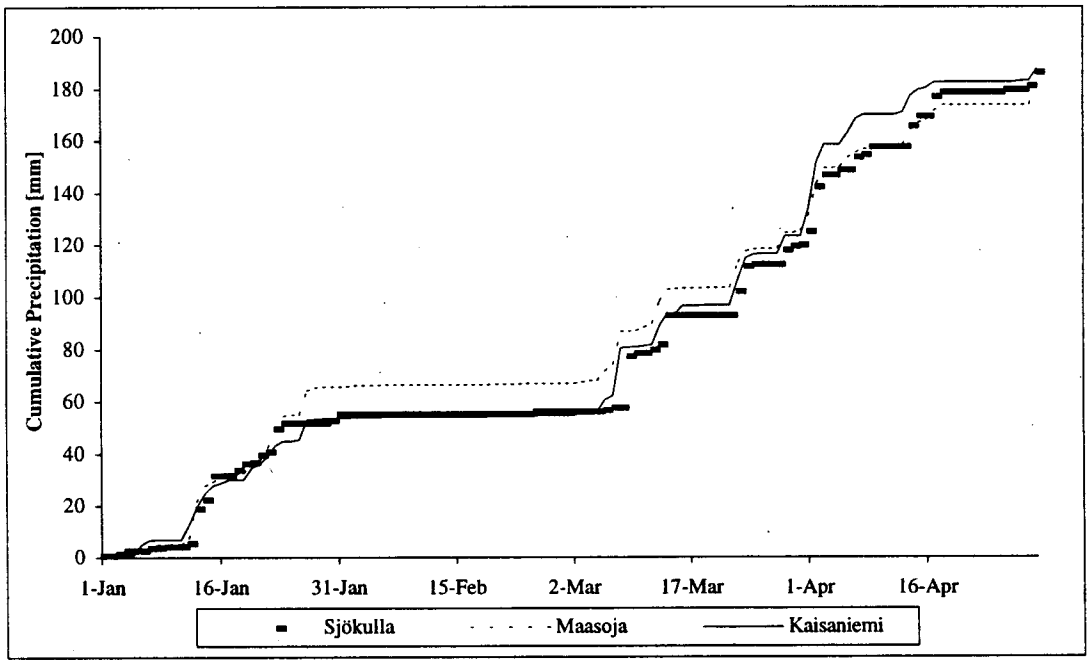

Figure 3.25. Measured mean daily cumulative precipitation at Sjökulla and Kaisaniemi and Maasoja stations, winter 1994.

Equation (3.9) was used for air temperatures greater than 0 °C, and (3.8) for temperatures below 0 °C, respectively. The water vapor pressure is approximated as:

$$e_d = \frac{R_h}{100} e_0 \tag{3.10}$$

where

e_d = water vapor pressure [kPa]

e_0 = saturation water vapor pressure at air temperature (over water or ice) [kPa]

R_h = relative humidity [%]

Using the vapor pressure, e_d, from (3.10), the dew point temperature is calculated by solving for temperature in (3.8) or (3.9). If the dew point temperature is less than 1 °C, precipitation is assumed to be in the form of snow, otherwise rain. Figure 3.26 compares the estimated form of precipitation at Sjökulla with the observed form at Maasoja.

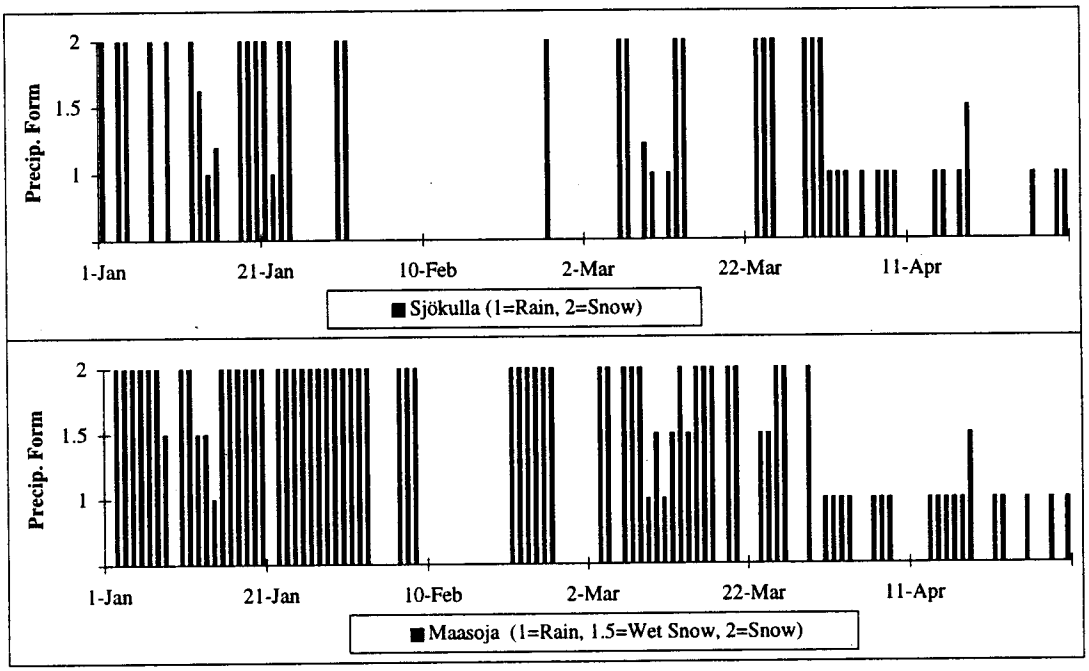

Figure 3.26. Estimated daily average precipitation form at Sjökulla and measured precipitation form at Maasoja station, winter 1994.

3.3.4 Relative Humidity

The calibration of the various measurement devices at Sjökulla during the summer of 1995 indicated a systematic error of 5 % in the relative humidity sensor. Therefore, all relative humidity values were lowered by 5 %. Missing values were interpolated in a similar fashion to temperature and radiation. The processed hourly relative humidity data are presented in Figure 3.27. Figure 3.28 compares the monthly mean relative humidity at Sjökulla and Kaisaniemi. The monthly values differ somewhat in January and February, but the overall agreement is close.

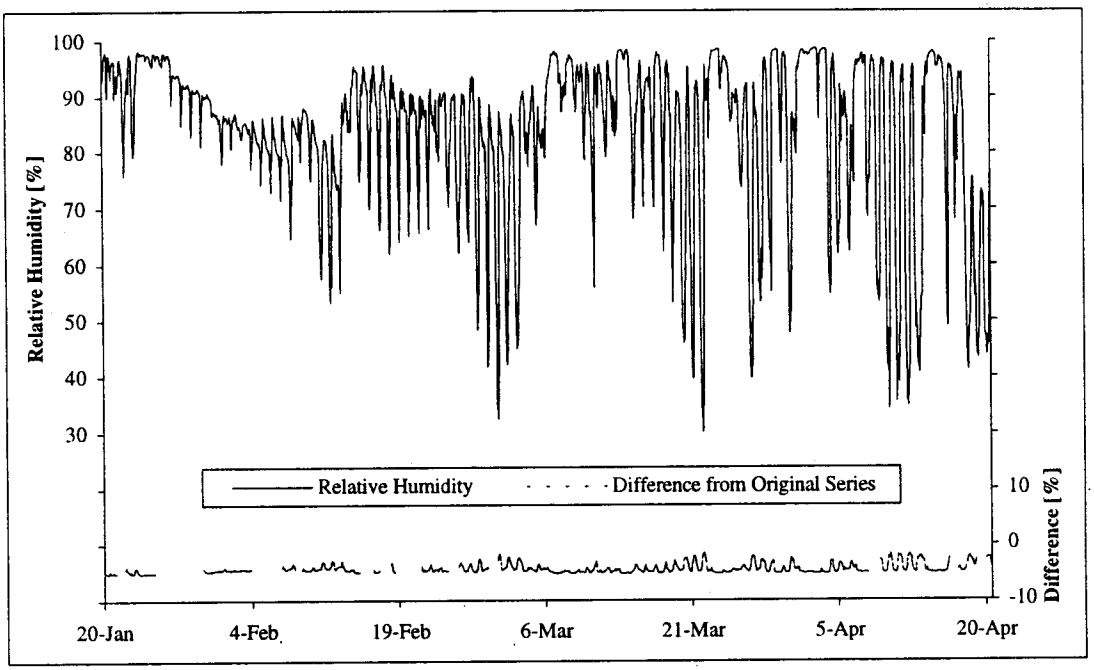

Figure 3.27. Processed hourly relative humidity and difference from original values at site B, Sjökulla.

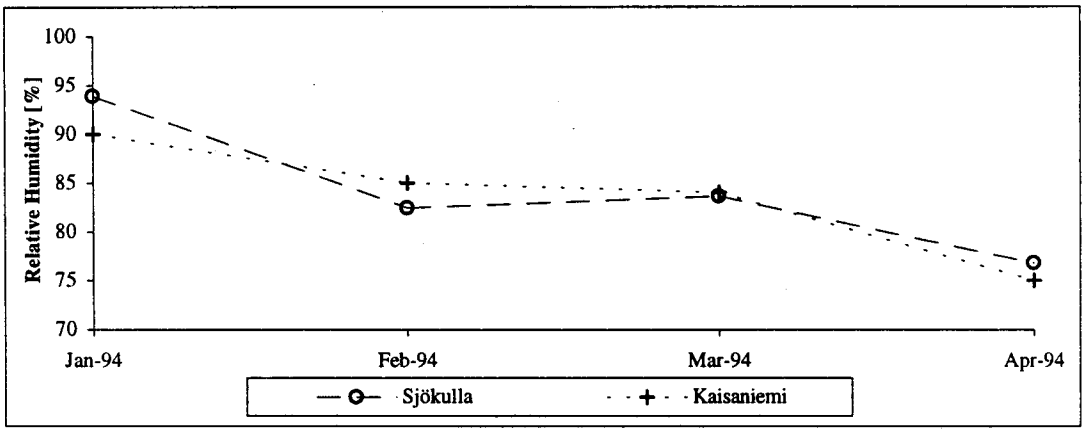

Figure 3.28. Monthly average relative humidity at Sjökulla and Kaisaniemi station, winter 1994.

3.3.5 Wind Speed

During calm periods, the anemometer registered a wind magnitude of 0.2 m s^{-1} as the lowest wind speed, which was set to zero. Missing wind speed values were interpolated using a 24-hour moving average around the missing measurement. If the measurement break was longer than 12 hours, the previous 12 hours were used in calculating the average until measured values were available during the next 12 hours. Figure 3.29 presents the hourly wind speed values, and Figure 3.30 compares the Sjökulla monthly average wind speed to the reported values at the Helsinki-Vantaa Airport and Jokioinen station which is located 80 km north-east of Sjökulla. The reported wind speeds at Helsinki-Vantaa Airport and Jokioinen (height 2.0 m) were adjusted to correspond the measurement height (1.8 m) in Sjökulla using the relationship:

$$\frac{u_1}{u_2} = \left(\frac{z_1}{z_2}\right)^{1/5} \tag{3.11}$$

where

u_1 = wind speed measured at elevation z_1 [m s^{-1}]

u_2 = desired wind speed at elevation z_2 [m s^{-1}]

The wind speeds in Figure 3.30 at Sjökulla are considerably lower than at the other stations. The January value is notably low, since the anemometer was out of operation during the first days of the month. The overall difference results from the influence of small hills and forest near the meteorological station in Sjökulla. Since wind speed near the ground may vary considerably depending on the location, the values were not edited to correspond to the reported averages at either Helsinki/Vantaa or Jokioinen.

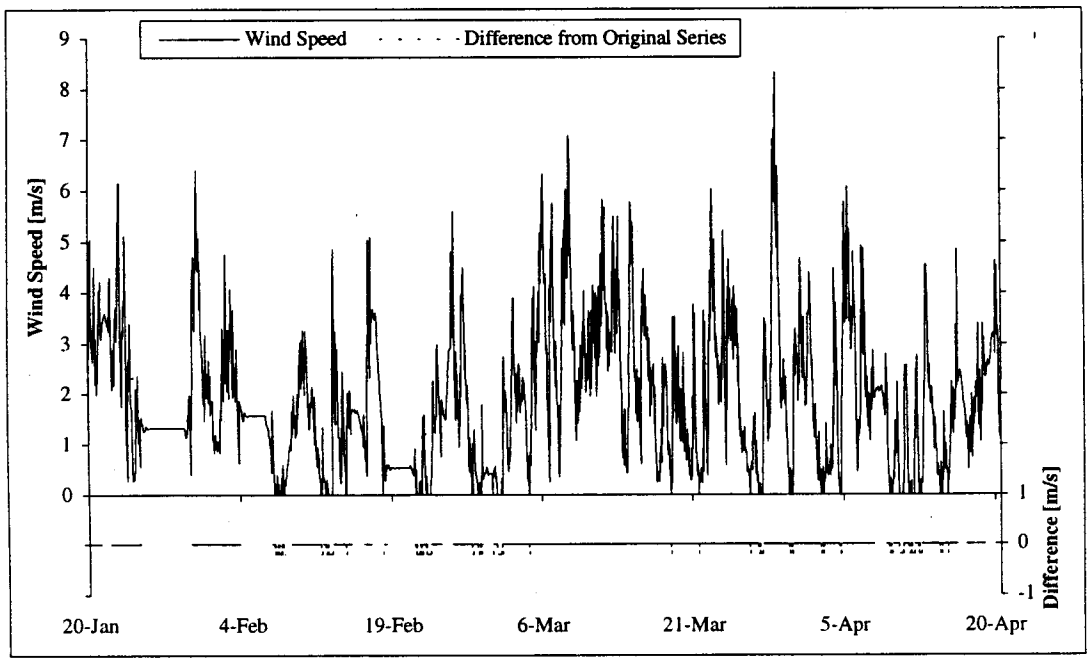

Figure 3.29. Processed hourly wind speed and difference from original values at site B, Sjökulla.

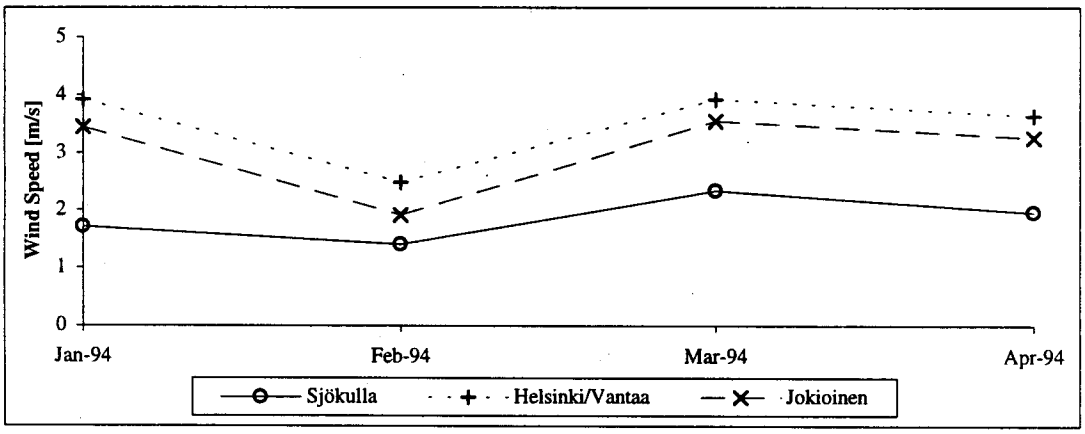

Figure 3.30. Monthly average wind speed at Sjökulla and Helsinki/Vantaa Airport and Jokioinen, winter 1994.

3.3.6 Snow Water Equivalent

Based on the snow cover measurements, snow depth and water equivalent were calculated taking into account both the soft snow and the ice layer immediately above the soil surface. If only the soft snow measurement was available, the missing ice layer thickness was estimated by linear interpolation between the nearest measurements in time. In the calculation of the overall snow water equivalent, the ice, or the crust layer was assumed to have a density of 500 kg m^{-3}. The areal average snow/ice depth and water equivalent estimates were based on the six measurements at points S1-S6 (Figure 3.1). Figure 3.31 shows the combined snow and ice layer depth at the temperature profile site and the average depth near the meteorological station together with four reported values from Kaisaniemi and Maasoja. The snow water equivalent at the profile site and the areal average near the meteorological station are shown in Figure 3.32.

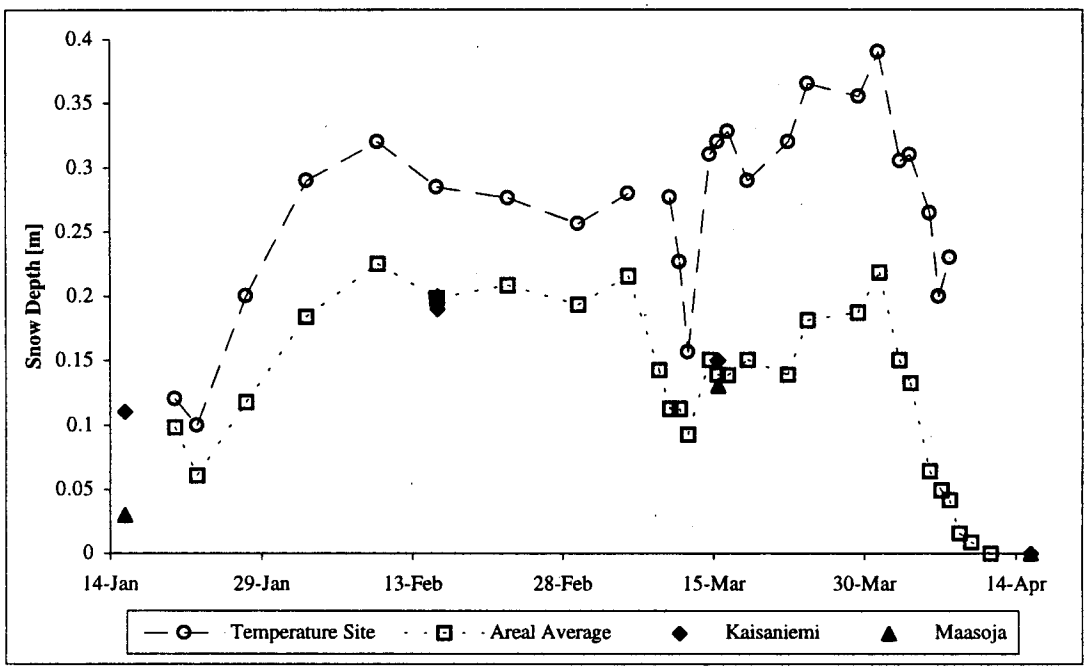

Figure 3.31. Combined snow and ice depth at the Sjökulla temperature profile site, spatial average depth over two field sections near the meteorological station, and reported snow depth from Kaisaniemi and Maasoja, winter 1994.

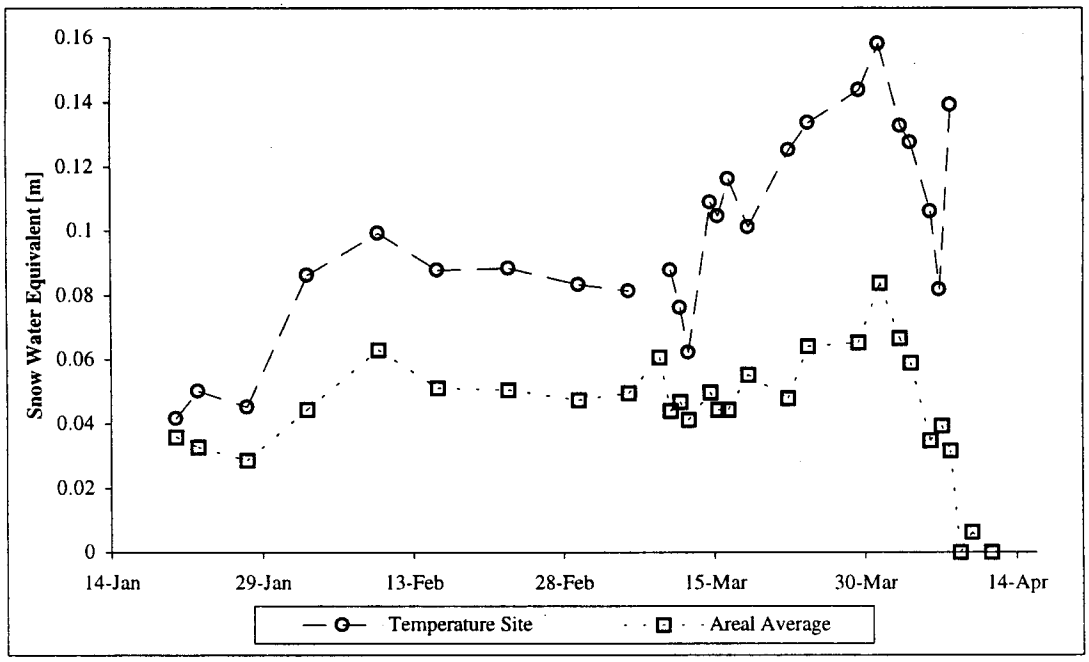

Figure 3.32. Snow water equivalent at the Sjökulla temperature profile site and estimated spatial average water equivalent over two field sections near the meteorological station, winter 1994.

The areal average snow depth is in good general agreement with the measurements at the Kaisaniemi and Maasoja. However, the snow depth and water equivalent at the profile site are considerably higher than the areal average, which suggests that snow drifted and accumulated at the lowest part of the hillslope at the profile site. The mass differences between the two locations at Sjökulla started during February and again in early March after a short period of melting. The origin of the drifted snow to the profile site was not obvious. According to the reports of the Finnish Meteorological Institute (1994), the main wind direction in Southern Finland varied during February from between east and west (Figure 3.33), and was from the south during March, 1994 (Figure 3.34). Therefore, snow may have been blown across the fallow field during February. During March, extra snow may have been deposited from trees located south of the profile site. The snow water equivalent (Figure 3.32) indicates that the melting period in early March did not result in significant runoff, since most of the meltwater was held in the snow. The snow water equivalent reached its maximum value before the final melting period began in early April.

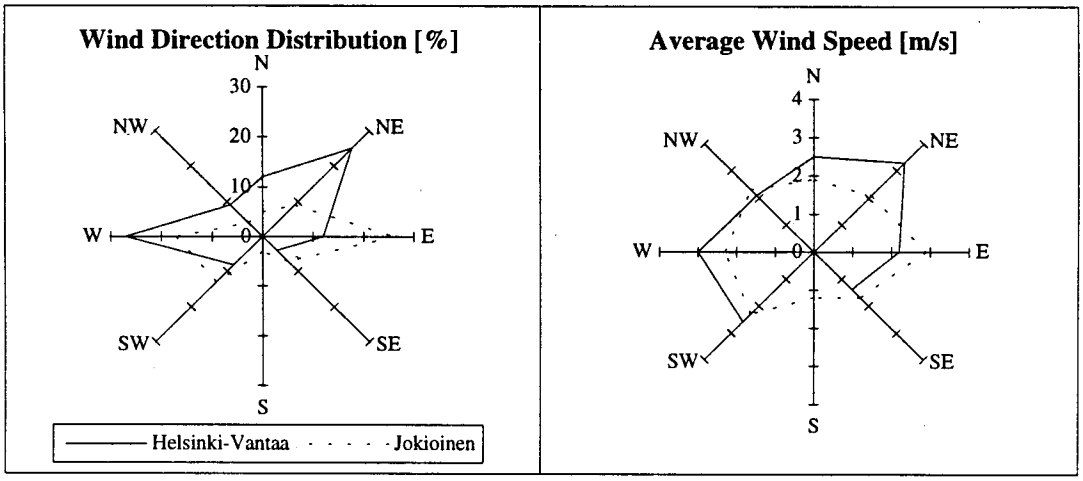

Figure 3.33. Average wind direction and wind speed distribution at Helsinki-Vantaa Airport and Jokioinen station, February 1994.

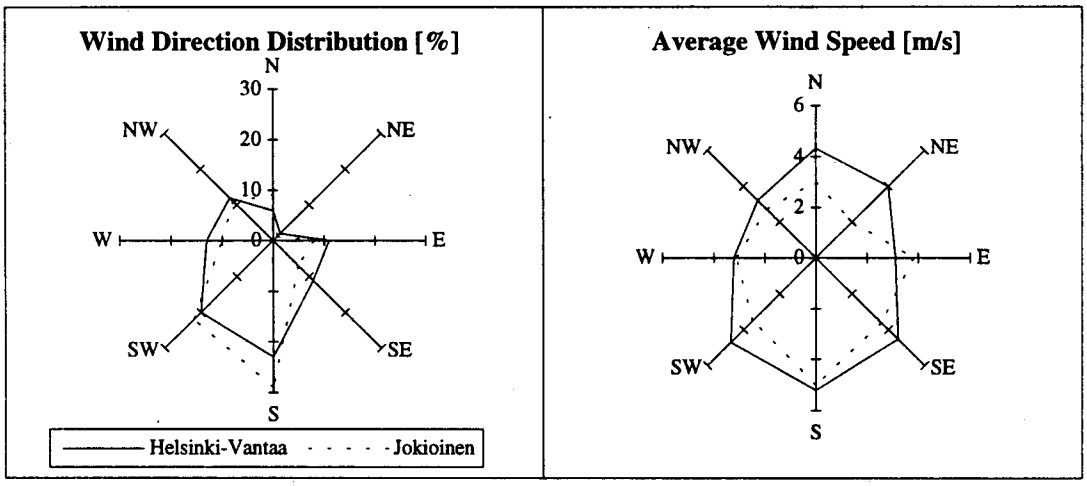

Figure 3.34. Average wind direction and wind speed distribution at Helsinki-Vantaa Airport and Jokioinen station, March 1994.

Chapter 4 Application of SNTHERM Using the Sjökulla Data Set

SNTHERM was used in two stages: First, the measured snow depth and water equivalent were simulated for January to April, 1994, to check the mass balance. Additional mass was added to the precipitation time series at the temperature profile site to approximate plausible snow drifting. Second, the initial condition for the soil profile was adjusted to replicate the measured temporal temperature profiles in the snow and soil. The model parameters were those suggested in the SNTHERM electronic documentation file. The model was calibrated to replicate snow temperature by adjusting only the initial conditions.

4.1 Model Results

4.1.1 Snow Depth and Water Equivalent

Using the meteorological data described in Chapter 3, SNTHERM was run starting from 10:00 a.m. January 20, 1994, which corresponded to the time of the first snow cover measurements. The data had not been collected for use with a model of the form of SNTHERM, so it was necessary to estimate some of the initial states required by the model. The initial conditions are shown in Table 4.1. The initial snow depth and water equivalent were taken to be the areal average measurements near the meteorological station. The number of initial snow layers was chosen to keep the nodal layer thickness small. The thickness of the top node was set to 0.01 m as suggested in the model documentation. The layers near the soil surface were set equal to 0.01 m because of the observed abrupt density change due to surface ice layer. The soil down to a depth of 1.15 m was represented with 15 nodes. Each temperature sensor was located in the middle of a modeled soil layer. The initial temperatures in the snow and the soil were based on the measured profile, except for the bottom node temperature. The bottom

node defined the lower thermal boundary condition (constant temperature), which was set equal to the measured average temperature over most of the winter. The snow density profile was set equal to 200 kg m^{-3} at the surface and allowed to increase with depth such that the total water equivalent corresponded to the estimated value. The initial soil water bulk density was set arbitrarily high to be consistent with the observation that the soil was wet before the onset of surface freezing and snow accumulation. The model documentation suggests that the bulk water density in soil should fall between:

$$\rho_{wl} = 0.75 n_p \rho_d \tag{4.1}$$

where

ρ_{wl} = lower boundary for bulk water density in soil [kg m^{-3}]

ρ_d = bulk dry soil density [kg m^{-3}]

n_p = plasticity number

and

$$\rho_{wu} = \phi \rho_i \tag{4.2}$$

where

ρ_{wl} = upper boundary for bulk water density in soil [kg m^{-3}]

ρ_i = ice density [kg m^{-3}]

ϕ = porosity

The dry density for clay typically ranges from 900 to 1600 kg m^{-3}, and porosity ranges between 15 and 45 % (see e.g., Farouki 1986). The model documentation suggested a plasticity number of 0.25 for clay. Assuming average values, the bulk water density range for the soil was likely to be between 200 and 400 kg m^{-3}. The upper value was chosen here. This corresponded to a uniform initial saturation at each of the soil nodes. Snow grain diameter increases with depth and takes the ranges for new (0.04-0.2 mm), fine-grained (0.2-0.6 mm), and wet snow (2.0-3.0 mm), respectively (e.g., Jordan 1991). Clayey and silty soils are represented with an equivalent grain diameter in the range 10^{-4}-10^{-2} mm; 0.002 mm was used here. The initial model parameter values are given in Table 4.2.

Table 4.1. Initial values in snow and soil layers for the simulation of areal snow cover starting 10:00 a.m. January 20, 1994.

Node	Nodal temperature [K]	Elemental thickness [m]	Nodal water constituents bulk density [kg m^{-3}]	Nodal effective grain diameter [m]
1 (Clay)	274.4	0.3	400	0.000002
2 (Clay)	274.2	0.1	400	0.000002
3 (Clay)	274.0	0.1	400	0.000002
4 (Clay)	273.9	0.1	400	0.000002
5 (Clay)	273.4	0.1	400	0.000002
6 (Clay)	273.2	0.025	400	0.000002
7 (Clay)	273.1	0.05	400	0.000002
8 (Clay)	273.1	0.05	400	0.000002
9 (Clay)	273.1	0.05	400	0.000002
10 (Clay)	273.0	0.05	400	0.000002
11 (Clay)	272.9	0.05	400	0.000002
12 (Clay)	272.8	0.05	400	0.000002
13 (Clay)	272.6	0.05	400	0.000002
14 (Clay)	272.4	0.05	400	0.000002
15 (Clay)	271.7	0.025	400	0.000002
16 (Snow)	271.4	0.01	500	0.002
17 (Snow)	271.2	0.01	480	0.002
18 (Snow)	270.9	0.025	420	0.0015
19 (Snow)	270.6	0.0233	360	0.0006
20 (Snow)	270.0	0.02	270	0.0005
21 (Snow)	269.7	0.01	200	0.0004

Table 4.2. Snow and soil parameters and selected modeling options for the application of SNTHERM at Sjökulla.

Parameter description	Value	
Number of material layers (e.g., snow, clay, sand, etc.)	2	
Print-out interval [h]	1	
Print-out of incident heat fluxes	*yes*	
Average barometric pressure [mb]	1008.0	
Estimate solar radiation	*no*	
Estimate incident long-wave radiation	*no*	
Sloped terrain	*no*	
Snow is compacted (tanktracks)	*no*	
Near infrared extinction coefficient for top snow node	400.0	
Optional input of measured surface temperature data	*no*	
Optional print-out of water infiltration estimates	*no*	
Basic time step of meteorological data [s]	3600.0	
Estimate standard met. data from user-supplied routine	*no*	
Snow albedo	*variable albedo algorithm used*	
Irreducible water saturation for snow	0.04	
A fixed density for new snow	*supplied by user*	
The settling compaction limit [kg m^{-3}]	100.0	
Stability correction for stable atmospheric conditions	*no*	
An alternative turbulent transfer module implemented	*yes*	
Viscosity coefficient [kg s m^{-2}]	900 000	
Air temperature measurement height [m]	1.00	
Wind speed height [m]	1.80	
Dew point or relative humidity height [m]	1.80	
	soil	snow
Number of nodes in material layer	15	8
Material layer type	*clay*	*snow*
Quartz content of layer	0.4	0.0
Roughness length for turbulent transfer of momentum [m]	0.001	0.001
Drag coefficient at neutral stability	*computed by model*	
Ratio of neutral stability bulk turbulent transfer coefficients of momentum and latent heat	1.0	1.0
Ratio of neutral stability turbulent transfer coefficients of momentum and sensible heat	1.0	0.7
Windless exchange coefficient for water vapor	1.00	2.00
Windless exchange coefficient for heat	1.00	2.00
Fractional humidity within medium relative to saturated state	0.98	1.00
Minimum number of consecutive good calculations required before time step can be increased	2	
Minimum allowed time step [s]	5.0	
Minimum allowed time step when water flow is present [s]	1.0	
Maximum allowed time step [s]	900.0	
Maximum time step for saturation criteria [s]	900.0	
Maximum allowed nodal change in saturation per time step	0.02	
Maximum allowed linearization error in heat balance eq. [°K]	0.1	

Figures 4.1 and 4.2 show time series of the calculated and measured average snow depth and snow water equivalent together with the maximum and minimum values from the six snow measurement locations (S1-S6). Taking into consideration the variability in the measured snow depth and the water equivalent, the calculated series follow the measurements reasonably well, except in late January, when the calculated values are considerably higher. This period corresponds to five days of missing meteorological data. However, the general accumulation and especially the melting pattern of the snowpack is well simulated.

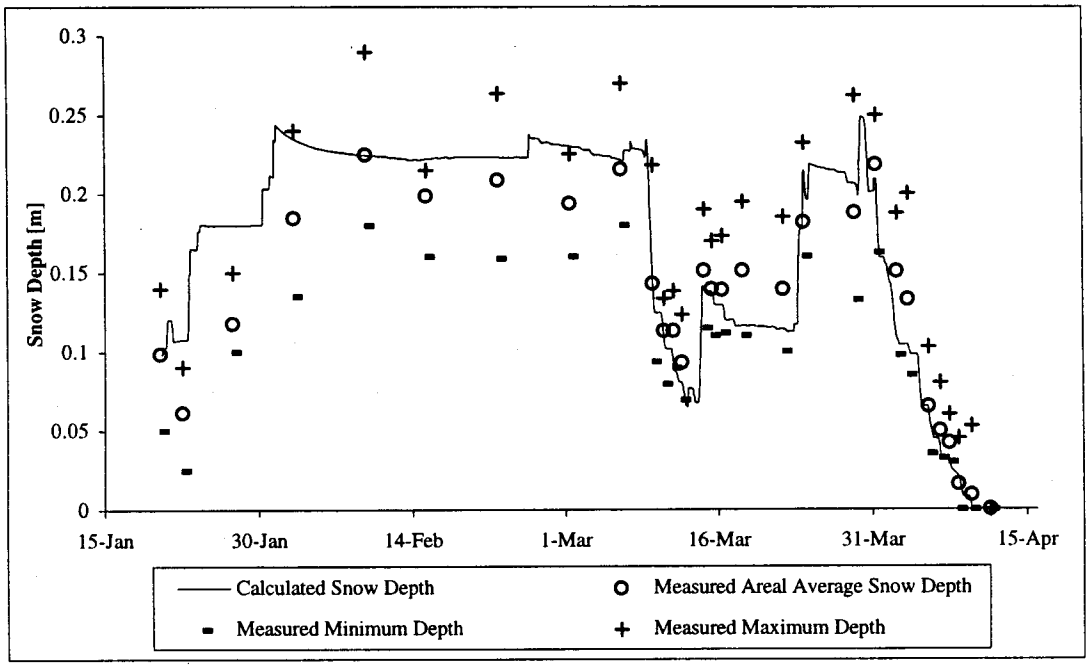

Figure 4.1. Calculated, measured areal average, and maximum and minimum values of measured snow depth.

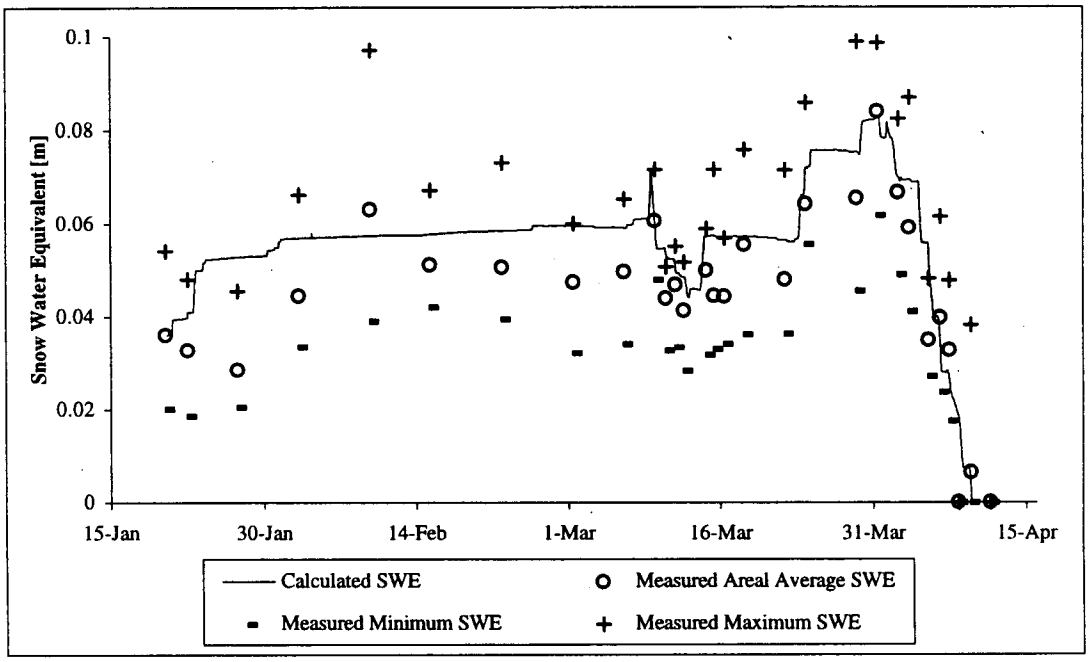

Figure 4.2. Calculated, measured areal average, and maximum and minimum values of snow water equivalent.

While the model replicated successfully the areal snow water equivalent near the meteorological station, it did not do as well at the temperature profile site which tended to have notably higher snow depth and water equivalent. The snow depth and water equivalent were simulated at the temperature site using three different starting points with the initial values determined as described above. Figures 4.3 and 4.4 show the results of the model runs which used different starting times: January 20, February 2, and March 14, respectively. The initial values for snow and soil properties are shown in Tables 4.3 to 4.5. The results indicate that the model is unable to predict the measured snow depth and water equivalent before February 2 and March 14. The model replicates reasonably well the measured snow depth and water equivalent at all other times, except in late March when the calculated snow water equivalent is slightly lower than the measured values.

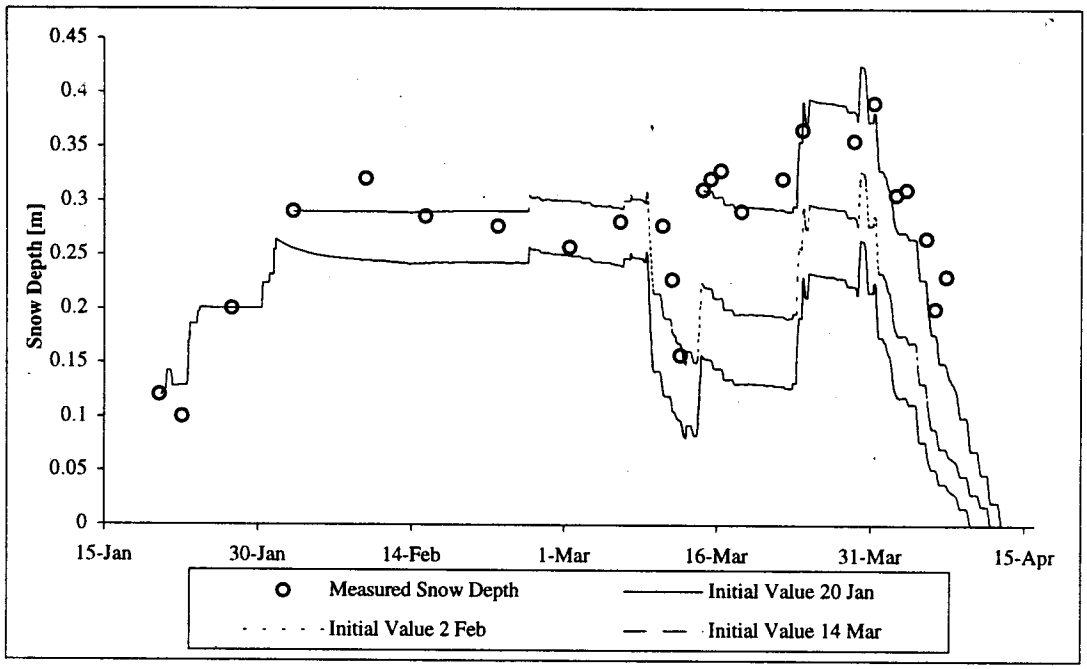

Figure 4.3. Calculated and measured snow depth at temperature profile site using different initial values for January 20, February 2, and March 14.

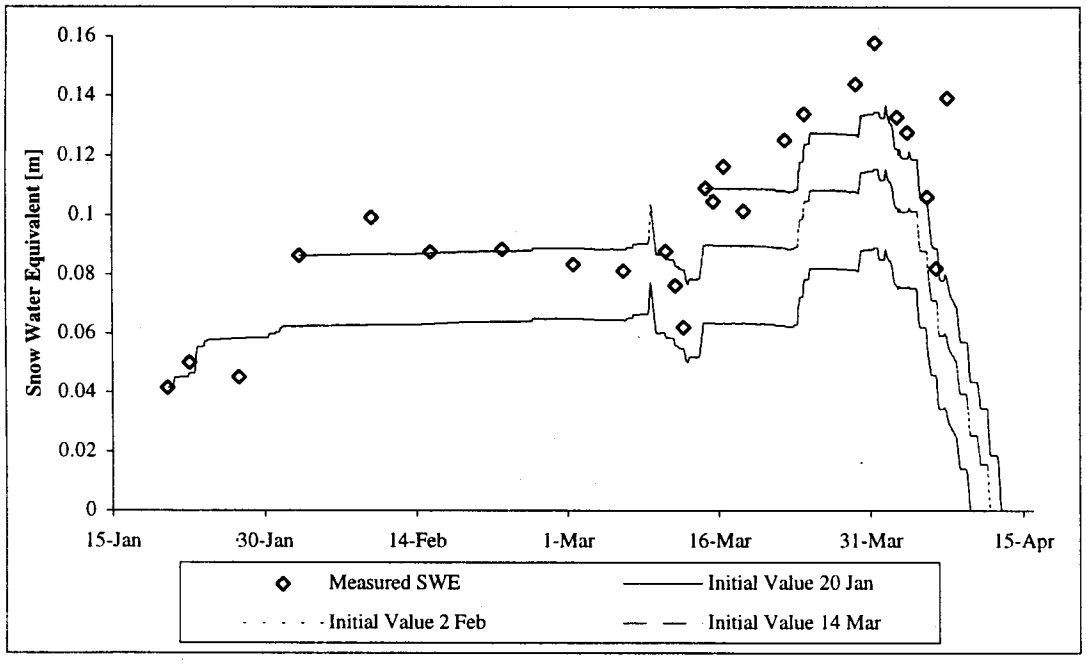

Figure 4.4. Calculated and measured snow water equivalent at temperature profile site using different initial values for January 20, February 2, and March 14.

Table 4.3. Initial values in snow and soil layers for the simulation of snow cover at the temperature profile site starting 10:00 a.m. January 20, 1994.

Node	Nodal temperature [K]	Elemental thickness [m]	Nodal water constituents bulk density [kg m^{-3}]	Nodal effective grain diameter [m]
1 (Clay)	274.4	0.3	400	0.000002
2 (Clay)	274.1	0.1	400	0.000002
3 (Clay)	274.0	0.1	400	0.000002
4 (Clay)	273.9	0.1	400	0.000002
5 (Clay)	273.4	0.1	400	0.000002
6 (Clay)	273.2	0.025	400	0.000002
7 (Clay)	273.1	0.05	400	0.000002
8 (Clay)	273.1	0.05	400	0.000002
9 (Clay)	273.1	0.05	400	0.000002
10 (Clay)	273.0	0.05	400	0.000002
11 (Clay)	272.9	0.05	400	0.000002
12 (Clay)	272.8	0.05	400	0.000002
13 (Clay)	272.6	0.05	400	0.000002
14 (Clay)	272.4	0.05	400	0.000002
15 (Clay)	271.7	0.025	400	0.000002
16 (Snow)	271.4	0.01	500	0.002
17 (Snow)	271.2	0.01	480	0.002
18 (Snow)	270.9	0.02	420	0.0015
19 (Snow)	270.6	0.02	370	0.0006
20 (Snow)	270.1	0.02	320	0.0005
21 (Snow)	269.6	0.02	260	0.0004
22 (Snow)	269.1	0.01	240	0.0003
23 (Snow)	268.6	0.01	200	0.0002

One plausible explanation for differences in modeled and measured quantities is that snow drift may have occurred at the temperature profile site, and drift was most extensive during the times when the model failed to replicate the measured snow depth. The snow which drifted was assumed to be blown from the top of the snowpack in the vicinity of the profile site. Extra precipitation was added to the measured values in an attempt to represent snow drift during early February and in the middle of March. The density of the added snow was taken as the average model calculated density of the top snowpack layer during the assumed drifting period. The additional snow mass was set equal to the amount necessary to raise the snow depth to the measured depth following the period of assumed drift. This resulted in an addition of 8.8 mm of precipitation (70 kg m^{-3} density) during February 1-8, and 25.2 mm (165 kg m^{-3} density) during March 13-14. The resulting snow depth and water equivalent are shown in Figure 4.5, which

indicates that snow depth corresponds well to the measured values, but snow water equivalent is underpredicted.

Table 4.4. Initial values in snow and soil layers for the simulation of snow cover at the temperature profile site starting 10:00 a.m. February 2, 1994.

Node	Nodal temperature [K]	Elemental thickness [m]	Nodal water constituents bulk density [kg m^{-3}]	Nodal effective grain diameter [m]
1 (Clay)	274.4	0.3	400	0.000002
2 (Clay)	274.2	0.1	400	0.000002
3 (Clay)	273.9	0.1	400	0.000002
4 (Clay)	273.7	0.1	400	0.000002
5 (Clay)	273.5	0.1	400	0.000002
6 (Clay)	273.3	0.025	400	0.000002
7 (Clay)	273.3	0.05	400	0.000002
8 (Clay)	273.1	0.05	400	0.000002
9 (Clay)	272.9	0.05	400	0.000002
10 (Clay)	272.9	0.05	400	0.000002
11 (Clay)	272.7	0.05	400	0.000002
12 (Clay)	272.3	0.05	400	0.000002
13 (Clay)	272.1	0.05	400	0.000002
14 (Clay)	271.8	0.05	400	0.000002
15 (Clay)	271.3	0.025	400	0.000002
16 (Snow)	271.0	0.01	500	0.002
17 (Snow)	270.9	0.01	500	0.002
18 (Snow)	270.7	0.01	410	0.0015
19 (Snow)	270.5	0.02	360	0.0006
20 (Snow)	269.6	0.04	330	0.00054
21 (Snow)	267.6	0.04	310	0.00046
22 (Snow)	263.8	0.05	280	0.00037
23 (Snow)	260.9	0.04	250	0.00027
24 (Snow)	257.7	0.04	230	0.00019
25 (Snow)	255.9	0.02	210	0.00013
26 (Snow)	255.2	0.01	200	0.0001

Table 4.5. Initial values in snow and soil layers for the simulation of snow cover at the temperature profile site starting 3:00 p.m. March 14, 1994.

Node	Nodal temperature [K]	Elemental thickness [m]	Nodal water constituents bulk density [kg m^{-3}]	Nodal effective grain diameter [m]
1 (Clay)	274.4	0.3	400	0.000002
2 (Clay)	273.6	0.1	400	0.000002
3 (Clay)	273.3	0.1	400	0.000002
4 (Clay)	273.1	0.1	400	0.000002
5 (Clay)	272.9	0.1	400	0.000002
6 (Clay)	272.8	0.025	400	0.000002
7 (Clay)	272.7	0.05	400	0.000002
8 (Clay)	272.7	0.05	400	0.000002
9 (Clay)	272.8	0.05	400	0.000002
10 (Clay)	272.6	0.05	400	0.000002
11 (Clay)	272.7	0.05	400	0.000002
12 (Clay)	272.9	0.05	400	0.000002
13 (Clay)	273.0	0.05	400	0.000002
14 (Clay)	273.0	0.05	400	0.000002
15 (Clay)	273.0	0.025	400	0.000002
16 (Snow)	273.0	0.01	500	0.002
17 (Snow)	273.0	0.01	500	0.002
18 (Snow)	273.0	0.01	500	0.0015
19 (Snow)	273.0	0.02	460	0.0006
20 (Snow)	273.0	0.03	430	0.00055
21 (Snow)	273.0	0.04	380	0.00048
22 (Snow)	273.1	0.05	350	0.00039
23 (Snow)	273.1	0.04	330	0.0003
24 (Snow)	273.1	0.04	290	0.00022
25 (Snow)	273.1	0.03	260	0.00015
26 (Snow)	273.1	0.02	230	0.0001
27 (Snow)	273.1	0.01	200	0.0001

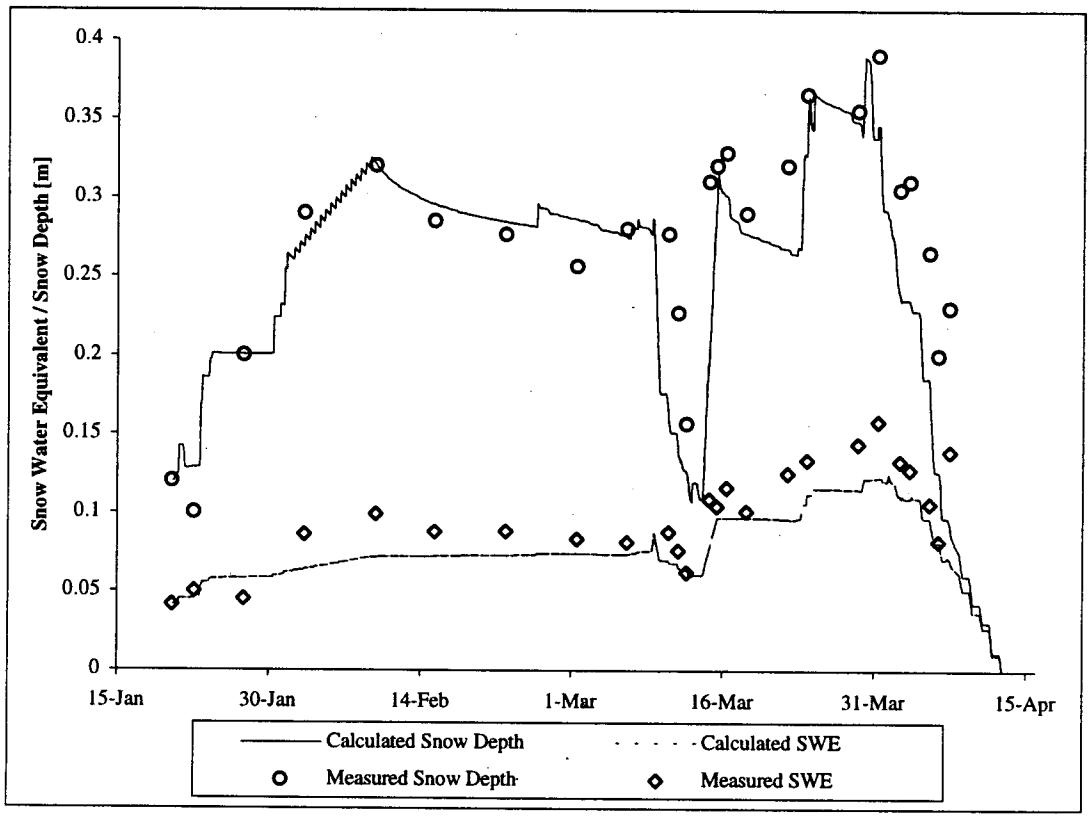

Figure 4.5. Calculated and measured snow depth and water equivalent at the temperature profile site assuming input from snow drift during February 1-8 and March 13-14.

4.1.2 Temperature Profiles

After the snow depth was modeled relatively well at the profile site, snow and soil temperatures were simulated. The initial temperature profile on January 20 (Table 4.3) was taken as the measured profile, except at the lowest point, where the measured temperature decreased slightly from about 1.7 to 0.7 °C during the winter. Since the model boundary condition at the bottom node has to be set at a constant temperature, 1.3 °C was assigned to the bottom node. Figure 4.6 presents the day and night time temperature profiles every two weeks, and Figures 4.7 and 4.8 show the snow and soil temperatures at the measured heights throughout the winter. In Figure 4.6 readings

were taken at noon of January 31 and midnight later the same day. This time is shown as February 1, midnight. Readings were taken just after midnight on March 15, and later that day at noon.

The temperature profiles indicate good agreement between the calculated and measured values, with the differences in the range of approximately ±1 °C (the mean difference between the measured and calculated snow temperatures at 0.05 m above soil surface was 0.67 °C). The soil moisture content affected the thermal conductivity considerably. A uniform initial soil bulk water density was assumed, but no measurements for the actual soil moisture were available. The highest differences between the calculated and measured data time series were found just below the soil surface, where the calculated temperature tended to change smoothly in time relative to the measured temperature.

4.1.3 Snow Density

The initial bulk water density profile was based on the measured initial total density of the snowpack and assumed high soil saturation. Figure 4.9 shows the calculated density profiles every two weeks, the corresponding interpolated average soft snow density, and assumed density of the crust layer immediately above the soil surface. Figure 4.9 shows that the model is able to simulate the formation of the dense lower layers of snow, since the bulk water density near the soil surface increases toward the melting period. The calculated bulk soil density of 1400 kg m^{-3} remained almost constant through the winter, because the model does not account for any liquid water movement through soil. The calculated soil density was low relative to values given elsewhere (e.g., Lee 1978), which were in the range from 1700 to 1900 kg m^{-3} for clay having moisture content between 10 and 30 %.

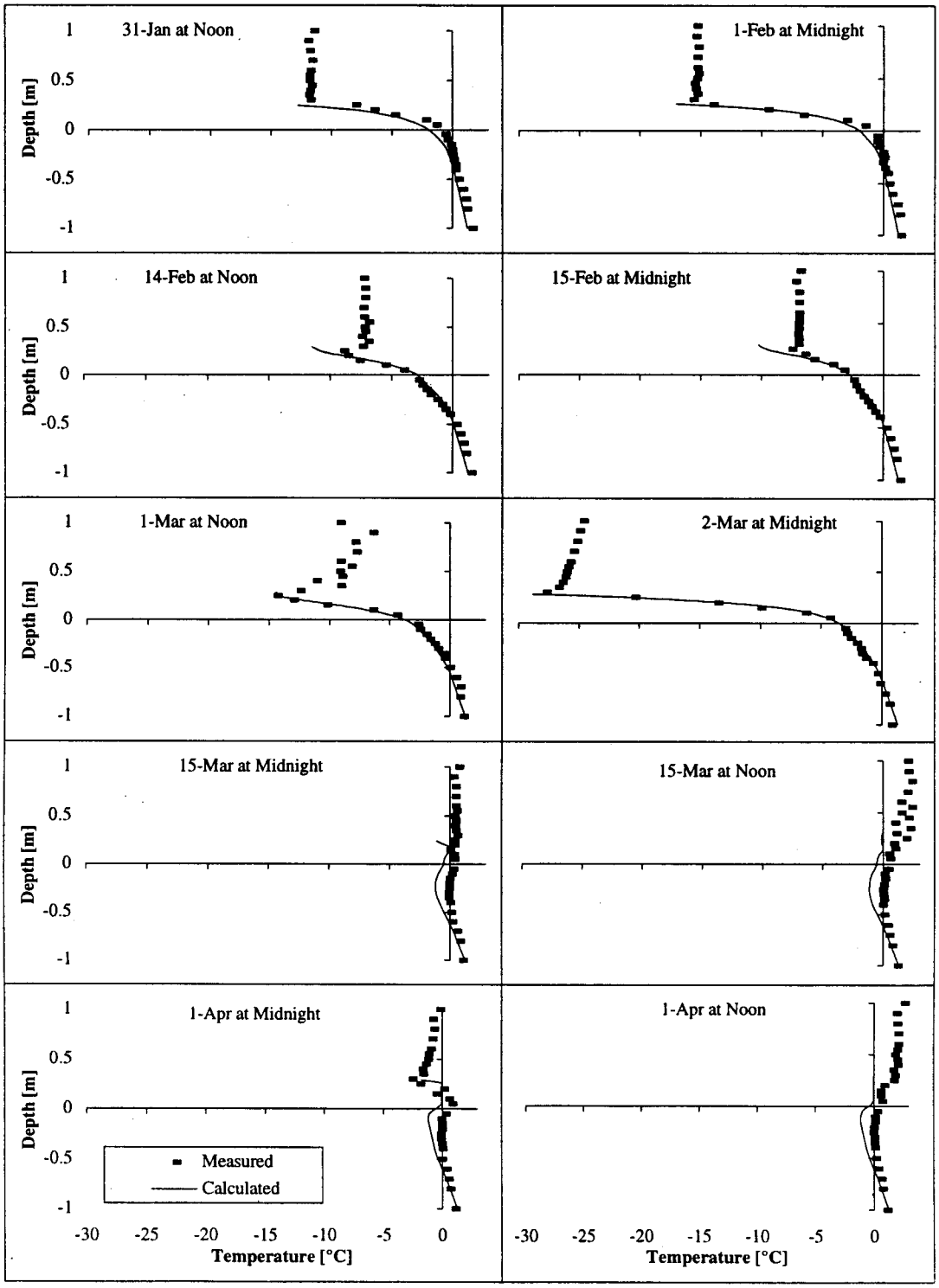

Figure 4.6. Two-week calculated and measured day and night time temperature profiles in snow and soil.

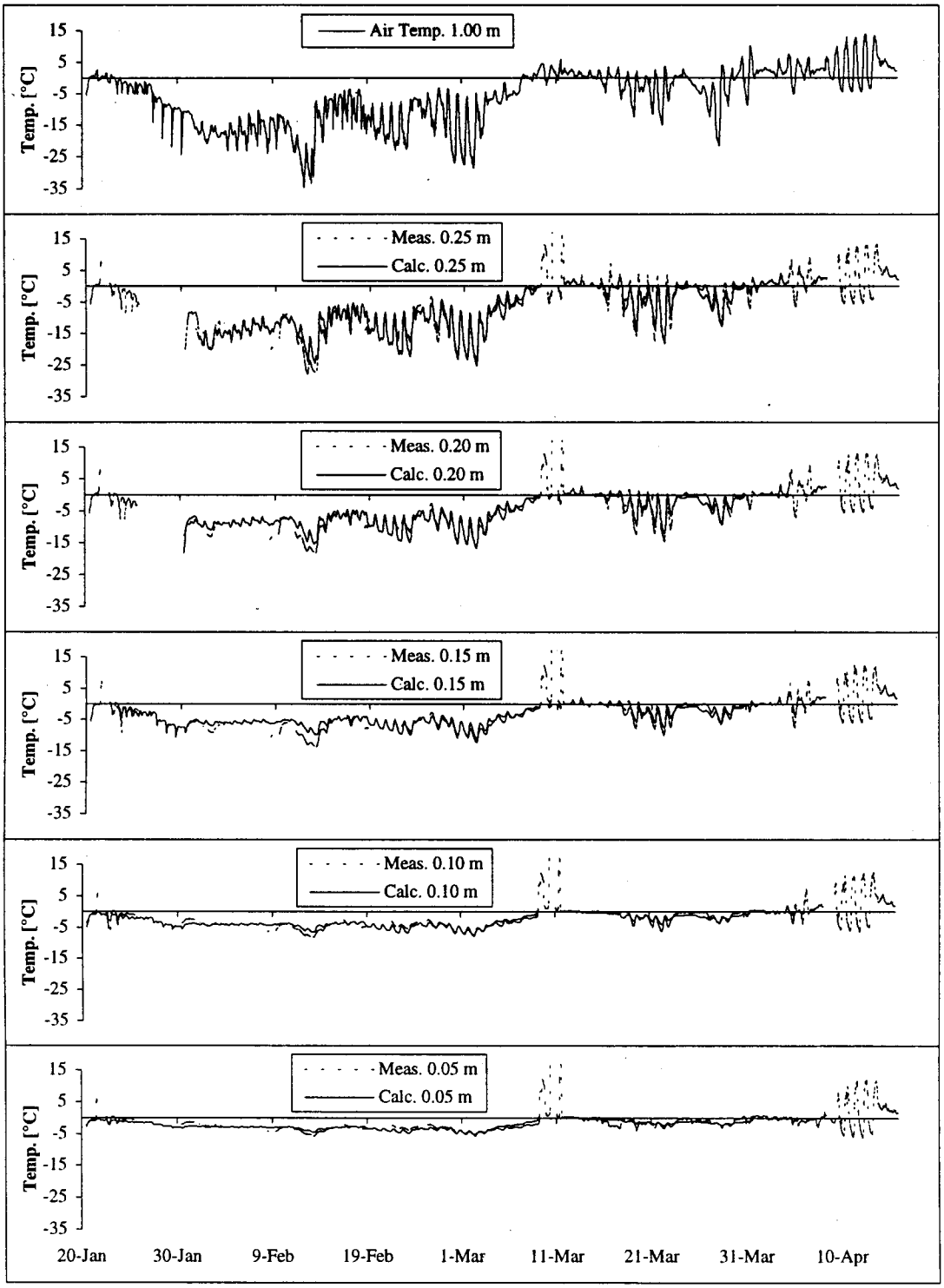

Figure 4.7. Calculated and measured snow temperature at particular depths during winter 1994.

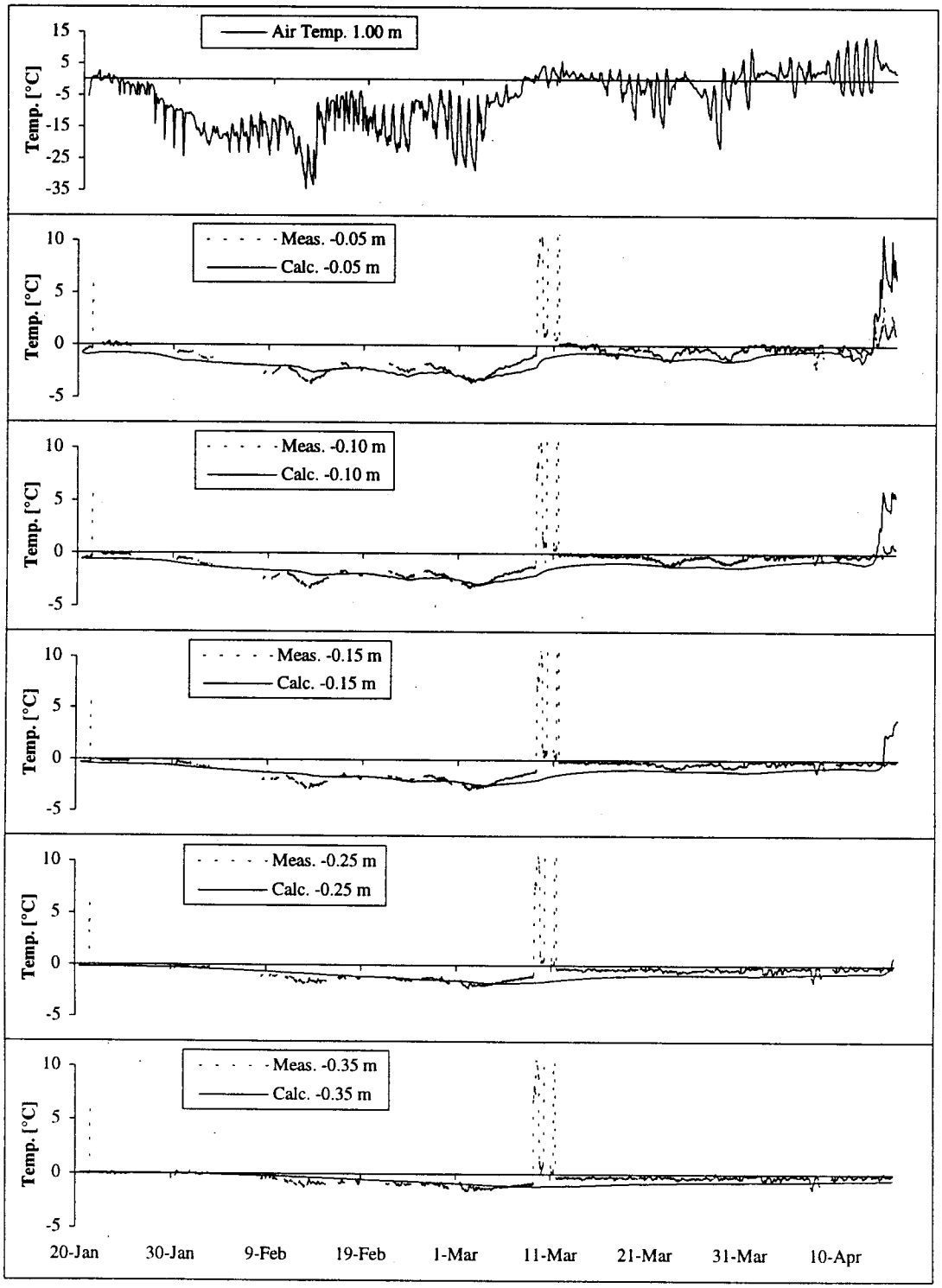

Figure 4.8. Calculated and measured soil temperature at particular depths during winter 1994.

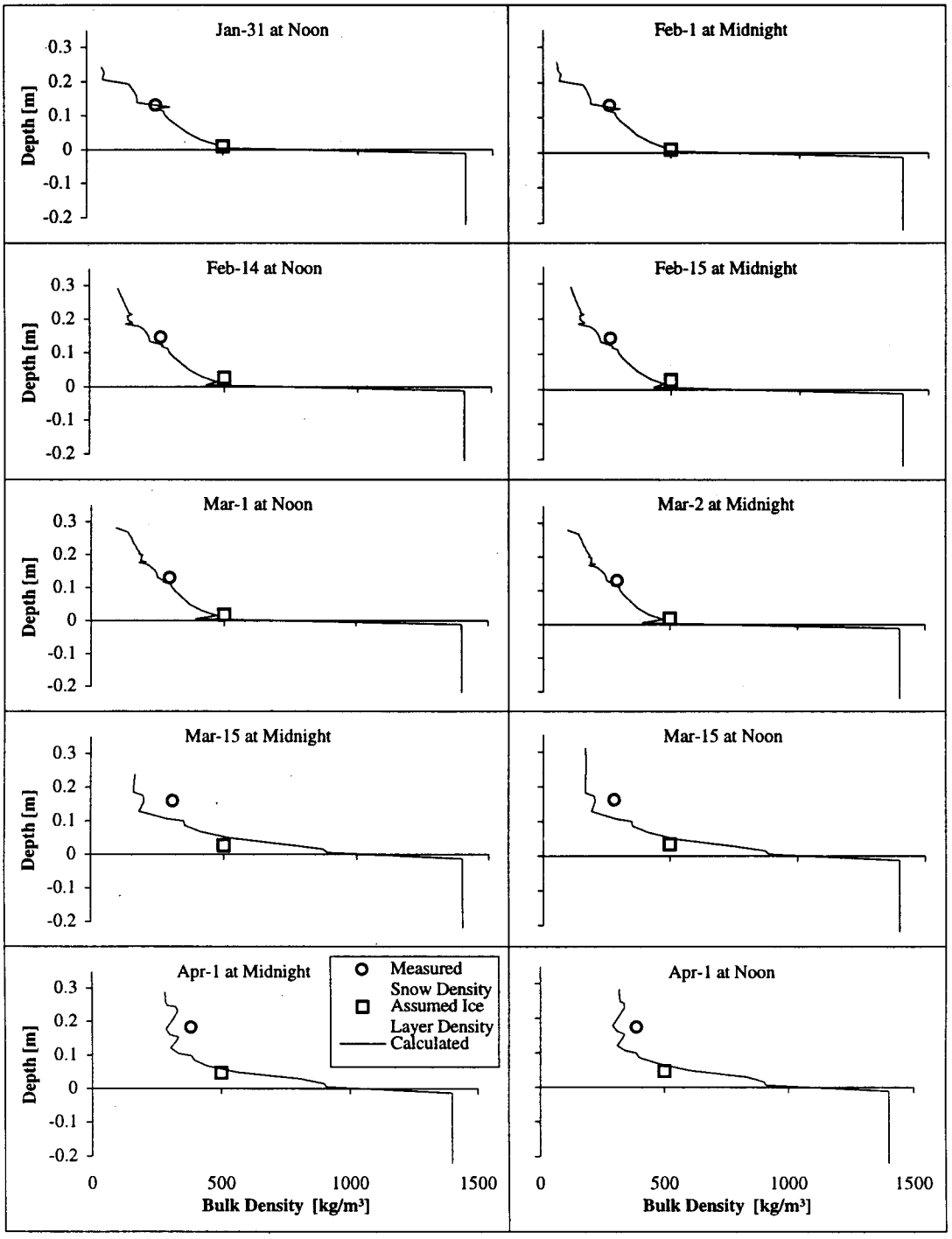

Figure 4.9. Two-week calculated day and night time snow and soil density profiles. Measured density was the measured bulk average for soft snow and the assumed 500 kg m^{-3} for the ice layer.

4.1.4 Thermal Conductivity

Effective thermal conductivity depends on the conductivity of the constituents, and the bulk density of the medium. Soil thermal conductivity is most sensitive to the degree of water saturation. The simulated temperature profile showed good agreement with the measured values, which supported the use of wet soil with a high bulk water density as an initial condition. Figure 4.10 shows the effective thermal conductivity profiles and typical ranges, which showed that the calculated values in snow and soil were plausible. The late winter high values at the bottom layers of snow indicated that water was re-frozen at the soil surface and the effective thermal conductivity increased towards the value corresponding to ice (2.5 W m^{-1} $°K^{-1}$), which is higher than the range reported for snow (Lee 1978).

4.1.5 Specific Heat

Figure 4.11 shows selected profiles of simulated specific heat together with typical ranges reported for snow and clayey soil. The simulated profiles show that the specific heat of wet snow rises toward the specific heat of water (4186.8 J kg^{-1} $°K^{-1}$) and the values for the soil were significantly higher than the literature values. Since the specific heat of soil increases with moisture content, the high values resulted from the assumed initial high soil saturation. Figures 4.6 to 4.8 indicate that the calculated soil temperatures change less rapidly than the measured values. The calculated values of effective specific heat imply that the heat required to raise the soil temperature is higher than the literature values. Therefore, the soil was relatively thermally inert to temperature changes, as demonstrated by the calculated temperature profiles.

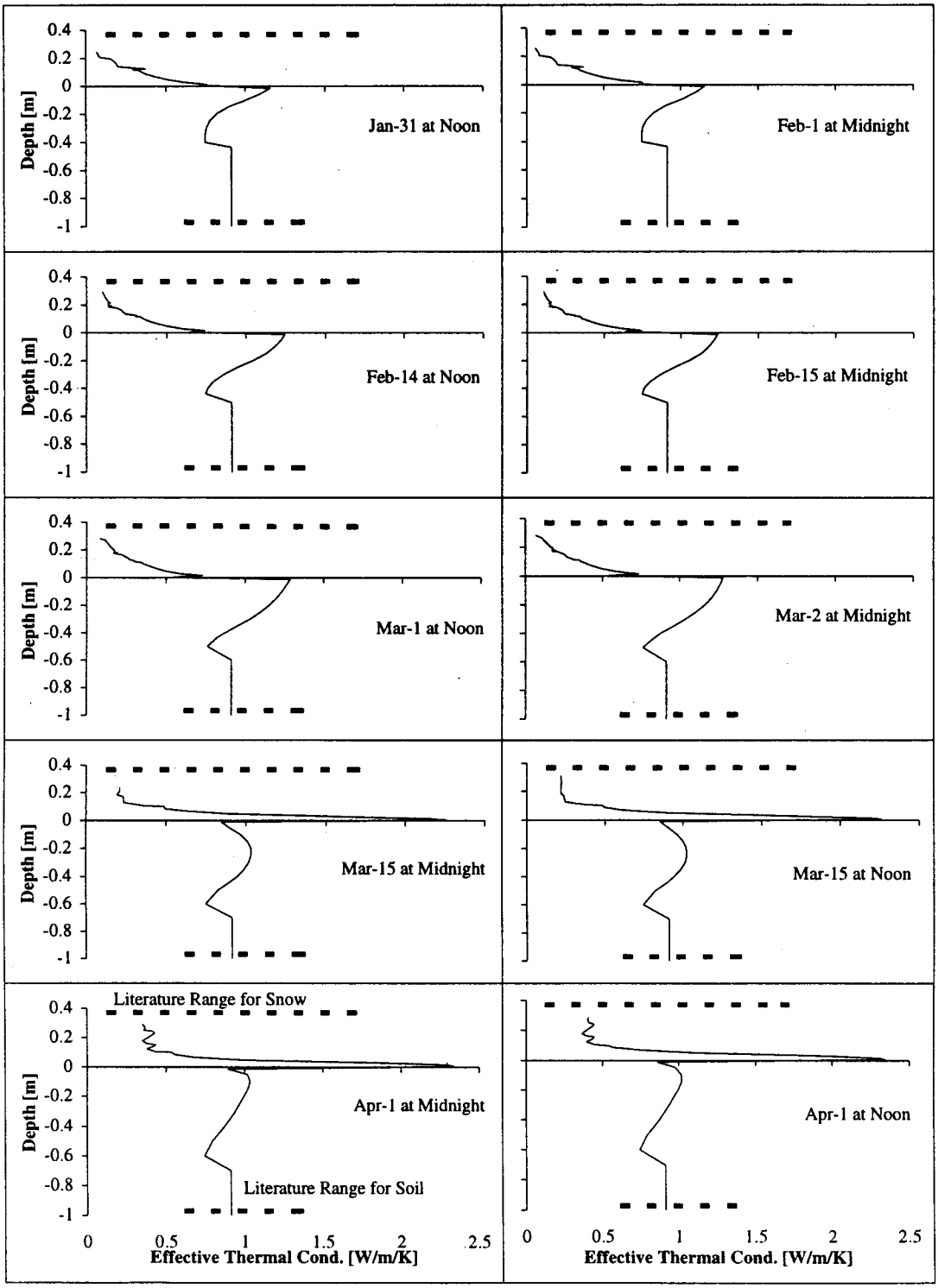

Figure 4.10. Two-week calculated day and night time effective thermal conductivity profile and typical conductivity ranges for snow and soil (Lee 1978).

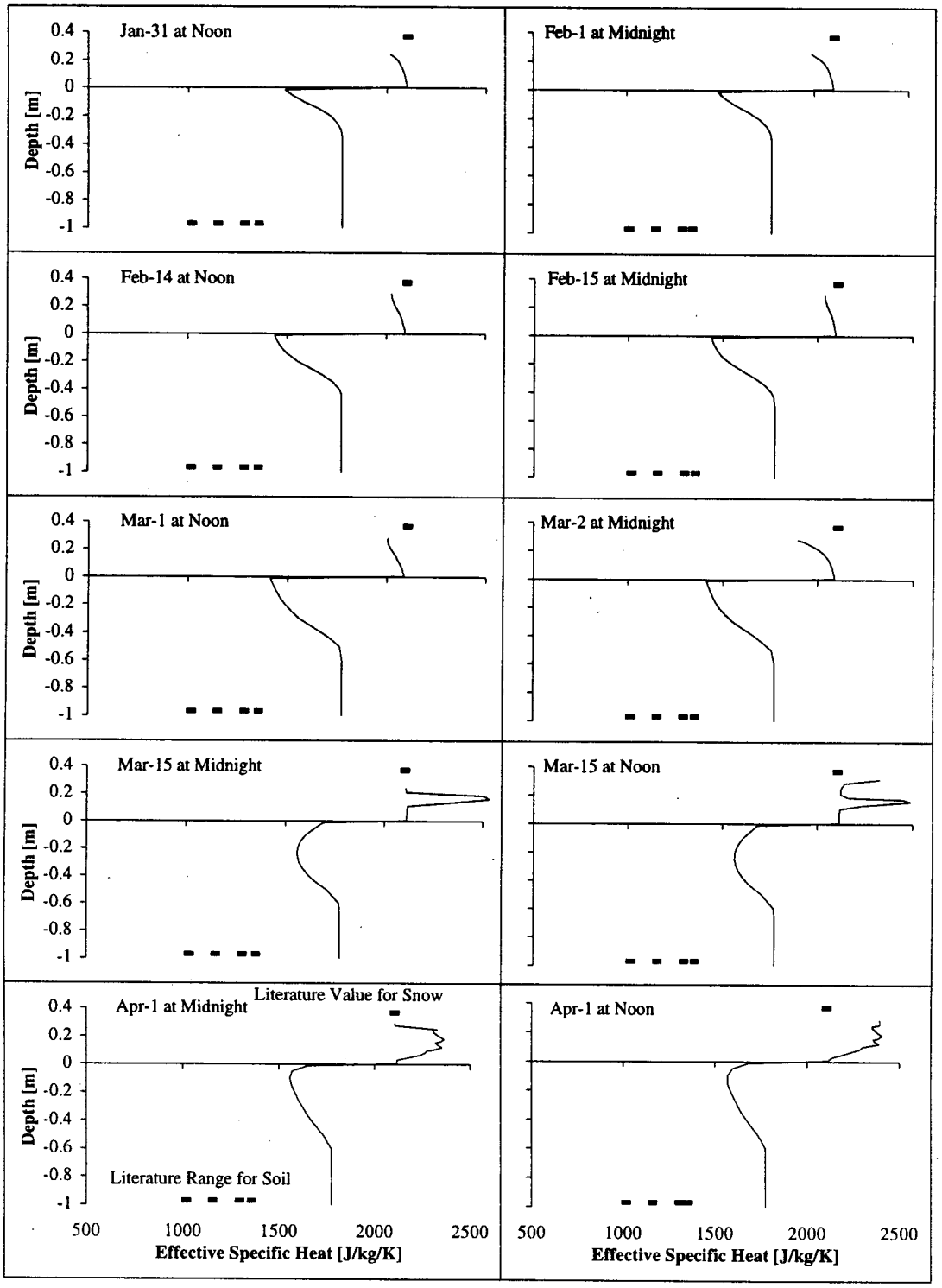

Figure 4.11. Two-week calculated day and night time effective specific heat profile and typical ranges for snow and soil (Lee 1978).

4.2 Model Sensitivity to Meteorological Variables

4.2.1 Energy Fluxes at Snowpack Boundaries

SNTHERM calculated the net fluxes of short- and long-wave radiation, sensible heat, latent heat, and advective heat at the surface, and ground heat at the bottom boundary of the snowpack. Figures 4.11 and 4.12 present the flux components at the snowpack boundaries, except the advective heat (precipitation input) which was negligible. Positive fluxes refer to energy input into the snowpack. Long-wave radiation and sensible heat comprise the major energy net fluxes during the cold winter, whereas short-wave radiation and sensible heat are the major influxes during the melting period starting in early April. The importance of the sensible heat energy is substantial during both the early melting period in March and the final snowmelt in April. The long-wave radiation flux remains negative throughout the winter indicating higher upward than downward radiation. Net latent heat fluxes are relatively small except for individual evaporation peaks during early snowmelt in March.

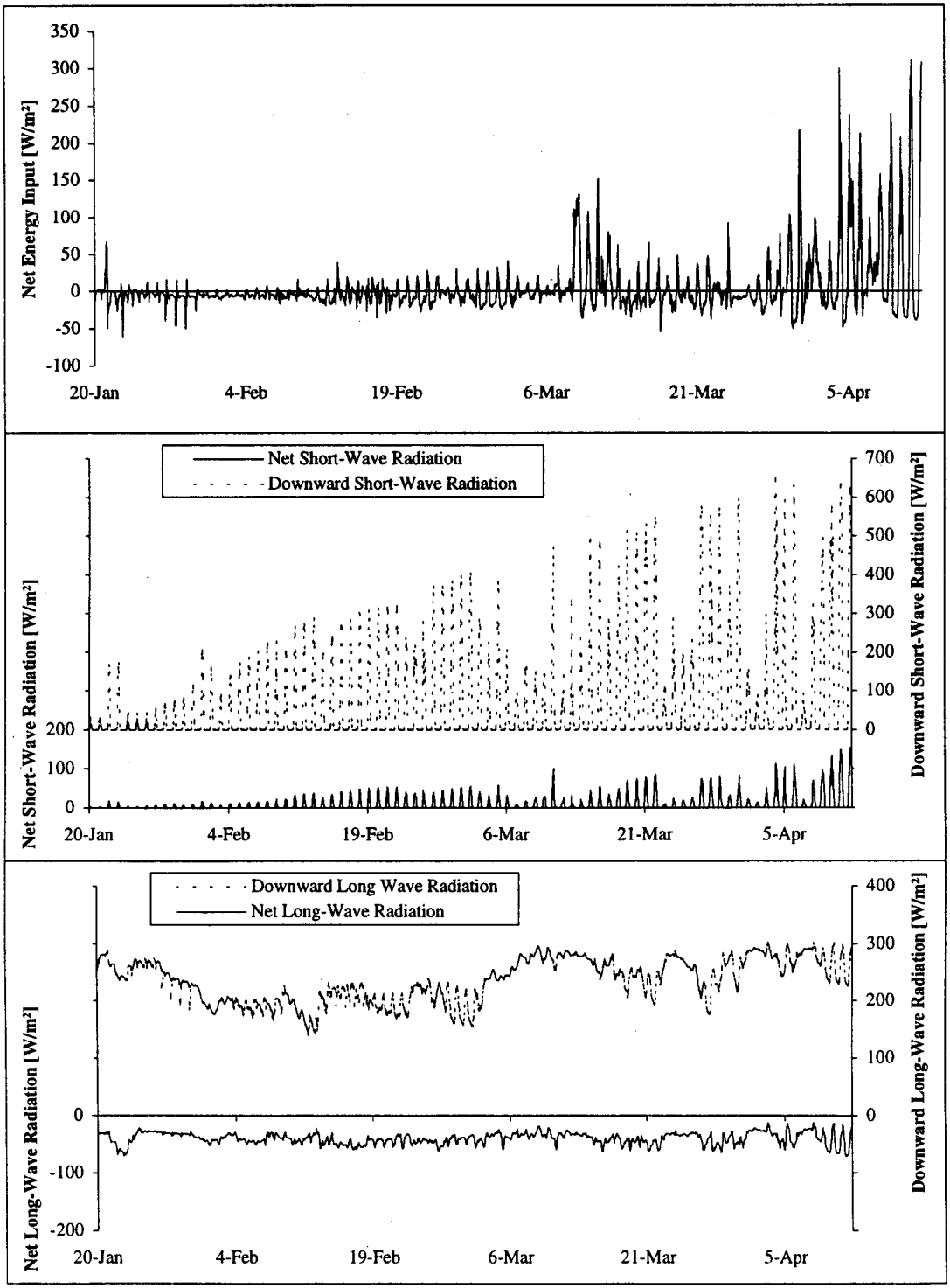

Figure 4.12. Calculated net input energy and short- and long-wave radiation fluxes at the snow pack surface boundary at temperature site (A).

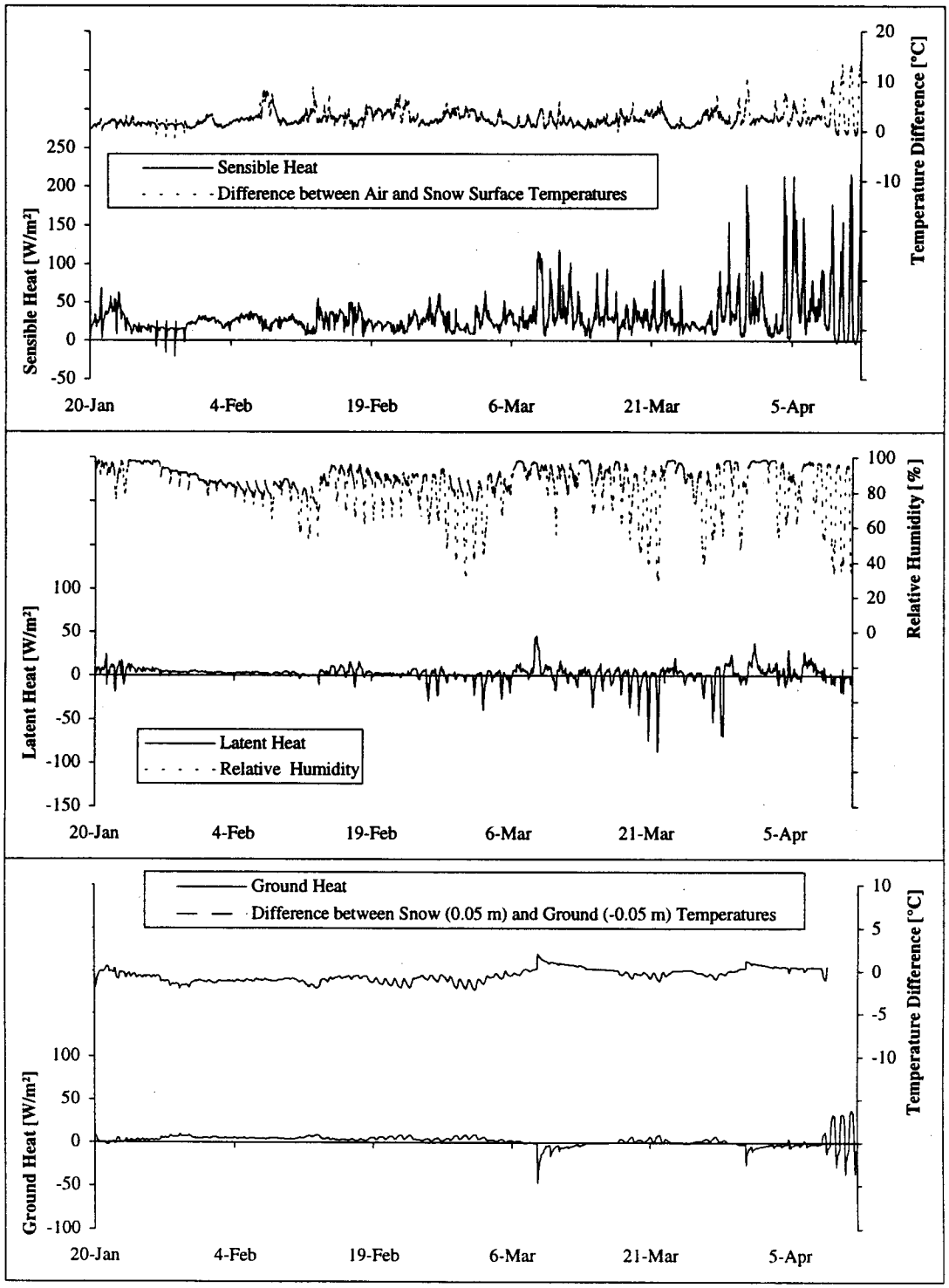

Figure 4.13. Sensible and latent heat fluxes at the snowpack surface, and ground heat flux at the snowpack bottom boundary at temperature site (A).

4.2.2 Sensitivity to Systematic and Random Errors

The sensitivity of the calculated snow depth was analyzed by perturbing the input meteorological variables. Systematic and random errors were studied separately for measured air temperature, short-wave radiation, relative humidity, wind speed, precipitation, and estimated long-wave radiation. The systematic error was assumed to be a constant deviation from a measured value, and was set for temperature as a fixed value and for the other meteorological variables as a percentage. Random errors were assumed to be independent and uniformly distributed between plus and minus the magnitude of the systematic error. The magnitude of the systematic error was set arbitrarily to a value that resulted in a notable change in the calculated snow depth. Random and systematic errors smaller than 5% in the meteorological variables other than air temperature did not affect the calculated snow depth. The error magnitudes explored are listed in Table 4.6.

Figures 4.14 to 4.19 present the calculated snow depth using the input meteorological variables (as described in Chapter 3) with one of them containing either a systematic or a random error. The snow mass was insensitive to random errors in the meteorological data since the average behavior of the calculated snow depth corresponds to the results obtained using the original "error-free" input variables. The snow depth shows the highest sensitivity to systematic errors in air temperature and long-wave radiation. Assumed errors in short-wave radiation had negligible effect on the snow depth. Errors in relative humidity, wind speed, and precipitation (including snow drift) had a moderate influence on the snow mass.

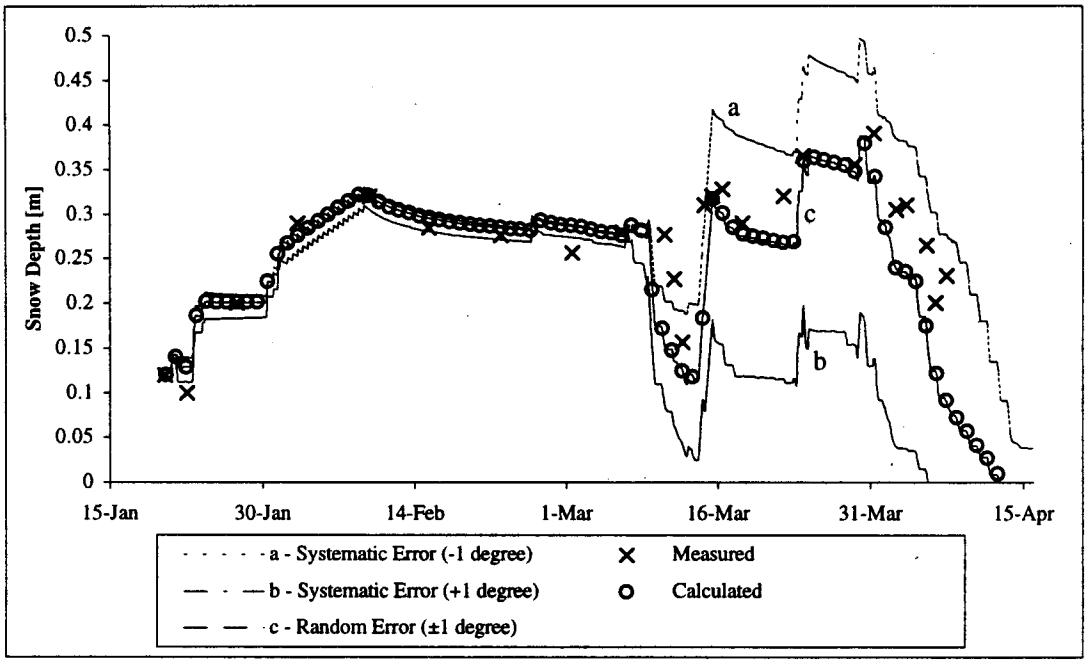

Figure 4.14. Sensitivity of calculated snow depth to air temperature errors.

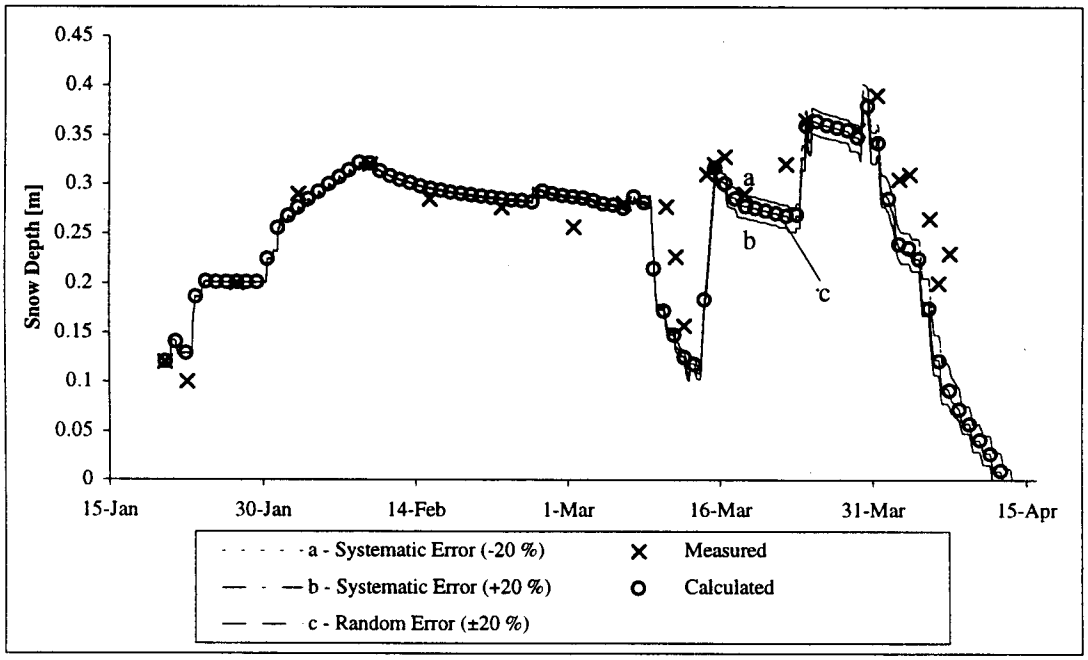

Figure 4.15. Sensitivity of calculated snow depth to short-wave radiation errors.

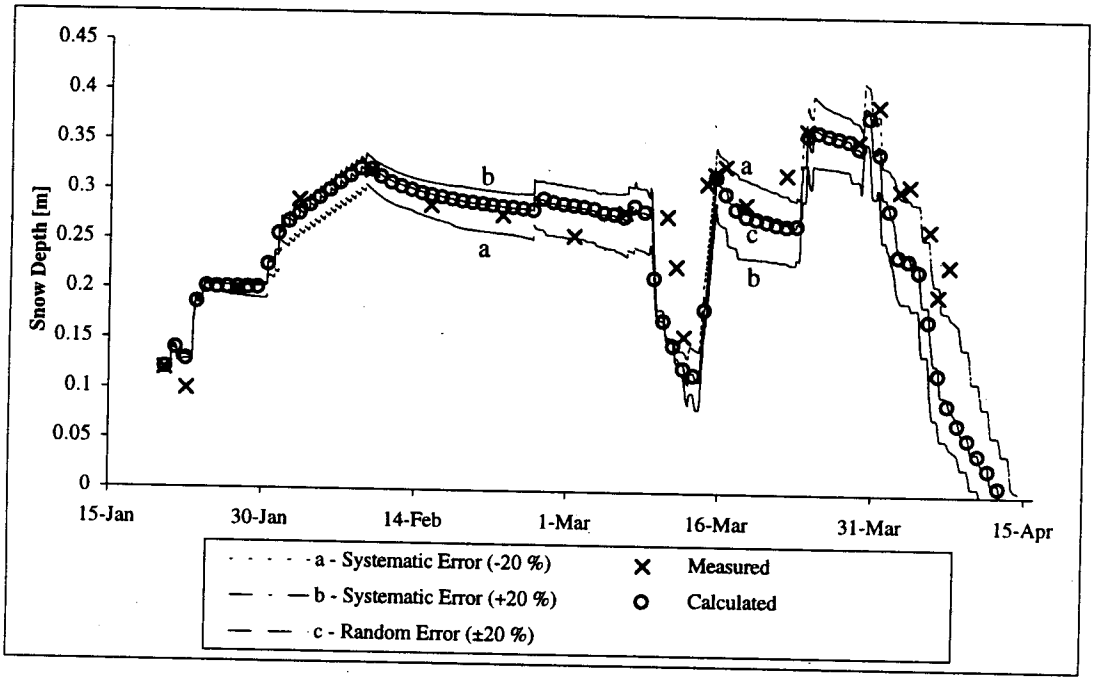

Figure 4.16. Sensitivity of calculated snow depth to relative humidity errors.

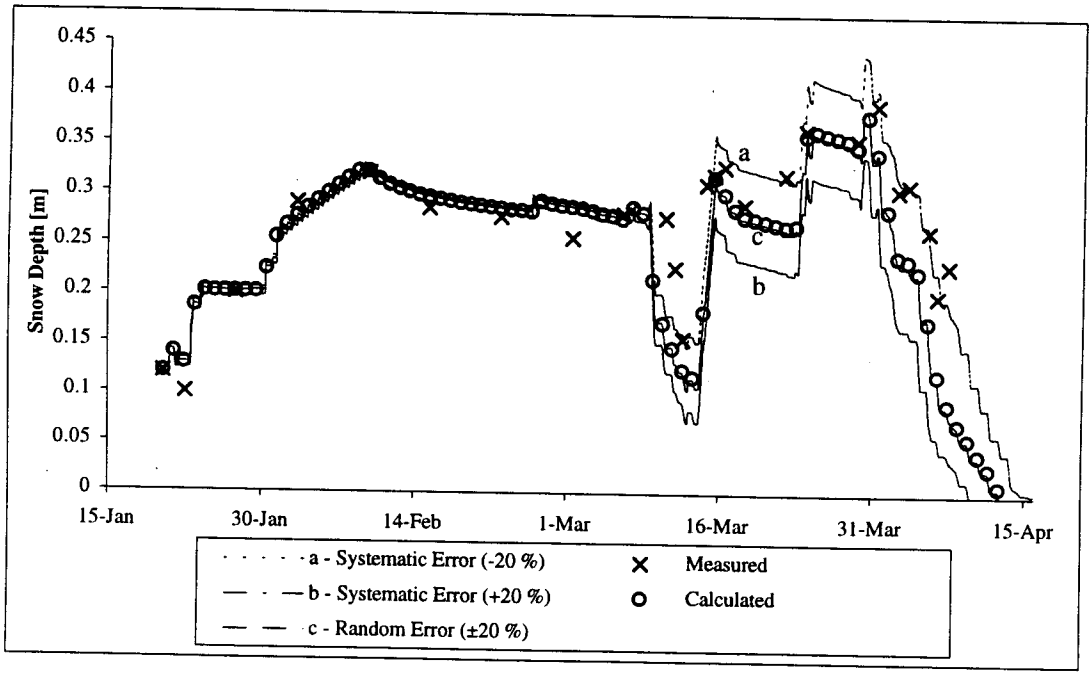

Figure 4.17. Sensitivity of calculated snow depth to wind speed errors.

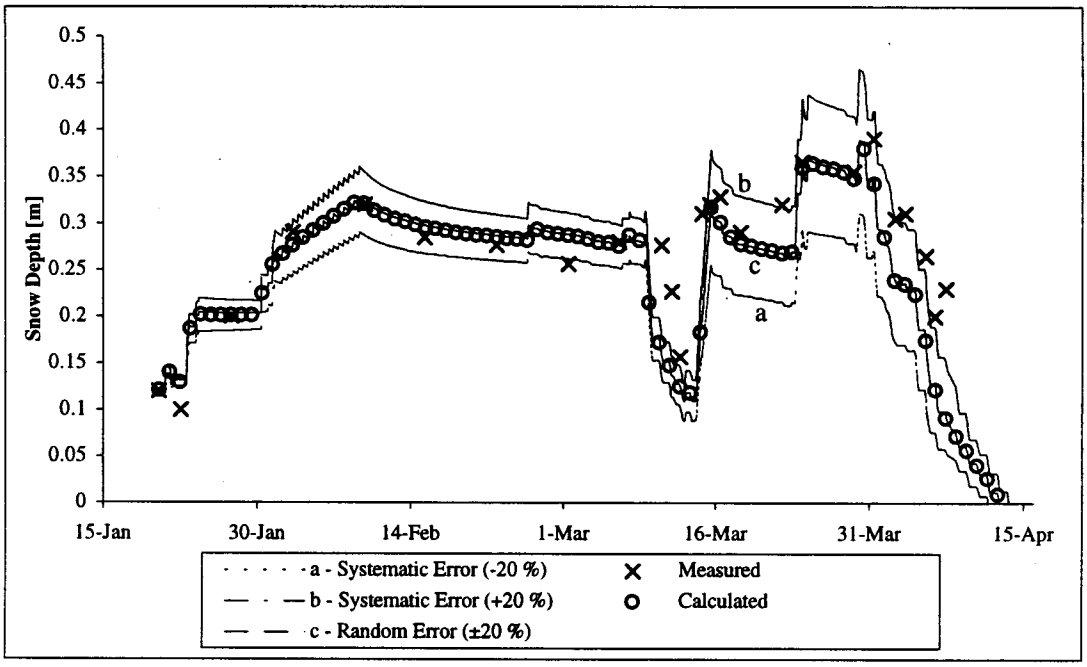

Figure 4.18. Sensitivity of calculated snow depth to precipitation errors.

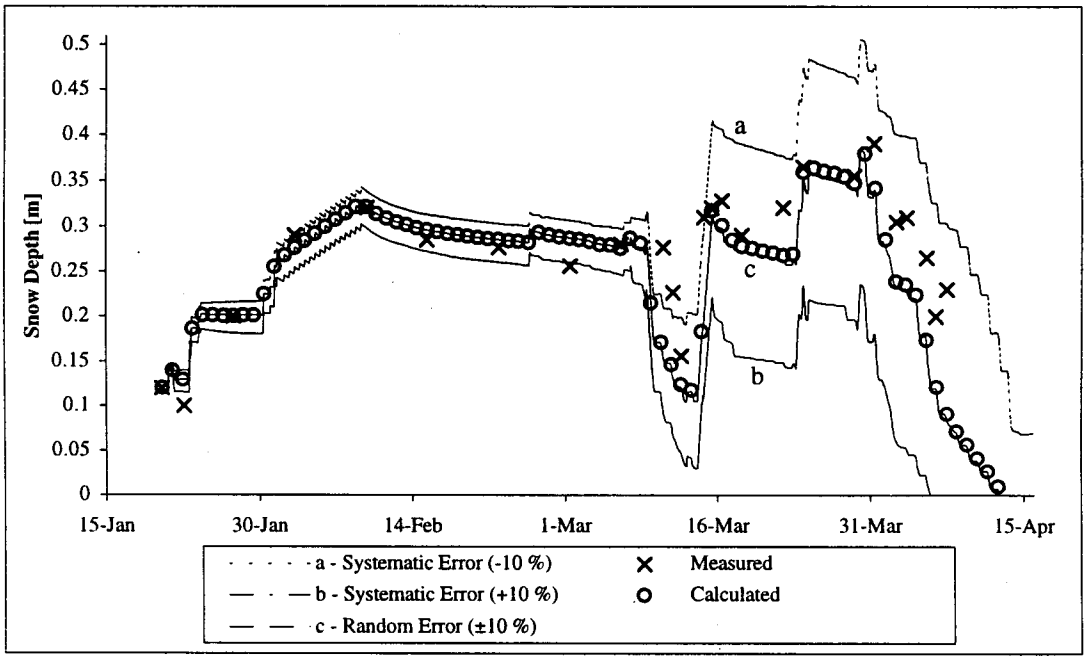

Figure 4.19. Sensitivity of calculated snow depth to long-wave radiation errors.

Table 4.6. Magnitudes of systematic and random errors used to assess the snow depth sensitivity to different variables.

Variable	Systematic error (high)	Systematic error (low)	Random error
Air temperature	+1 °K (0.35 .. 0.42 %)	-1 °K (-0.35 .. -0.42 %)	±1 °K (-0.40 .. 0.39 %)
Short-wave radiat.	+20 % (0 .. 150 W m^{-2})	-20 % (0 .. -150 W m^{-2})	±20 % (-120 .. 125 W m^{-2})
Relative humidity	+20 % (1.4 .. 17 unit %)	-20 % (-6.0 .. -20 unit %)	±20 % (-20 .. 17 unit %)
Wind speed	+20 % (0 .. 1.7 m/s)	-20 % (0 .. -1.7 m/s)	±20 % (-1.3 .. 1.2 m/s)
Precipitation	+20 % (0 .. 1.1 mm/h)	-20 % (0 .. -1.1 mm/h)	±20 % (-0.41 .. 0.49 mm/h)
Long-wave radiat.	+10 % (14 .. 31 W m^{-2})	-10 % (-14 .. -31 W m^{-2})	±10 % (-28 .. 29 W m^{-2})

4.3 Discussion of Model Results

4.3.1 Model Parameters and Initial Values

The model parameters can be adjusted to calibrate SNTHERM for local conditions. Jordan (1991) suggested that parameters be calibrated separately for the cold winter and melting periods. The available data at Sjökulla were insufficient to support formal model calibration. A number of missing meteorological data were estimated, but the filled-in values were more or less arbitrary. The meteorological variables were measured at site B, which was located 220 m from the temperature profile site (A in Figure 3.1) and had different local characteristics such as aspect and snow properties. The available snow cover measurements included high variability as shown in Figures 3.6 and 3.7. In addition, the calculated snow water equivalent was uncertain because of the unknown ground and ice layer properties. Because of these shortcomings in the data, the cold winter parameter values suggested for use with SNTHERM were employed.

The initial snow and soil properties were based on the observations at the site and typical values found in the literature. The only known initial condition was the measured temperature profile (A) in the snow and soil. However, the assumed initial temperatures were actually not valid at the meteorological site (B) where the snow depth was lower than at the temperature profile site (A). The initial snow density corresponded to the

measured value, but the density gradient with depth was assumed. The initial soil bulk water density was adjusted to make the calculated and measured temperature profiles compatible. Therefore, the only model calibration was effected by changing the bulk soil water density. Grain diameters for snow and soil were taken as typical values reported in literature. The nodal layer thickness in the soil was chosen to correspond to the location of the temperature sensors at the profile site. The initial thickness of snow layers was chosen to be relatively small, however, the model changed the layer thicknesses and the number of layers with time and the influence of the initial conditions became relatively unimportant.

4.3.2 Mass Balance

The objective of the mass balance calculations at the temperature profile site was to replicate the measured snow depth. Since dry snow is an effective insulator, significant errors in simulated snow depth would have prevented useful comparison being made between measured and calculated snow and soil temperature profiles. After the snow depth was simulated reasonably well, the model was calibrated by changing the initial soil parameters in attempt to replicate the measured temperature profiles. The assumed initial soil properties affected the thermal balance most and the mass balance only slightly.

The calculated snow depth and water equivalent showed that the model performed well using the suggested parameter values and the given initial condition (Figures 4.1 and 4.2). While the model simulated the measured snow melt well over a range of snow depth changes, the simulated snow accumulation was slightly less satisfactory. During the 5-day period of missing data at the end of January, the model overpredicted the snow mass but fitted the measured areal values well during other times. However, the model results at the end of January were sensitive to the initial value: an initial condition with a lower snow mass gave a better agreement. The comparison between the areal

average and temperature profile site snow depths suggested extensive drifting occurred at the profile site (Figure 3.31). After additional snow was added to match the measured depth, the calculated snow water equivalent still remained low (Figure 4.5). This indicated that the snow, which was assumed to drift to the site, most likely experienced fast metamorphism during drifting (McKay and Gray 1981, p. 155).

The simulated density gradient in snow was steep with a low top layer density. Densification was most rapid just after a snowfall event. The water movement through the snow was treated one-dimensionally and no lateral flows were assumed. The modeled liquid water percolated downward in the snowpack and was artificially drained at the snow-soil interface. While ponding of water at the frozen ground was not represented in the model, the densification and high liquid water content at the bottom snow layer was simulated reasonably well. When the wet snow immediately above the soil surface froze, a distinct ice layer was formed. The actual ice layer above the soil surface was thicker than the modeled layer, which suggests that water was ponded and re-frozen on the impermeable frozen ground.

4.3.3 Thermal Balance

Despite the uncertainties in the input data resulting from data fill-in, the model simulated the snow and soil temperatures quite well (Figures 4.6 to 4.8). Therefore, the modeled temperatures supported the validity of the temperature measurements even near the snow surface. The highest differences between the calculated and measured values corresponded to the time periods between breaks in the meteorological time series. During the melting period, percolating water was observed to flow along temperature sensors and the wooden stick that held the measurement system. The highest temperature sensors were exposed to air and the lowest sensors in the snow were probably partly surrounded with air as well. This was not a significant problem, however, because the temperature profile remained relatively isothermal during

snowmelt. The measured soil temperatures fluctuated more than the calculated values. The smooth variation in simulated temperatures was partly due to the assumed constant temperature at the bottom boundary and the seemingly high calculated effective heat capacity of the soil. The soil temperature 1.0 m below the surface was actually changing slightly with major changes in air temperature. The effective thermal conductivity in snow and soil compared well to the literature values (Figure 4.10). However, the specific heat in the soil was higher than the literature values (Figure 4.11). This most likely resulted from the assumed initial high soil water content.

4.3.4 Sensitivity Analysis

The assumed errors in the meteorological variables represented a range from strictly systematic to completely random fluctuation from the measured or estimated values. The calculated snow depth was insensitive to any of the assumed random errors. The systematic errors had a major effect on the snow depth, which was most sensitive to constant errors in air temperature and long-wave radiation (Figures 4.14 and 4.19). The systematic errors in the other measured variables had a minor influence on the calculated snow depth. Systematic error in short-wave radiation (Figure 4.15) did not show any significant influence on the overall snow depth, because the net solar energy flux was small during the cold part of the winter and high only during the snowmelt, when the melt was mainly driven by the sensible heat flux (Figure 4.13). Systematic error in wind speed affected the sensible heat flux resulting in a slight change in the snow depth (Figure 4.17). Systematic decrease in the relative humidity increased the net latent heat flux, which, however, did not influence significantly the calculated snow depth (Figure 4.16). A constant error in precipitation mass (and snow drift) affected only slightly the calculated snow depth (Figure 4.18).

Chapter 5 Discussion

A detailed mass and energy balance model (SNTHERM, Jordan 1991) was used to simulate snow cover properties during the winter of 1994 at Sjökulla, Finland. The model was assumed to be a correct physical representation of the major processes in the snowpack. An extensive input data quality check was made prior to using the site data with the model. The data quality and assurance check indicated that the measured variables were likely to be correct after taking into account instrument calibration information obtained during the summer of 1995. After interpolating and filling-in missing data, the data quality proved satisfactory on average. However, short term dynamics in the variables were lost during measurement breaks of several days duration. The snow cover model was used successfully to check further the overall quality of the filled data. The agreement between calculated and measured areal snow depth and water equivalent indicated that the measured and estimated energy inputs were likely to be correct, and that the estimated long-wave radiation was realistic. The measurement breaks and the uncertainties in the interpolated data did not preclude calculation of continuous snow cover through the winter. The model results were relatively insensitive to the uncertain substituted values.

SNTHERM simulated the measured areal snow depth and snow water equivalent satisfactorily. The model did not take into account lateral movement of snow such as drifting, since it simulated the point depth and water equivalent of an assumed undisturbed snowpack. In the case of snow depth and water equivalent calculated lower than measured values, the inference was that additional processes affected the snow cover. In the case of snow drift, the modeled mass lost or gained should be included in addition to measured precipitation. Therefore, the measured snow water equivalent should be used to assess mass changes caused by snow drifting. In the case of forest canopy over the snowpack, meteorological variables should be measured ideally under the canopy to get the energy and mass input correct. Where possible, additional

observations about the amount of snow held in trees, which may fall onto the snowpack, should be gathered.

Temperature index and simple energy balance models are capable of replicating the measured total water equivalent (U.S. Army Corps of engineers 1956, Male and Gray 1981, Kustas et al. 1994). However, empirical index models require calibration against measured snow mass. For the application reported here, SNTHERM was capable of replicating areal snow depth and water equivalent without calibration of model parameters. The model output provided information about characteristics of the site. It is likely that snow drifted at the profile site. The measured temperature profile was useful for assessing the soil moisture content, which affected considerably the thermal properties of soil. Another advantage of using the multilayered-physically-based snow model was the resulting simulated profiles of snow density, effective thermal conductivity, and specific heat. The snow density profile simulated correctly the formation of a dense layer at the soil surface. Moreover, the effective thermal conductivity suggested that wet bottom layers of the snowpack actually re-froze and formed a distinct ice layer as was observed at the site.

Since SNTHERM provided detailed information about site characteristics, its use would have influenced the experimental design during the time the data were gathered. The snow cover measurements and the model results indicated that selection of the location of the temperature profile measurement site was inappropriate. It would have been more consistent to measure the snow and soil temperature at the meteorological site, where the data would have been comparable (collected at the same site), and lateral snow drifting was inconsequential. Also, the model would have suggested additional variables which needed to be measured. In this case, the additional measurements would have involved long-wave radiation or cloudiness and the initial soil moisture profile. Snow depth and water equivalent showed considerable variation in field sections which were smaller than one hectare. The variation was due to the plowed rugged surface and

snow depth differences along the hillslope. The point model did not provide any explicit solution to the problem of representing spatial snow cover heterogeneity. However, the model represented successfully the behavior of snowpack affected only by vertical mass fluxes. Application to spatially distributed snow cover should take into account snow drifting and the lateral movement of water in snow, which would require additional spatial measurements (Colbeck 1974).

Examination of measured and estimated energy fluxes at the snowpack boundaries indicated that the sensible heat was the dominant flux during most of the winter. The largest peak values of latent heat were of opposite sign to the corresponding sensible heat; the overall importance of latent heat was small. The net long-wave radiation was negative, i.e., the energy was lost from the snowpack. The net short-wave radiation was small during the cold winter; high values occurred only in late spring. Ground and advective heat fluxes were of minor importance.

The snow depth sensitivity to prescribed systematic and random errors in the meteorological variables indicated that air temperature had the most notable effects on the calculated snow depth. The other important variable was the incoming long-wave radiation, which was a function of air temperature to the fourth power. The prescribed errors in short-wave radiation did not have any significant effect on the snow depth, because the high albedo calculated by the model lowered net solar radiation flux; the melt was mainly driven by sensible heat flux.

Chapter 6 Conclusions

The suitability of a point mass and energy balance model (SNTHERM) for simulating snow cover properties for a winter season in Southern Finland was assessed. To permit physical interpretation of the model results, an extensive data quality assurance/control check was performed to determine the quality of the measured meteorological series. The data, after careful processing, were shown to be satisfactory, even if the small time scale dynamics were not represented well during periods where filled-in data were used.

The physical multilayered snow model was useful for both checking the data and simulating the snow characteristics. The value of using a snow model during field investigations to check the validity of the measurements, to identify additional variables to be measured, and to select representative snow cover measurement points has been demonstrated. The model simulated reasonably well the average areal snow depth and water equivalent, which were highly variable. At a temperature profile measurement site, apparent (unobserved) snow drift needed to be accommodated by adding extra snow input to the measured precipitation. The model results indicated good agreement between the measured and calculated temperature profiles. There were less fluctuation in the modeled soil temperature than in the measured values. This resulted from setting the bottom node boundary to a constant temperature and using the high effective soil specific heat computed by the model. The measured temperature profiles were useful for estimating an average initial soil moisture, which had a major influence on the modeled thermal properties of soil. Finally, the model simulated the formation of a distinct ice layer at the bottom snow layers, which was consistent with observations. Since the mass and energy balance were in accordance with the field measurements, the estimated long-wave radiation appears to be approximately correct.

The benefits of the physical snow model include the lack of calibration needed to apply it, and the vertical profiles of snow cover properties it calculated. The model explained

the small-scale site characteristics and indicated the time of snow mass changes that likely were due to external sources such as snow drift. To model the spatial distribution of snow, snow drifting and lateral water movement in snow need to be taken into account. Also, the meteorological data have to be measured in both open areas and under forest canopy.

The relative energy fluxes on the snow pack boundaries indicated that the sensible heat flux was the most important component throughout the winter. Net radiation fluxes were of secondary importance. The sensitivity analysis using assumed errors in the meteorological data showed that random errors were insignificant in simulating snow depth. Systematic errors in air temperature and long-wave radiation had the largest effects on modeled snow depth. Other input variables, including short-wave radiation, did not have any considerable effect on the snow depth.

Chapter 7 Suggestions for Future Research

Further study could follow two paths. First, the model application could be extended, and second, SNTHERM results could be compared to alternative modeling approaches. The present study could lead to an analysis of uncertainty in snow cover modeling. The areal snow measurements indicate substantial variability, and therefore, formal uncertainty propagation in the simulation of snow depth and water equivalent should be pursued. The propagation of parameter or input variable uncertainty could be handled using a first order approximation of variance for calculated snow water equivalent or temperature, or using Monte Carlo simulation to produce the probability distributions of the simulated snow cover properties (e.g., Garen and Burges 1981). In this case, information about the joint probability distribution (or variance-covariance) of the model parameters and initial values would be useful.

SNTHERM simulated the soil properties and temperatures and could be used to approximate freezing depth during the winter. The model could be run starting in early autumn to simulate ground freezing and soil thermal state. However, the current model does not account for water movement in soil or the effects of solar radiation penetrating into the ground through shallow snow cover, which limit the model's applicability to periods of snow cover.

A second major activity would be a comparison between index-based models or simple energy balance approaches, and SNTHERM. One question is what model complexity is needed to represent point snow and soil processes reasonably well during winter. Of special interest would be simulation of soil surface ice layer formation, which affects substantially the generation of snowmelt runoff. The comparison of energy balance models would, however, require additional measurements of energy fluxes, such as up and downward long-wave radiation. The comparison of models against measured bulk snow temperature or total snow depth and water equivalent does not provide a

reasonable basis to check the validity of the surface energy balance. Net radiation or radiation components would provide the necessary means to check the radiation balance of the surface energy fluxes.

References

Abbott, M. B., Bathurst, J. C., Cunge, P. E., O'Connell P. E. and Rasmussen, J. 1986. An introduction to the European Hydrological System - Système Hydrologique Européen, "SHE", 2: Structure of a physically-based, distributed modelling system, Journal of Hydrology, 87(1/2), 61-77.

Abdulla, F. 1995. Regionalization of a Macroscale Hydrological Model, University of Washington, Department of Civil Engineering, Water Resources Series, Technical Report No. 144, 198 p.

Anderson, E. A. 1976. A Point Energy and Mass Balance Model of a Snow Cover, NOAA Technical Report NWS 19, 150 p.

Anderson, E. A. and Baker, D. B. 1967. Estimating incident terrestrial radiation under all atmospheric conditions, Water Resources Research, 3(4), 975-988.

Arons, E. M. and Colbeck, S. C. 1995. Geometry of heat and mass transfer in dry snow: a review of theory and experiment, Reviews of Geophysics, 33(4), 463-493.

Blöschl, G., Kirnbauer, R. and Gutknecht D. 1991. Distributed snowmelt simulations in an alpine catchment, 1. model evaluation on the basis of snow cover patterns, Water Resources Research, 27(12), 3171-3179.

Bras, R. L. 1990. Hydrology, An Introduction to Hydrologic Science, Addison-Wesley, Reading, Massachusetts, 643 p.

Colbeck, S. C. 1972. A theory of water percolation in snow, Journal of Glaciology, 11(63), 369-385.

Colbeck, S. C. 1974. Water flow through snow overlying an impermeable boundary, Water Resources Research, 10(1), 119-123.

Colbeck, S. C. 1982. An overview of seasonal snow metamorphism, Reviews of Geophysics and Space Physics, 20(1), 45-61.

Colbeck, S. C. 1991. The layered character of snow covers, Reviews of Geophysics, 29(1), 81-96.

Dunne, T., Price, A. G. and Colbeck, S. C. 1976. The generation of runoff from subarctic snowpacks, Water Resources Research, 12(4), 677-685.

Farouki, O. T. 1986. Thermal Properties of Soils, Series on Rock and Soil Mechanics, Trans Tech Publications, Vol. 11, 136 p.

Finnish Meteorological Institute. 1994. Monthly weather reports for January, February, March, and April. (In Finnish: Ilmatieteen Laitos, Kuukausikatsaus Suomen ilmastoon. Tammikuu, Helmikuu, Maaliskuu, ja Huhtikuu, 1994, 88. vuosikerta)

Garen D. C. and Burges, S. J. 1981. Approximate Error Bounds for Simulated Hydrographs, Journal of the Hydraulics Division, ASCE, 7(HY11), 1519-1534.

Gray, D. M. and Prowse, T. D. 1992. Snow and Floating Ice, Ch. 7, In: Maidment, D. R. Handbook of Hydrology, McGraw-Hill Inc., New York, 7.1-7.58.

Jensen, M. E., Burman, R. D. and Allen, R. G. 1990. Evapotranspiration and Irrigation Water Requirements, ASCE Manuals and Reports on Engineering Practice No. 70, 332 p.

Jordan, R. 1991. A One-Dimensional Temperature Model for a Snow Cover, Technical Documentation for SNTHERM.89, U.S. Army Corps of Engineers, CRREL, Special Report 91-16, 49 p.

Kelly, R. J., Morland, L. W. and Morris, E. M. 1986. A three phase mixture model for melting snow, In: Morris, E. M. (Ed.), Modelling Snowmelt-Induced Processes, IAHS Publication No. 155, 17-26.

Kustas, W. P., Rango, A. and Uijlenhoet, R. 1994. A simple energy budget algorithm for the snowmelt runoff model, Water Resources Research, 30(5), 1515-1527.

Langham, E. J. 1981. Physics and Properties of Snowcover, Ch. 7, In: Gray, D. M. and Male, D. H. (Eds.), Handbook of Snow, Principles, Processes, Management and Use, Pergamon Press, Toronto, 275-337.

Lee, R. L. 1978. Forest Microclimatology, Columbia University Press, New York.

Male, D. H. and Gray, D. M. 1981. Snowcover Ablation and Runoff, Ch. 9, In: Gray, D. M. and Male, D. H. (Eds.), Handbook of Snow, Principles, Processes, Management and Use, Pergamon Press, Toronto, 360-436.

Marks, D. 1988. Climate, Energy Exchange, and Snowmelt in Emerald Lake Watershed, Sierra Nevada, University of California, Santa Barbara, 149 p.

McKay, G. A. and Gray, D.M. 1981. The Distribution of Snowcover, Ch. 5, In: Gray, D. M. and Male, D. H. (Eds.), Handbook of Snow, Principles, Processes, Management and Use, Pergamon Press, Toronto, 153-190.

Morland, L. W., Kelly, R. J. and Morris, E. M. 1990. A mixture theory for a phase-changing snowpack, Cold Regions Science and Technology, 17(3), 271-285.

Morris, E. M. 1983. Modelling the flow of mass and energy within a snowpack for hydrological forecasting, Annals of Glaciology, 4, 198-203.

Paasonen-Kivekäs, M. 1994. Distribution of soil nitrogen in an agricultural field, In: Kettunen, J., Granlund, K. Paasonen-Kivekäs, M. and Sirviö, H. (Eds.), Spatial and Temporal Variability and Interdependencies among Hydrological Processes, Proceedings in a Nordic Seminar, Kirkkonummi, Finland, NHP Report No. 36, 142-148.

Price, A. G. and Dunne, T. 1976. Energy balance computations of snowmelt in a subarctic area, Water Resources Research, 12(4), 686-694.

Rango, A. and Martinec, J. 1995. Revisiting the degree-day method for snowmelt computations, Water Resources Bulletin, 31(4), 657-669.

TVA. 1972. Heat and Mass Transfer between a Water Surface and the Atmosphere, Norris, Tennessee, Tennessee Valley Authority, Lab. Report 14, Water Resources Research Report 0-6803.

U.S. Army Corps of Engineers. 1956. Snow Hydrology, Summary Report of the Snow Investigations, North Pacific Division, Portland Oregon, 437 p.

Vehviläinen, B. 1986. Operational spring time forecasting difficulties and improvements, Nordic Hydrology, 17(4/5), 363-370.

Wallace J. M. and Hobbs, P. V. 1977. Atmospheric Science, An Introductory Survey, Academic Press, San Diego, p. 467.

WMO. 1986. Intercomparison of Models of Snowmelt Runoff, World Meteorological Organization, Report No. 23, Geneva, 36 p.

Zuzel, J. F. and Cox, L. M. 1975. Relative importance of meteorological variables in snowmelt, Water Resources Research, 11(1), 174-176.

APPENDIX A Summary of SNTHERM

A summary of the representation of the relevant snow physics in Jordan's (1991) model, SNTHERM, is given here to facilitate the interpretation of its application and testing using the 1994 data set from Sjökulla, Finland.

A.1. Continuity Equations

Jordan (1991) used mixture theory to provide a mathematical description for flow of fluid in a porous material, such as snow or soil. A unit volume of snow is partitioned into a mixture of dry air and water vapor, liquid water, and ice. Similarly, soil is considered as dry solids in addition to water phases and air. The sum of constituent bulk densities defined the total density:

$$\rho_t = \sum_k \theta_k \rho_k = \sum_k \gamma_k \qquad \text{(A.1)}$$

where

ρ_t = density of the total medium [kg m^{-3}]
θ_k = volume fraction of constituent k
ρ_k = density of constituent k [kg m^{-3}]
γ_k = bulk density [kg m^{-3}]
k = constituent index

Porosity for snow and soil were defined as the volumetric fraction of air and liquid in snow, and as the fraction of air, liquid and ice in soil, respectively. Saturation was specified as the fraction of liquid water present in the void volume.

The mixture theory formulation provides the flexibility of using the same set of mass balance equations for a variety of snow and soil materials (Kelly et al. 1986, Jordan 1991). In SNTHERM, snow and soil were divided into horizontal layers which were assumed homogeneous. Therefore, density, porosity, liquid water content, and grain size were assumed constant in an individual layer. The soil layer thickness was fixed, but the snow layer was allowed to compact as snow metamorphosed. Air was assumed to be incompressible, stagnant and at atmospheric pressure, mass changes due to the conduction of dry air were ignored. The continuity equations for the total media and individual mixture components in the interior elements of the snow and soil grids are (Jordan 1991):

$$\frac{\partial}{\partial t}(\rho_t \Delta z) - \overline{\rho_{vk,sat} f_{rh}} \frac{\partial(\theta_v \Delta z)}{\partial t} = -\overline{\left(U_l^{j+1} - U_l^j\right)} - \overline{\left(U_v^{j+\frac{1}{2}} - U_v^{j-\frac{1}{2}}\right)} \qquad \text{(A.2)}$$

for the total media,

$$\frac{\partial}{\partial t}(\gamma_t \Delta z) = -\overline{M_{li} \Delta z} - \overline{M_{vi} \Delta z} \qquad \text{(A.3)}$$

for ice,

$$\frac{\partial}{\partial t}(\gamma_l \Delta z) = -\overline{\left(U_l^{j+1} - U_l^j\right)} + \overline{M_{li} \Delta z} - \overline{M_{vl} \Delta z} \qquad \text{(A.4)}$$

for liquid water, and

$$\overline{(\phi_{sd} - s\phi)\Delta z}\,\overline{f_{rh} C_{kT}} \frac{\partial T}{\partial t} = -\overline{\left(U_v^{j+\frac{1}{2}} - U_v^{j-\frac{1}{2}}\right)} + \overline{M_{vi} \Delta z} + \overline{M_{vl} \Delta z} \qquad \text{(A.5)}$$

for water vapor.

where

$\rho_{vk,sat}$ = Equilibrium vapor density with respect to phase k [kg m^{-3}]

f_{rh} = fractional humidity (=1 for snow)

U_l = mass flux of liquid water [kg m^{-2} s^{-1}]

U_v = mass flux of water vapor [kg m^{-2} s^{-1}]

$M_{k,k'}$ = rate of phase change (M_{li} = melt, M_{vi} = sublimation, M_{vl} = evaporation) [kg m^{-3} s^{-1}]

ϕ_{sd} = solid porosity

s = liquid water saturation

C_{kT} = variation of saturation vapor pressure with temperature relative to phase k [kg m^{-3} °K^{-1}]

T = temperature in a soil or snow layer [°K]

Δz = layer thickness [m]

t = time [s]

j = nodal element index

i = subscript representing ice

l = subscript representing liquid water

v = subscript representing water vapor

The continuity equation for the total media (A.2) states that the changes in material mass and expelled vapor mass equals convection of liquid water and diffusion of water vapor. The convection term is taken as a stepwise approximation of the spatial average $U_l^{j+1} - U_l^j$, and the diffusion term as a piecewise-linear approximation $U_v^{j+1/2} - U_v^{j-1/2}$. The convection of water vapor is ignored, but the expelled vapor from the control volume is taken into account as described in (A.2). The mass flux of liquid water U_l is defined as a gravity flow according to Darcy's law as described later. The saturation

vapor density is related to temperature using an expression for the equilibrium vapor density (Anderson 1976), and the diffusive vapor flux is calculated as:

$$U_v = -D_e f_{rh} C_{kT} \frac{\partial T}{\partial z} \qquad \text{(A.6)}$$

where

D_e = effective diffusion coefficient [$m^2\ s^{-1}$]

The effective diffusion coefficient, D_e, is represented as a function of temperature and air pressure. If the liquid water content in snow exceeds 0.02, the saturated water vapor in the pores is set at the equilibrium vapor pressure over water, otherwise it is set to the corresponding value over ice. The continuity equation for ice (A.3) states that the mass change depends on the mass fluxes of melt and sublimation only. In the case of liquid water, the mass flux due to liquid water movement is added (A.4). Finally, the continuity equation for water vapor (A.5) describes the relation between vapor mass change (a function of temperature) and vapor diffusion, sublimation, and evaporation. The overbar in the equations denotes a temporal average.

A.2. Snow Compaction

A snow compaction term is added to the continuity equation (A.2) to take into account the two snow compaction processes, viz, destructive metamorphism and settling.

$$\overline{CR\rho_s \Delta z} = \overline{\rho_s \Delta z}\left[-\left(\frac{1}{\Delta z}\frac{\partial \Delta z}{\partial t}\right)_{metamorphism} - \left(\frac{1}{\Delta z}\frac{\partial \Delta z}{\partial t}\right)_{overburden} \right] \qquad \text{(A.7)}$$

where

CR = fractional compaction rate of snow cover [s^{-1}]

The metamorphism component in (A.7) increases most during compaction of new snow with low density (<150 kg m^{-3}), and the compaction rate decreases as density increases. Snow settling is due to the weight of snow, and is described as snow load pressure divided by a viscosity coefficient. The equations used for metamorphosis and settling are adopted from Anderson (1976). Grain size changes of snow result from vapor deposition and are described as:

$$\frac{\partial d}{\partial t} = \frac{g_1 |U_v|}{d} \qquad \text{(A.8)}$$

where

d = diameter of snow grain [m]

g_1 = grain growth parameter [m^4 kg^{-1}]

Equation (A.8) describes an inverse relationship between the grain growth rate and size. Vapor flux provides the source for the growth and is assumed to be a purely diffusive process. Grain size change in wet snow is described using a similar equation, where the fraction of liquid water is used instead of vapor mass flux.

A.3. Momentum Equation

The only component of momentum included is for liquid water and is simplified to Darcy's empirical law by assuming that the inertial, convective, and phase change terms are small, and that air is at atmospheric pressure. Furthermore, capillary forces are ignored and the gravity flow of water follows (Colbeck 1972, Jordan 1991):

$$U_l = \rho_l \theta_l v_l = -\frac{K_l}{\mu_l}\rho_l^2 g \qquad \text{(A.9)}$$

where

v_l = seepage velocity [m s^{-1}]

K_l = intrinsic permeability [m^2]

μ_l = dynamic viscosity of water [N s m^{-2}]

g = acceleration due to gravity [m s^{-2}]

The mass change of water is expressed in terms of changes in saturation and porosity; mass change due to sublimation is ignored. Porosity change is described in terms of volumetric changes due to fusion and nodal thickness. The fluid flow equation is:

$$\rho_l(1-s_r)\overline{\phi\Delta z}\frac{\partial s_e}{\partial t} = \frac{\rho_l^2 g}{\mu_l}\left[\overline{\left(K_{max}s_e^3\right)}^{j+1} - \overline{\left(K_{max}s_e^3\right)}^{j}\right] + \overline{M_{li}\Delta z}\left(1-\frac{\rho_l}{\rho_i}\bar{s}\right) - \rho_l \bar{s}\frac{\partial \Delta z}{\partial t} \qquad \text{(A.10)}$$

where

s_r = residual liquid water saturation

s_e = effective liquid water saturation

s = liquid water saturation (= $s_e(1- s_r) + s_r$)

K_{max} = Saturation intrinsic permeability [m^2]

The fluid flow equation states that the water mass change equals the sum of gravitational flux (Darcian flow) and melt flux. Permeability is represented as a function of effective liquid saturation and saturation permeability, which is a function of grain diameter and the bulk density of ice. The residual saturation deficit has to be exceeded before the water front is assumed to move in the snowpack. The fluid flow equation ignores

fingering of flow and ponding of water on the ice layers. Meltwater is artificially drained out of the snowpack at the snow-soil interface.

A.4. Mass Balance Boundary Conditions

The necessary (and sufficient) boundary conditions for the solution of the continuity and fluid flow equations are the mass fluxes across the air-snow interface, which include the mass fluxes of rainfall, snowfall, and turbulent exchange of water vapor. The continuity equations of the snowpack become (Jordan 1991):

$$\frac{\partial}{\partial t}(\rho_i \Delta z) - \overline{\rho_{vk,sat} f_{rh}} \frac{\partial(\theta_v \Delta z)}{\partial t} = -\overline{(U_p - U_l^n)} + \overline{\frac{E_{E0} + E_E w}{L_{vk}}\left(P_{v,air} - f_{rh} P_{vk,sat}^n\right)} + \overline{U_v^{n-\frac{1}{2}}} \quad \text{(A.11)}$$

for the total media,

$$\frac{\partial}{\partial t}(\gamma_i \Delta z) = -\overline{(1 - f_{lp}) U_p} - \overline{M_{li} \Delta z} - \overline{M_{vi} \Delta z} \quad \text{(A.12)}$$

for snowfall,

$$\frac{\partial}{\partial t}(\gamma_l \Delta z) = -\overline{f_{lp} U_p} + \overline{U_l^n} + \overline{M_{li} \Delta z} - \overline{M_{vl} \Delta z} \quad \text{(A.13)}$$

for liquid water, and

$$\overline{(\phi_{sd} - s\phi)\Delta z}\,\overline{f_{rh} C_{kT}} \frac{\partial T}{\partial t} = -\overline{\frac{E_{E0} + E_E w}{L_{vk}}\left(P_{v,air} - f_{rh} P_{vk,sat}^n\right)} + \overline{U_v^{n-\frac{1}{2}}} + \overline{M_{vi} \Delta z} + \overline{M_{vl} \Delta z} \quad \text{(A.14)}$$

for water vapor, respectively, where

E_{E0} = windless exchange coefficient for latent heat [W m^{-2} mb^{-1}]

E_E = exchange coefficient for latent heat [J m^{-3} mb^{-1}]

L_{vk} = Latent heat with respect to phase k [J kg^{-1}]

f_{lp} = fractional mass liquid water content of precipitation

w = wind speed at height z_w [m s^{-1}]

$P_{v,air}$ = water vapor pressure in air at height z_p [mb]

$P_{vk,sat}$ = saturation water vapor pressure with respect to phase k [mb]

U_p = mass precipitation flux [kg m^{-2} s^{-1}]

n = top node index

p = index of precipitation

The right hand side of (A.11) describes the convective mass of precipitation, the turbulent mass exchange due to water vapor phase changes, and the mass of vapor diffusion. Equation (A.12) represents the snowfall mass flux and mass change due to fusion and sublimation on the right, (A.13) the liquid water fluxes, and (A.14) the water vapor exchange, respectively. The fluid flow equation for the top node is:

$$\rho_l(1-s_r)\overline{\phi\Delta z}\frac{\partial s_e}{\partial t} = -\overline{f_{lp}U_p} - \frac{\rho_l^2 g}{\mu_l}\overline{\left(K_{max}s_e^3\right)^n} + \overline{M_{li}\Delta z}\left(1-\frac{\rho_l}{\rho_i}\bar{s}\right) - \rho_l \bar{s}\frac{\partial \Delta z}{\partial t} \qquad \text{(A.15)}$$

To keep the thickness of the top layer suitably small for the assumed physics, the top layer is subdivided into two layers after precipitation events.

A.5. Energy Balance Equations

The energy balance equation sets the rate of change in stored heat equal to the sum of convective heat with water flow, diffusive heat with vapor flux, heat conduction, and net radiative flux. Only short-wave radiation is assumed to penetrate below the top layer. Heat exchange with air masses, except latent heat effects of water vapor, are ignored in

the model. Therefore, diffusive heat with vapor flux is included in the heat conduction term using an effective thermal conductivity, which adds a diffusive term to the thermal conductivity of snow or soil. The thermal conductivity of the snow is represented as a function of air and ice conductivities and the bulk snow density.

The stored heat is partitioned according to the enthalpies of the constituent phases and equals the change in the heat content of the mixture components, and the latent heat of sublimation and fusion. The heat content of the components is calculated separately for the total medium and for the combined ice-water constituent. The latent heat of sublimation is divided into latent heat of expelled water vapor and latent heat of the vapor mass change in a nodal layer.

The latent heat of fusion is derived as follows. The apparent heat capacity method is used to relate the freeze-melt changes to temperature. The fusion phase change is assumed to occur over a small temperature interval resulting in a freezing curve describing the liquid water fraction as a function of temperature. The fraction of liquid water is the sum of capillary and hygroscopic water, both of which depend on the temperature difference from the melting point. The gradient of the freezing curve corresponding to the temperature range determines the water flux resulting from a phase change. Consequently, latent heat of fusion is divided into the heat released from or added to the medium by freeze-thaw, and heat related to the unfrozen net flux of water. The unfrozen net flux of water is combined with the heat content of the ice-water constituent, determined using an enthalpy adjustment factor and the liquid water flux. The enthalpy adjustment factor determines the heat stored per unit ice-water mass and is calculated separately for snow, unfrozen soil, and frozen soil (Jordan 1991). The combined specific heat is calculated as a bulk density weighted average of specific heats of the mixture components. The energy equation for the interior nodes is:

$$\left[\overline{\rho_t c_t \Delta z} + L_{li}\overline{\gamma_w \Delta z F} + L_{vi}\overline{(\phi_{sd} - s\phi)\Delta z f_{rh} C_{kT}}\right]\frac{\partial T}{\partial t} - \overline{\left(U_l^{j+1} - U_l^j\right)}\left[\overline{H} - L_{li}\left(1 - \overline{f_l}\right)\right]$$
$$= -c_l\left[\overline{\left(U_l T_l\right)^{j+1} - \left(U_l T_l\right)^j}\right] + \overline{\left(k_e \frac{\partial T}{\partial z}\right)^{j+\frac{1}{2}}} - \overline{\left(k_e \frac{\partial T}{\partial z}\right)^{j-\frac{1}{2}}} + \overline{\left(I_s^{j+\frac{1}{2}} - I_s^{j-\frac{1}{2}}\right)} \qquad \text{(A.16)}$$

where

c_l = specific heat of water at 0 °C [J kg^{-1} °K^{-1}]

c_t = bulk density weighted specific heat [J kg^{-1} °K^{-1}]

c_w = bulk density weighted specific heat of liquid and ice [J kg^{-1} °K^{-1}]

γ_l = bulk liquid water density [kg m^{-3}]

γ_w = bulk liquid water and ice density [kg m^{-3}]

f_l = mass liquid water fraction ($= \gamma_l/\gamma_w$)

F = slope of the freezing curve ($= \partial f_l / \partial T$) [°K^{-1}]

L_{vi} = latent heat of sublimation [J kg^{-1}]

L_{li} = latent heat of fusion [J kg^{-1}]

H = enthalpy adjustment factor [J kg^{-1}]

k_e = effective thermal conductivity, including effects of vapor diffusion [W °K^{-1} m^{-1}]

I_s = net short-wave radiation flux [W m^{-2}]

The components of the first term in (A.16) determine the change in internal heat content of the total media, energy added or subtracted by latent heat of fusion, and the energy change by the latent heat of sublimation. The second term describes the change in the heat content of the ice-water medium and unfrozen net flux of water. The change in ice-water mass equals the liquid water flux, which is the only mobile fraction in the mixture. The liquid water flux is multiplied by an enthalpy adjustment factor to yield the change in stored heat. The latent heat of fusion accounts for the freezing of infiltrated water. On the right hand side of (A.16), the first term describes the heat convection due to water flow, the second describes the heat conduction and vapor diffusion term, and the last

term determines the net radiative flux. The extinction of solar radiation in the interior nodes decreases exponentially using the extinction coefficient for visible radiation, which is a function of the bulk density of ice-water constituent and snow grain diameter.

A.6. Energy Balance Boundary Conditions

The energy equation uses measured (or estimated) meteorological fluxes as boundary conditions at the snow-air interface, and a constant temperature boundary at the bottom node. The surface energy balance is affected by turbulent fluxes of sensible and latent heat, short and long-wave radiation, and advected heat from precipitation. The short-wave radiation at the surface includes both direct beam and diffuse solar radiation. This radiation is assumed to be diffuse and isotropic. The extinction of short-wave radiation at the top nodal layer is considered separately for the visible and near infrared ranges. Radiation in the infrared range is assumed to be absorbed in the top 2 mm of the snow. The reflected short-wave radiation is estimated using a snow albedo which is calculated as a function of grain size and solar zenith angle (Marks 1988, p. 53). The model allows the use of measured radiation components or estimates of short- and long-wave incident radiation using cloud cover observations.

The latent heat fluxes are estimated using the water vapor pressure difference between the air and top snow node, where the water vapor pressure is assumed to be the saturated value for the snow temperature. The turbulent exchange coefficients are based on bulk transfer coefficients, which depend on the (user specified) aerodynamic roughness length, measurement reference heights, and air stability functions (Anderson 1976). No stability correction is used for stable atmospheric conditions (Jordan 1991, p. 28). The energy equation for the top node is:

$$I_{top} = I_s\downarrow\left(1-\alpha_{top}\right)+\varepsilon I_{ir}\downarrow-\varepsilon\sigma\left(T^n\right)^4+\left(E_{H0}+E_H w\right)\left(T_{air}-T^n\right)$$
$$+\left(E_{E0}+E_E w\right)\left(P_{v,air}-f_{rh}P^n_{vk,sat}\right)-c_p U_p T_p \qquad \text{(A.17)}$$

$$\left[\overline{\rho_t c_t \Delta z}+L_{fi}\overline{\gamma_w \Delta z F}+L_{vi}\overline{(\phi_{sd}-s\phi)\Delta z f_{rh}C_{kT}}\right]\frac{\partial T}{\partial t}$$
$$-\overline{\left(U_p-U_l^n\right)}\overline{H}+L_{fi}\left[\overline{U_p}\left(\overline{f_{lp}}-\overline{f_l}\right)-\overline{U_l^n}\left(1-\overline{f_l}\right)\right] \qquad \text{(A.18)}$$
$$=\overline{I_{top}}-\overline{I_s\downarrow\left(1-\alpha_{top}\right)\left(e^{-\beta_\infty \Delta z}e^{-\beta_{nir}0.002}\right)^n}+c_l\overline{\left(U_l T_l\right)^n}-\overline{\left(k_e\frac{\partial T}{\partial z}\right)^{n-\frac{1}{2}}}$$

where

I_{top} = energy flux across air-snow interface [W m^{-2}]

$I_{ir}\downarrow$ = long-wave radiation influx [W m^{-2}]

β_∞ = bulk or asymptotic extinction coefficient

β_{nir} = extinction coefficient for near-infrared radiation

E_{H0} = windless exchange coefficient for sensible heat [W m^{-2} °K^{-1}]

E_H = exchange coefficient for sensible heat [J m^{-3} °K^{-1}]

c_p = $f_{lp}c_l+\left(1-f_{lp}\right)c_i$

f_{lp} = mass liquid water fraction of precipitation

ε = emissivity of snow surface

σ = Stefan-Boltzmann constant [W m^{-2} °K^{-4}]

A.7. Solution Method

The system of continuity and energy equations for each node at time *t* are solved first for fluid mass, and second, for the energy balance. The quantities changing in time are linearized using an implicit temporal average (Crank-Nicolson scheme):

$$\overline{\chi} = 0.5\left[\chi^{t-\Delta t} + \chi^{t}\right] \tag{A.19}$$

where

χ = any temporal flux or state variable

The system of implicit equations at time t are arranged a with well-conditioned tridiagonal coefficient matrix (A) having row elements:

$$A_3^j \chi^{j+1,t} + A_2^j \chi^{j,t} + A_1^j \chi^{j-1,t} = B^j \tag{A.20}$$

where

A, B = matrix elements

The first and the last rows in the matrix include the top and bottom boundary conditions, respectively, and the number of the rows equals the number of snow and soil layers. The element on the right hand side of (A.20) depend only on the known values at the previous time step t-Δt. Table A.1 presents an abbreviated flow chart of the calculations in SNTHERM (Jordan 1991).

Table A.1. Abbreviated flow chart of SNTHERM.89. Major subroutines are indicated in upper-case italics (Jordan 1991, Figure 6).

1. DECLARE ARRAYS and VARIABLE TYPES. Large common blocks are estimated in *ARRAYS*.
2. OPEN FILES. File names are read from *FILENAME*.
3. READ in general parameters and initial snowpack and soil element values for temperature, thickness, water content and grain size (*GETINPUT*)
4. CALCULATE CONSTANT PARAMETERS for unfrozen water fraction, thermal conductivity, melt zone limits, bulk transfer functions over soil, water content limits, vapor diffusion and others (*CALCONSTANT*)
5. INITIALIZE general liquid water variables (*DENSITY*), combined specific heat and other miscellaneous parameters

BEGIN TIME LOOP

6a. If this is the start of a basic time interval (default 1 hour), then READ in or GENERATE METEOROLOGICAL DATA (*GETMET*) and screen it for out of bound data points. Optionally estimate solar radiation (*INSOL*) or downward long-wave radiation (*SKYRAD*) if measured values are not provided. Adjust measured or estimated radiation for incidence on sloped surface (*SLOPE*).

6b. Automatically SUBDIVIDE basic time interval and INTERPOLATE meteorological data (*SUBTIME*). Size of time step is determined in Section 18.

MASS BALANCE

7. ADD top elements, resulting from SNOWFALL or ponding RAIN (*NEW SNOW*).
8. Determine COMPACTION rate of snow cover as a function of the initial settling rate and overburden (*COMPACT*).
9. Estimate SOLAR HEATING within snow elements as a function of density and grain diameter (*SDSOL*).
10. Estimate TOP BOUNDARY FLUXES, as a function of air temperature, wind speed, relative humidity and radiation (*QTURB*).
11. For RAIN and MELT, compute the mass WATER FLOW exiting each element, using the gravity flow approximation of Colbeck and an upwind discretization scheme (*FILTRATE*).

12a. Estimate mass transfer due to SUBLIMATION and DIFFUSION of WATER VAPOR within snow cover and for top node of bare soil (*DIFFUSION*).

12b. Estimate SNOW GRAIN DIAMETER (*FGRAIN*).

13. Using the snowfall rate and the estimates for water flow, vapor diffusion and compaction rate, UPDATE the SNOW DENSITY, MASS and ELEMENTAL THICKNESS.

THERMAL BALANCE

14. Update THERMAL PARAMETERS, including effective thermal conductivity (*THRK*); combined specific heat, slope of freezing curve, enthalpy adjustment factor and melt zone switches (*THPARAM*).
15. For INITIAL TIME STEP, set PAST fluxes and variables.
16. SET UP and SOLVE linear THERMAL BALANCE equations, using tridiagonal matrix algorithm (*THERMAL, TRIDIAG*). For elements in melt zone, compute temperature change from melt (*FTEMP*). Recompute top fluxes using new temperature. Compute nodal heat fluxes (including solar heating) for use in the next iteration (*FBB*).

FINAL ADJUSTMENTS and PRINTOUT

17. Make final ADJUSTMENTS to LIQUID WATER variables (*DENSITY*), determine melt state (*NMELT*) and make other adjustments.
18. CHECK if CONVERGENCE criteria are met (*CONVERGE*). If not, reduce time step, reset variables and redo iteration. If met, increase time step and continue.
19. Optionally PRINT OUT surface FLUX and METEOROLOGICAL data for this basic time step (*FLUX*).
20. SAVE PAST VALUES for mass, thermal and meteorological parameters (*OLD*).
21. Divide or combine thick or thin snow elements (*SUBDIVIDE, COMBINENODES* and *COMBO*).
22. PRINT OUT information for this basic time step (*WRITE*). If measured temperatures are provided, compute RMS error.

END MAIN TIME LOOP

23. CLOSURE